nagra.

Arbeitsbericht NAB 19-18

Benchmark study of undrained triaxial testing of Opalinus Clay - analysis and comparative evaluation

October 2019

National Cooperative
for the Disposal of
Radioactive Waste

Hardstrasse 73
P.O. Box 280
5430 Wettingen
Switzerland
Tel. +41 56 437 11 11

www.nagra.ch

nagra.

Arbeitsbericht NAB 19-18

Benchmark study of undrained triaxial testing of Opalinus Clay - analysis and comparative evaluation

October 2019

A.Minardi, A. Ferrari & L. Laloui

Laboratory for Soil Mechanics – LMS
Swiss Federal Institute of Technology – EPFL

KEYWORDS
Opalinus Clay, undrained triaxial test, benchmark

National Cooperative
for the Disposal of
Radioactive Waste

Hardstrasse 73
P.O. Box 280
5430 Wettingen
Switzerland
Tel. +41 56 437 11 11

www.nagra.ch

Nagra Arbeitsberichte ("Working Reports") present the results of work in progress that have not necessarily been subject to a comprehensive review. They are intended to provide rapid dissemination of current information.
This report was prepared on behalf of Nagra. The viewpoints presented and conclusions reached are those of the author(s) and do not necessarily represent those of Nagra.

Executive summary

Five different laboratories were selected by Nagra to perform a benchmark study of undrained triaxial testing of Opalinus Clay (OPA). Core material was taken from the Mont Terri Underground Research Laboratory (URL), both from the "shaly" and the "sandy" facies. A total of thirty tests were carried out. The aim of the study was to demonstrate that very similar quantitative results can be achieved by different laboratories testing "identical core material" if strict sample handling and testing procedures were adopted.

In addition, the robustness of testing results was also to be demonstrated by using two fundamentally different procedures to carry out the saturation of the specimens before the shearing phase of the tests.

This report presents a detailed diagnostic analysis of all the experimental stages ("phases") of the performed tests. A comparison of the testing results obtained by the different laboratories is presented, with the aim of assessing and validating the testing procedures for the planning and performance of future testing campaigns.

Good to very good reproducibility was achieved in tests carried out with Opalinus Clay from the shaly facies ("shaly OPA"), in which samples are homogeneous in terms of macroscopic structure and mineralogical composition. The reproducibility of the testing results was demonstrated not just using the same testing procedure by two different laboratories, but also by using the two different procedures to saturate the samples prior to the shear phase.

In contrast to the shaly facies, comparison of test results with core material from the sandy facies ("sandy OPA") is more challenging due to the inherent heterogeneity of the material. Compared to the shaly facies, index properties and the bulk mineralogical composition of tested samples from the sandy facies was much more heterogeneous.

The study demonstrates that robust testing of Opalinus Clay is possible when rigorous testing procedures are adopted and respected. Robust testing also yields greater confidence in the evaluation of the hydro-mechanical response of the material.

Table of Contents

The electronic data files (test raw data) can be made available by Nagra on request.

List of Tables

List of Figures

1 Introduction

The report summarizes the analysis of a benchmarking study on undrained triaxial testing of Opalinus Clay. The aim of this experimental study was the definition of rigorous and consistent testing procedures to perform undrained triaxial tests on the Opalinus Clay (OPA).

Seven different contractors were invited and five met the requirements to participate in the benchmark study. The participating laboratories and the respective contacts were:

- Erich Pimentel, ETH Zurich/Institute of Geotechnics, Switzerland
- Carlo Dietl & Eberhard Jahns, Gesteinslabor Dr. Eberhard Jahns, Heiligenstadt, Germany
- Jørn Stenebråten, Sintef Industry, Trondheim, Norway
- Bahman Bohloli & Magnus Soldal, Norwegian Geotechnical Institute, Oslo, Norway
- Rudy Stankovic, Rock Soil Testing and Development Company, Park City/Utah, USA

The main goal of the diagnostic analysis presented in this document is to i) examine each individual test, from the specimens' preparation to the shearing phase, in order to evaluate its quality, and ii) to conduct a comparative analysis of the tests of the different laboratories to discuss the robustness of the adopted testing procedures.

The report is organized as follows:

- Chapter 2 provides a general description of the testing programme along with the testing procedures adopted by the contractors.
- Chapter 3 summarizes the basic properties of the tested specimens, focusing in particular on the assessment of the water content.
- The mineralogical composition of the tested materials is presented in Chapter 4; the analyses were performed by the University of Bern (UniBE).
- Chapter 5 is dedicated to the initial phases of the tests, where the specimens were re-saturated and consolidated to the desired confining stress; particular attention is given to the measurement of the swelling pressure, and the assessment of the saturation with the evaluation of the Skempton's B coefficient.
- A diagnostic analysis of the shearing phase of the tests is presented in Chapter 6.
- Chapter 7 focuses on the assessment of the elastic response, with special attention on the behaviour exhibited during the unloading/reloading cycles.
- A comparison of the deformation behaviour during the shearing phase of the tests is presented in Chapter 8. The stress paths, the stress-strain relationships, and the evolution of the pore fluid pressure during shearing are carefully analysed.
- Chapter 9 provides a final discussion and a summary of the performed analysis.

2 Testing programme

Core samples from the shaly and the sandy facies in Mont Terri URL were tested. The specimens from the shaly facies were tested considering three bedding orientations with respect to the applied axial load: perpendicular to bedding (hereafter referred to as S-tests), parallel to bedding (P-tests), and oblique to bedding (Z-tests). Three different initial consolidation stresses (p'_{in}) were selected to carry out the shearing of the specimens: 4 MPa, 10 MPa, and 16 MPa. Tab. 1 summarizes the performed tests by each contractor with the principal testing information. The test number (#) refers to Nagra's programme; this number is used to indicate a series of tests performed by the contractors with the same testing conditions in terms of facies, bedding orientation, and initial consolidation stress. On the other hand, the test ID is given by the contractors and it identifies a single test in the programme. The adopted stress path for most of the performed tests was Conventional Triaxial Compression (CTC) where the cell confining pressure is kept constant while the axial stress is increased. Stress paths different from CTC were also considered in a few tests. Fig. 1 provides a summary of the possible stress paths in the plane mean total stress (p) versus deviatoric stress (q) that can be considered to carry out triaxial test; the deviatoric stress is here defined as axial stress minus radial stress. The upper part of the plane (compression part) summarizes the stress paths that induce axial compression of the tested specimen. The axial compression can be induced by either increasing the axial stress σ_a (CTC path), reducing the radial stress σ_r (RTC path), or increasing σ_a and reducing σ_r at the same time (TC path). The lower part of the plane contains the stress paths that induce axial extension of the specimen. The axial extension can be induced by either decreasing the axial stress (RTE path), increasing the radial stress (CTE), or decreasing σ_a and increasing σ_r at the same time (TE path). Therefore, when the term reduce is used to define the stress path, it means that one of the two stresses is decreased while the other is kept constant. On the other hand, when the term conventional is used to define the stress path, it means the one of the two stresses is increased and the other is kept constant. In the paths TC and TE both stresses are changed at the same time to keep the mean total stress constant. Among all these stress paths, those that were considered for the testing programme in addition to CTC were: Reduced Triaxial Extension (RTE), Conventional Triaxial Extension (CTE), and Triaxial Compression (TC). In all the three cases, the specimens were prepared with bedding orientation perpendicular to the cylindrical axis (S-tests).

For some of the tests, two specimens were tested; this was the case of the Test 2 for Lab A (T2289 and T2332) and Lab C (BGC2-1-2 and BGC2-1-4), Test 8 for Lab D (BGC2-17-4 and BGC2-17-1). Lab E was the only contractor that performed a multistage triaxial test (BGC2-16-3), with effective confining stress of 4, 10, and 16 MPa.

Tab. 2 summarizes the cores used by each contractor to prepare the specimens for triaxial testing. Indications on the specimens' size and lateral drainage configuration (presence of side drains) are also provided in the table. To properly evaluate the strain rate, each contractor performed a consolidation test to determine the consolidation coefficient (c_v); the methodologies presented in Renner et al. (2000) and Head et al. (2011) were used to evaluate the strain rates.

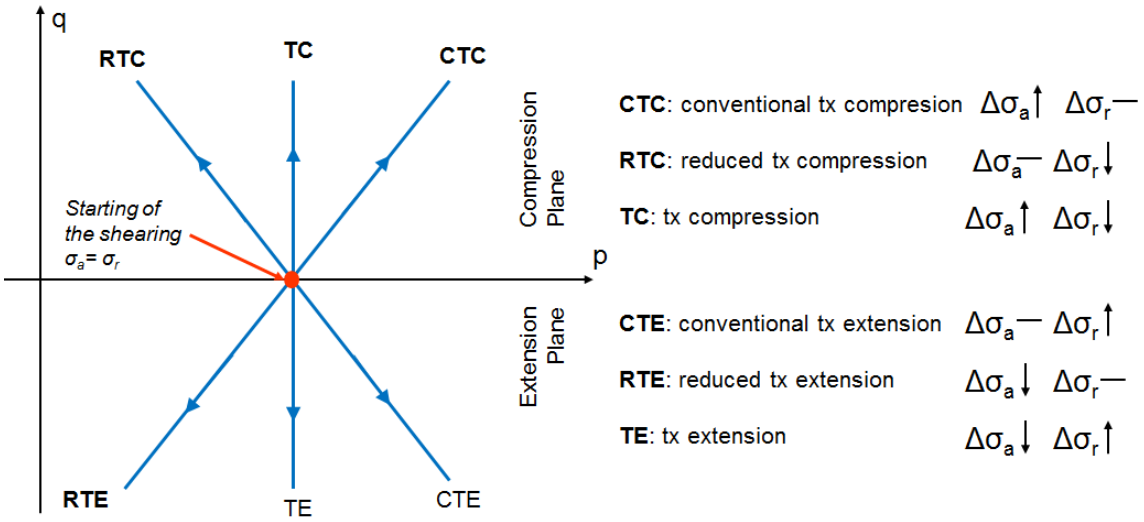

Fig. 1: Summary of possible stress paths that can be adopted to perform triaxial tests

On the right side it is indicated which of the two stresses (axial σ_a and radial σ_r) is increased or decreased.

Tab. 1: Summary of the tests performed by each contractor

Lab	Test ID	Test #	Facies	Bedding	Stress path	p'_{in} [MPa]	Strain rate [s^{-1}]
Lab A	T2303	1	Shaly	S	CTC	4	4.8×10^{-8}
Lab A	T2289	2	Shaly	S	CTC	10	4.8×10^{-8}
Lab A	T2332	2	Shaly	S	CTC	10	9.7×10^{-8}
Lab A	T2280	3	Shaly	S	CTC	16	4.8×10^{-8}
Lab A	T2304	4	Shaly	P	CTC	10	4.8×10^{-8}
Lab A	T2300	5	Shaly	S	CTE	10	4.8×10^{-8}
Lab A	T2310	6	Sandy	S	CTC	10	4.8×10^{-8}
Lab A	T2311	7	Sandy	S	CTC	16	4.8×10^{-8}
Lab B	CIU432_2_0	1	Shaly	S	CTC	4	2×10^{-7}
Lab B	CIU432_2_1	2	Shaly	S	CTC	10	2×10^{-7}
Lab B	CIU432_2_3	3	Shaly	S	CTC	16	3×10^{-7}
Lab B	CIU432_2_4	4	Shaly	P	CTC	10	1×10^{-7}
Lab B	CIU432_2_5	5	Shaly	S	RTE	7.2	1×10^{-7}
Lab B	CIU432_2_6	6	Sandy	S	CTC	10	3×10^{-7}
Lab B	CIU432_2_7	7	Sandy	S	CTC	16	3×10^{-7}
Lab C	BGC2-1-2	2	Shaly	S	CTC	7.5	2×10^{-7}
Lab C	BGC2-1-4	2	Shaly	S	CTC	7.5	2×10^{-6}
Lab C	BGC2-1-1	3	Shaly	S	CTC	16.8	1×10^{-7}
Lab C	BGC2-1-11	4	Shaly	P	CTC	9	2×10^{-7}
Lab C	BGC2-1-13	4	Shaly	P	CTC	16.5	2×10^{-7}
Lab C	BGC2-1-3	5	Shaly	S	TC	20	2×10^{-7}
Lab C	BGC2-1-22	10	Shaly	Z	CTC	4	2×10^{-7}
Lab C	BGC2-1-23	11	Shaly	Z	CTC	11	2×10^{-7}
Lab C	BGC2-1-24	12	Shaly	Z	CTC	16.4	2×10^{-7}
Lab D	BGC2-17_A3	6	Sandy	S	CTC	10	3×10^{-8}
Lab D	BGC2-17_4	8	Sandy	S	CTC	3.5	3×10^{-8}
Lab D	BGC2-17_1	8	Sandy	S	CTC	3.6	3×10^{-8}
Lab E	BGC2-15-1	6	Sandy	S	CTC	10	4.3×10^{-8}
Lab E	BGC2-16-3	7	Sandy	S	CTC	4, 10, 16	4.3×10^{-8}
Lab E	BGC2-15-2	8	Sandy	S	CTC	10	4.3×10^{-8}

Tab. 2: Summary of the cores used by contractors and testing configuration (specimen's size, use of side drains)

Contractors	**Core #, facies, test #**	**Specimen size** [mm]	**Side drains #**
Lab A	BGC2_31, shaly, 1-2-3-4-5 BGC2_18, sandy, 6-7	25 × 50 mm	4 plastic (vyon) filters
Lab B	BGC2_34, shaly, 1-2-3-4-5 BGC2_19, sandy, 6-7	25 × 50 mm	4 metal strips
Lab C	BGC2_29, shaly, 2-3-4-5-10-11-12	19 × 38 mm	2 to 4 metal strips
Lab D	BGC2_17, sandy, 6-8	25 × 50 mm	Not used
Lab E	BGC2_15, sandy, 6-8 BGC2_16, sandy, 7 (multistage)	50 × 100 mm	8 filter papers

Specimen preparation and testing procedures

The extraction of the specimens from the cores was performed by all the labs using a drilling machine. Lab B used a special core barrel configuration where an internal piston was used to stabilize the specimen during drilling by the application of a small axial force. Different types of hydrocarbons (non-polar and non-wetting) were used as cooling fluids by the different labs. Lab E used air-flushing during drilling to avoid direct contact of the specimens with fluid. Lab A used dry drilling for the Test 2 (T2280).

In order to have homogenous and intact specimens from the cores, CT-scans were used to identify the most suitable sections in the cores for drilling. The target zones were selected upon Nagra's guidance. An example of CT-scans is presented in Fig. 2 for the cores BGC2_34 (shaly OPA) and BGC2_19 (sandy OPA) used by Lab B for the preparation of the specimens. These figures highlight the less homogeneous composition of the sandy OPA. The curves at the right side of the cores show the CT-number, which give an indication of the material's density. Further scans can be found in the reports provided by the contractors.

The testing procedure requested by Nagra foresaw the following steps to carry out undrained triaxial tests:

1. An initial isotropic total stress (0.5 – 1 MPa) is applied to the specimen to ensure the contact with the axial piston. The saturation of the specimen is then performed at **constant volume**; axial and radial stresses are progressively increased to keep the specimen's volume constant while it is put in contact with fluid at low back pressure (lower than 100 kPa). This procedure allows the determination of the axial and radial swelling pressures. Next, the confining is set equal to the axial stress and the back pressure is increased to 2 MPa (the total stresses are also increased to keep the effective stress constant).

2. The assessment of the specimens' saturation is carried out by measuring the Skempton's B coefficient (B-check test). At least three isotropic undrained loading steps are performed. More steps are applied when unsatisfactory values (not in interval 0.4 to 1.0) are obtained. At the end of the last measurement, the pore fluid pressure should be approximately 5 MPa.

3. Drained consolidation of the specimen to the target consolidation stress is performed; three values of consolidation stresses are defined: 4 MPa, 10 MPa, and 16 MPa. The pore fluid pressure is kept constant to 5 MPa during consolidation.

4. The final stage is the shearing of the specimens at constant axial strain rate until specimen's failure and achievement of the ultimate condition (post-peak).

This testing procedure can be considered as the "conventional procedure", and it was adopted by Lab A, Lab B, Lab D. Other examples of this procedure can be found in Favero et al. (2018).

A different procedure was used by Lab C, and it can be referred to as "alternative procedure". This alternative procedure foresaw the equalization of the specimen to different relative humidity values (between 92 % and 98 %) in desiccators before testing in order to achieve different saturation conditions. During this equalization phase, the specimens were put in a cage in order to prevent swelling and cracking of the material due to the possible wetting process. After, the specimens were mounted in the rig and an initial undrained loading was carried out until an increase of the back (fluid) pressure was detected. At this stage, the specimen was assumed to have achieved the fully saturated condition; B-check test was then performed in three steps. A pressure transducer was placed inside the vessel very close to the specimen to monitor the evolution of the pore fluid pressure during the application of the external mechanical stress. When this testing procedure is adopted, the pore fluid pressure cannot be controlled actively unless opening the valve of the drainage line, in which case an external pore fluid is also required. Further details on the testing configuration can be found in Giger et al. (2018).

A "hybrid" procedure was used by Lab E, as the specimens were also exposed to a controlled relative humidity (94 – 96 %, see below) in desiccators after dry drilling. However, the rest of the adopted testing procedure was essentially conventional and included a consolidation phase.

In both testing procedures, the adopted fluid was an artificial water prepared according to a recipe provided by Nagra. The artificial water was composed of demineralised water and 6.7356 g/l NaCl, 0.0456 g/l $NaHCO_3$, 1.7510 g/l $CaCl_2$ $2H_2O$, 0.1902 g/l KCl, 1.8635 g/l $MgCl_2$ $6H_2O$ and 3.4089 g/l Na_2SO_4.

The specifications of the sensors used by the different contractors to measure the axial force, and specimens' deformations (displacements) are summarized in the Tab. 3. The specification of the pumps used to control the confining and fluid pressures are not reported as, in all the cases, the range and resolution were appropriate for the testing purposes. It has to be noted that the system used by Lab E (* in the Tab. 3) to measure the radial deformations was not working properly during the tests.

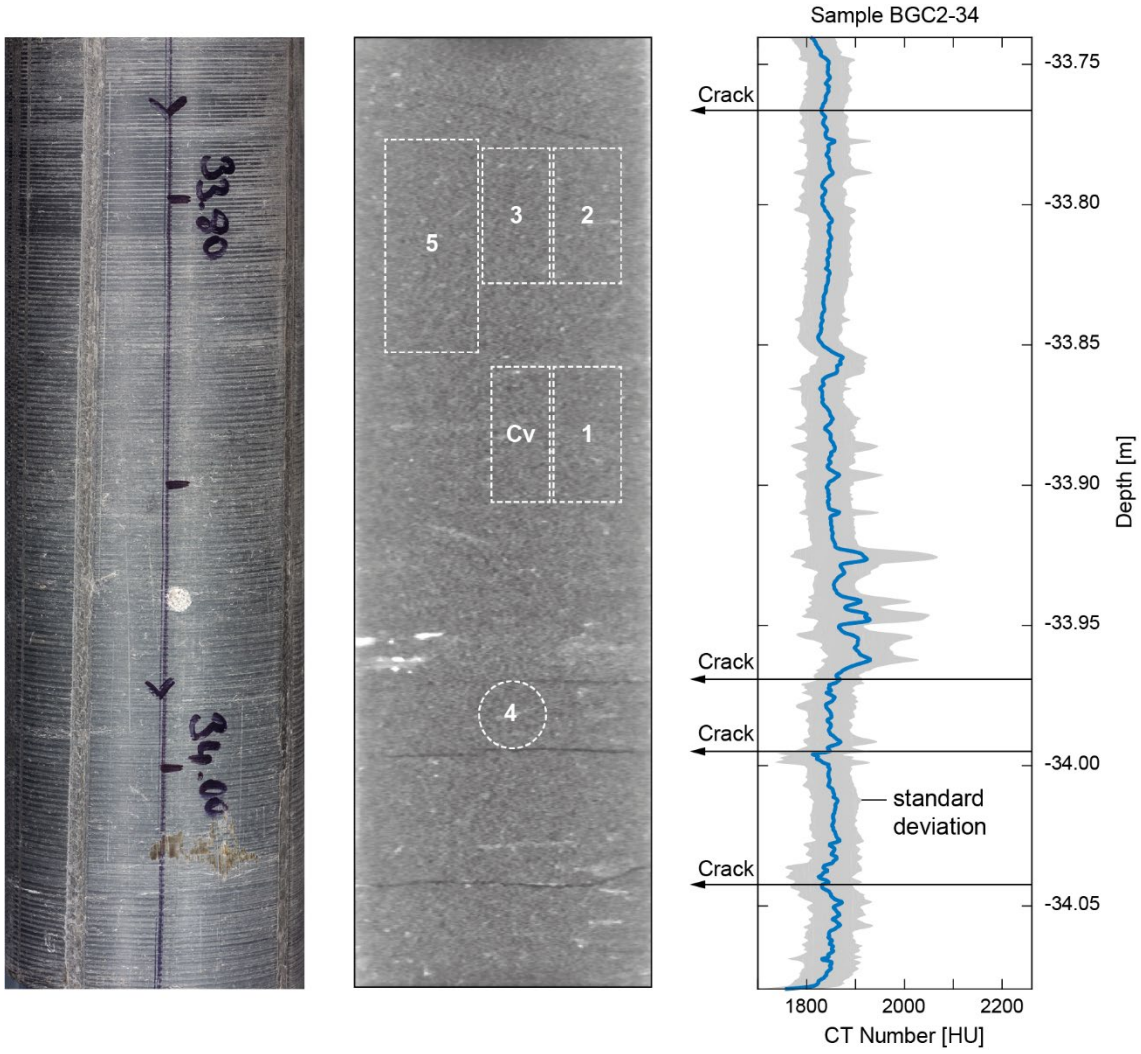

Fig. 2a: Virtual section of stacked XCT-scans of cores BGC2_34 used by Lab B.

Location of specimen plugs are indicated in dashed white lines with numbers denoting test IDs (cf. Tab. 1).

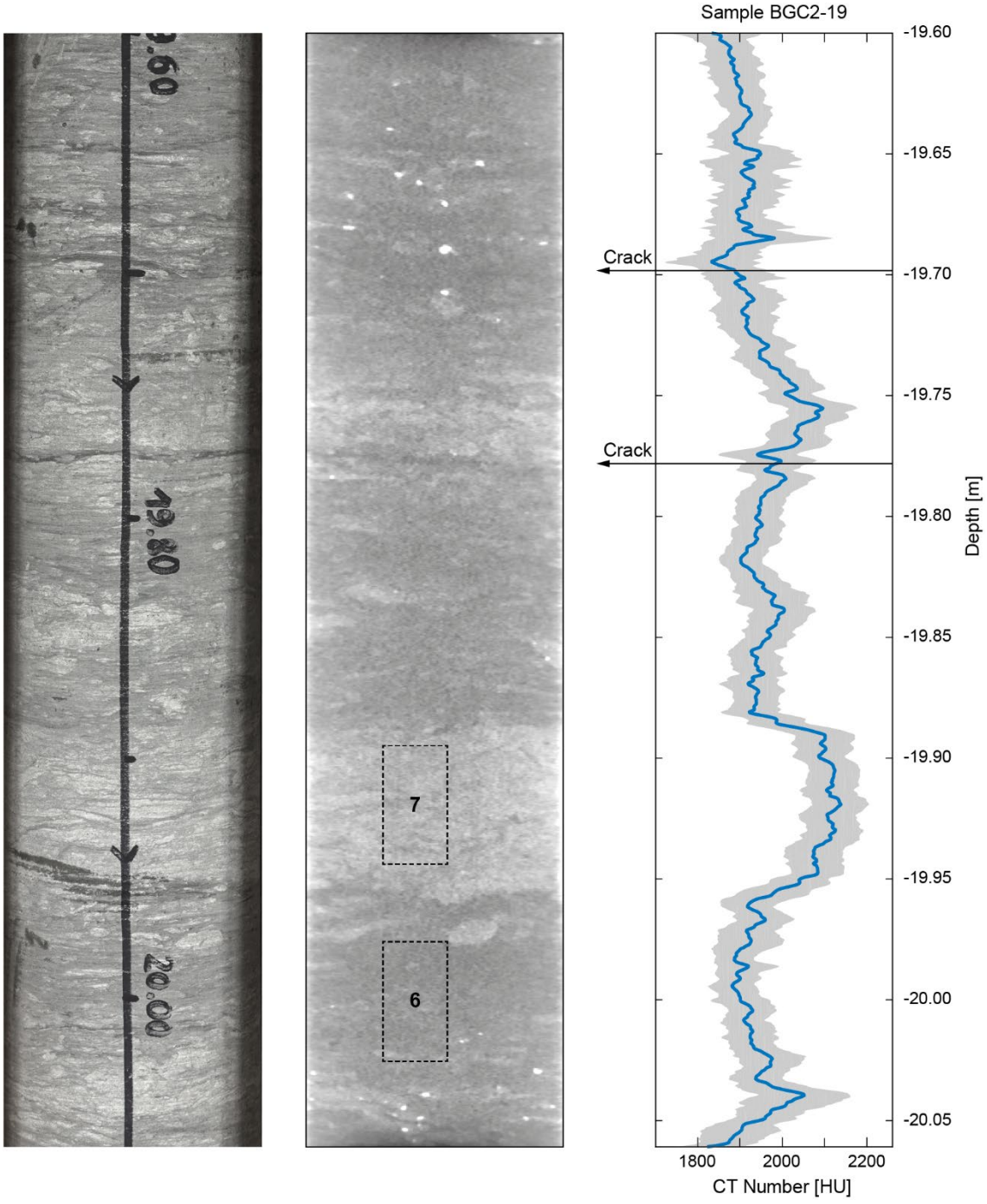

Fig. 2b: Virtual section of stacked XCT-scans of BGC2_19 used by Lab B

Location of specimen plugs are indicated in black lines with numbers denoting test IDs (cf. Tab. 1).

Tab. 3: Specifications of the sensors and transducers adopted in the testing set-ups of the contractors

Contractors	**Load Cell**	**Axial response**	**Radial response**
Lab A	Internal – Range: 44.5 kN External – Range: 250 kN	LVDTs Range: 2.54 mm	LVDTs Range: 2.54 mm
Lab B	Internal Range: 250 kN	LVDTs Range: 6 mm	Strain gauge cantilever Range: 4 mm
Lab C	Internal	Strain gauge cantilever	Strain gauge cantilever
Lab D	Internal Range: 600 kN and 50 kN	LVDTs Range:+/- 5mm	Strain gauge
Lab E	External Range: 600 kN	Magnetic sensor	Magnetic sensor on chain*

3 Basic properties of the specimens

This section presents the initial conditions of the tested specimens in terms of water content, grain density, porosity, and degree of saturation.

Lab A computed the water contents before and after testing (Fig. 3) directly on the specimens by measuring their weights before testing, after testing, and after oven-drying at 110 °C. However, as stated by the contractor in the report, the main disadvantage of this procedure is related to the difficulty in completely removing the specimens from the rig after testing; this aspect might lead to a slightly overestimation of the water content before testing. The initial bulk density of the specimens was obtained from calliper measurements (volume).

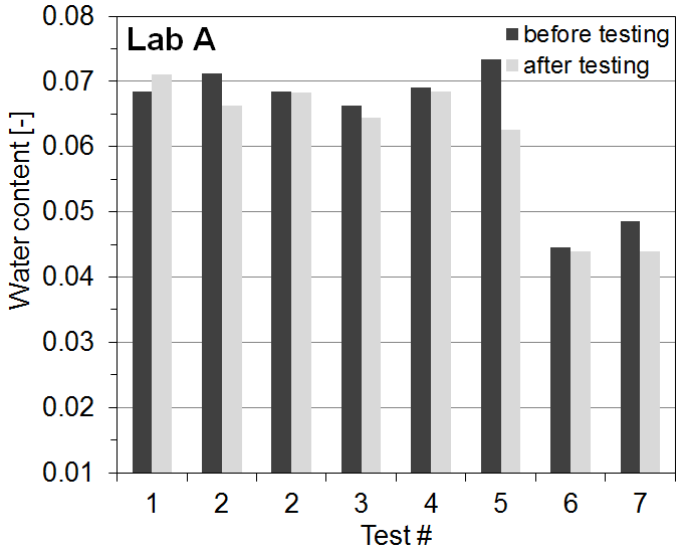

Fig. 3: Water content of the specimens tested by Lab A

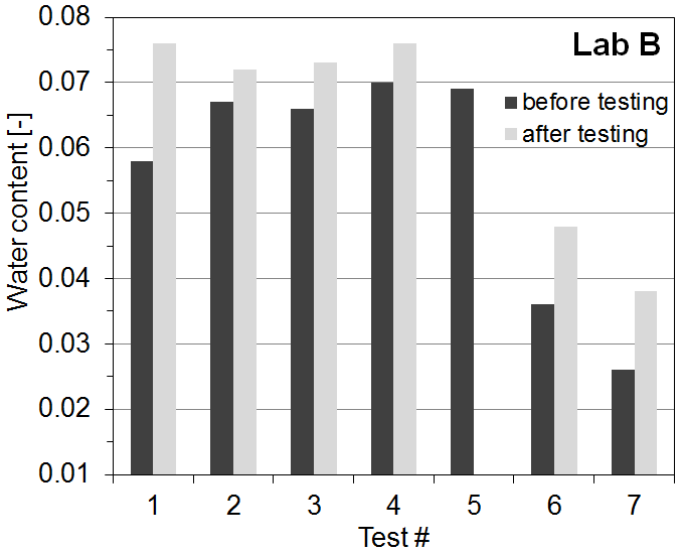

Fig. 4: Water content of the specimens tested by Lab B

Lab B adopted an accurate procedure to evaluate the water content and bulk density of the specimens prior testing by using a trimming piece of material obtained by a spare part of the specimen (see the Lab B report for more details). In particular the initial bulk density was computed both on the specimens with calliper measurements and on the trimming with Archimedes method. The Archimedes method can be considered more accurate; these values were used to compute the initial void ratio and initial water saturation. The end-trimmings were also used to obtain the water content before testing, while after testing the water content was obtained directly from the oven-drying of the specimens. Fig. 4 shows the difference in water content before (initial) and after (final) testing.

Lab C used an initial equalization of the specimens in desiccator under vacuum at high relative humidity (RH = 96 – 98 %) before testing. This procedure was used to facilitate the saturation phase of the tests. Fig. 5 shows the water content of the specimens tested by Lab C after preparation, at the end of the equalization in the desiccator, before testing, and after testing. These values were back-calculated from the dry weight of the specimens measured after testing. The graph clearly indicates that the equalization process (that lasted between one and two months) induced an increase in the specimens' water content. After the equalization the specimens were transferred to the laboratory for testing; the water content at that time was always lower than the water content at the end of the equalization, meaning that tiny water loss occurred during shipping. Finally, the water contents after testing are equal or slightly lower than before testing.

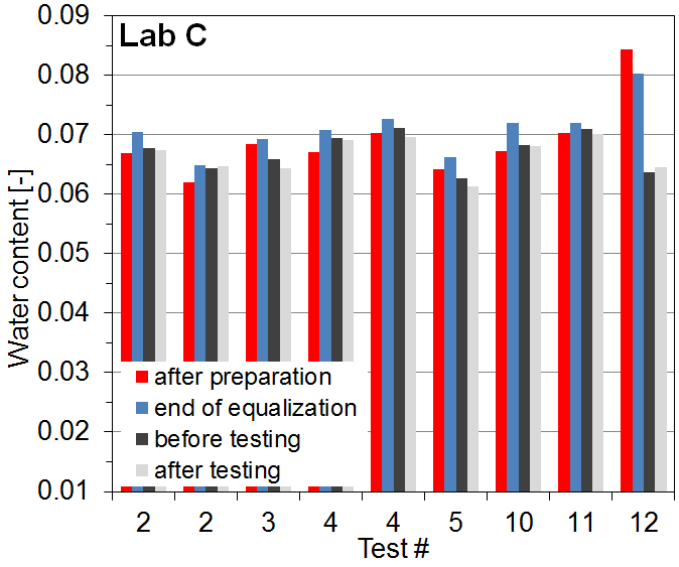

Fig. 5: Water content of the specimens tested by Lab C

The specimens tested by Lab E were equalized in a controlled relative humidity desiccator with a K_2SO_4 saturated solution (RH between 94 % and 96 %) for a period of one month; all the specimens gained water during the equalization. Remaining pieces of cores were also equalized in the desiccator; total suction was measured to check the equalization. Values between 3.7 MPa and 5 MPa were obtained; this result however does not confirm the full equalization of the tested specimens as the size of the remaining pieces of the cores is not specified. Moreover, in some cases the specimens exhibited horizontal cracks during the equalization in the desiccator. This aspect would indicate that the imposed relative humidity was too high compared to the state of the specimen after preparation. These specimens were not used for triaxial testing. The bulk density was measured before testing, but not the water content. After testing the specimens were broken in two parts. One piece was used for direct measurement for the water content, while the second one was covered with paraffin to measure its volume with Archimedes' method; the paraffin was then removed, and the water content was obtained also from the second piece. For the Test 6 (BGC2-15-1) the final water contents were 0.063 and 0.041, while for the Test 8 (BGC2-15-2) the values were 0.062 and 0.058. The higher difference in the Test 6 might be related to the heterogeneity of the specimen that can be observed from the CT scan (see the report of the contractor). For the Test 7 (BGC2-16-3), only one measurement of water content was performed after testing (0.073).

Lab D measured water content at both 70 °C and 105 °C. An increase of the absolute water content of about 0.1 – 0.3 % was found when the material is dried at higher temperature. The water contents reported in the Fig. 6 were measured at 105 °C, except for the specimen used for Test 8 (BGC2-17_4, middle columns in Fig. 6) which was dried at only 70 °C.

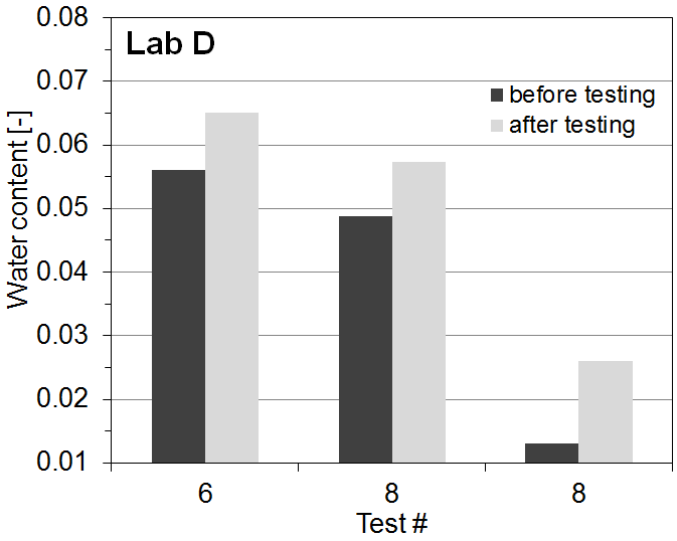

Fig. 6: Water content of the specimens tested by Lab D

Fig. 7 provides a summary of the values of water content (w), grain density (ρ_s), porosity (n), and degree of saturation (S_r) of the specimens before testing. The values of the grain density were obtained from helium pycnometer tests carried out at the University of Bern by the research group of Professor Martin Mazurek. In the case of Lab C, only one measurement of grain density was performed, and it was assumed valid for all the specimens due to the homogeneity of the core sample. The values of porosity and degree of saturation were computed according to the following equations, where e is the void ratio, ρ_b is the bulk density, and ρ_w is the water density.

$$e = \frac{\rho_s\,(1+w)}{\rho_b}$$

$$n = \frac{e}{1+e}$$

$$S_r = \frac{\rho_s\,w}{p_w e}$$

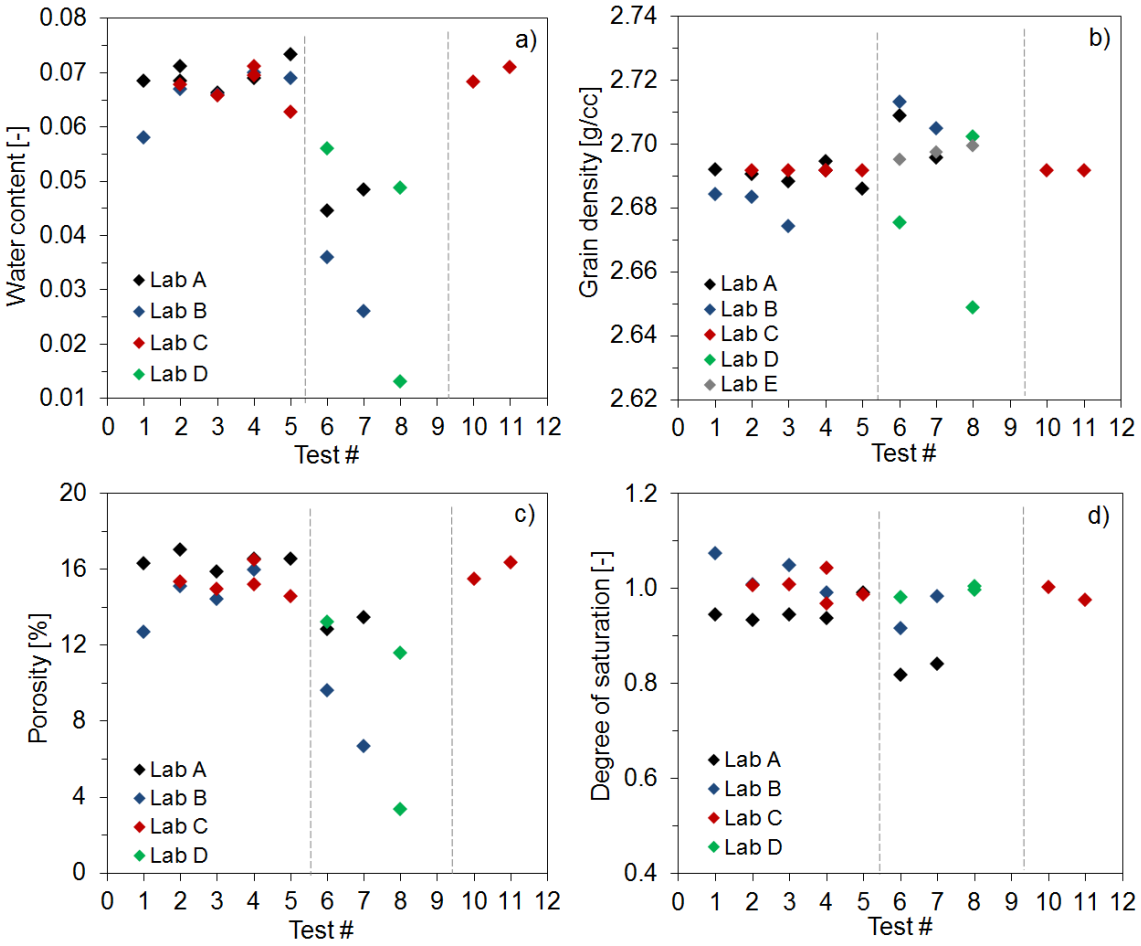

Fig. 7: Summary of the values of the a) water content, b) grain density, c) porosity, d) degree of saturation for the tested specimens

4 Mineralogy

Mineralogical analyses of the tested specimens after testing were performed at the University of Bern (UniBE) by the research group of Professor Martin Mazurek. Tab. 4 summarizes the results for tested specimens (shaly OPA highlighted in blue, and sandy OPA in red); the Sample-ID are in accordance with Tab. 1. While for Lab A and Lab B almost all the tested specimens were used for the mineralogical analysis, in the case of Lab C only on measurement was performed and it was assumed to be valid for all the tested specimens due to the homogeneity of the core (BGC2-29). The analysis on the specimen BGC2-16-3 (Lab E) was performed on the negative of the core from which the specimen was prepared for triaxial testing. The specimen of the Lab D Test 6 (BGC2-A3) was not used for the mineralogical analysis.

Tab. 4: Mineralogical composition of the tested specimen (analyses performed at UniBE)

Nagra core-ID	Contractor	Sample-ID	Depth interval [cm]		Calcite [wt.%]	Dolomite / Ankerite [wt.%]	Siderite [wt.%]	Quartz [wt.%]	Albite [wt.%]	K-feldspar [wt.%]	Pyrite [wt.%]	C(org) [wt.%]	Total clay minerals [wt.%]
BGC2-34	Lab B	CIU432_2_0	12.00	18.00	8	1.4	0.8	18	2.1	2.2	0.9	0.9	65
BGC2-34	Lab B	CIU432_2_1	4.00	11.50	7	1.4	0.7	19	2.0	1.5	0.7	1.0	67
BGC2-34	Lab B	CIU432_2_3	4.00	11.50	6	2.1	0.7	20	3.2	1.9	0.9	1.1	64
BGC2-34	Lab B	CIU432_2_4	26.00	29.00	9	1.0	1.0	13	1.9	1.4	0.9	1.0	71
BGC2-19	Lab B	CIU432_1_6	38.00	43.50	12	7.6	1.7	50	4.2	3.5	0.2	0.6	20
BGC2-19	Lab B	CIU432_1_7	29.00	36.00	47	0.2	2.7	31	3.1	1.6	0.05	0.3	14
BGC2-31	Lab A	T2303	21.50	27.00	13	0.5	0.6	19	3.3	3.7	1.1	0.9	58
BGC2-31	Lab A	T2289			6	0.2	0.9	18	3	5	1.0	1.3	64
BGC2-31	Lab A	T2280			9	0.5	1.6	17	3	6	1.0	1.0	60
BGC2-31	Lab A	T2304	18.85	24.55	10	0.7	0.9	18	3.2	2.6	1.1	0.8	62
BGC2-31	Lab A	T2300	21.50	27.00	10	0.8	0.8	17	2.8	2.3	1.1	1.0	64
BGC2-18	Lab A	T2310	15.00	20.50	20	2.8	1.7	45	3.5	3.5	0.3	0.6	22
BGC2-18	Lab A	T2311	22.00	27.60	14	1.7	1.6	46	3.4	3.7	0.5	0.7	28
BGC2-29	Lab C				7	0.1	1.8	17	3	6	1.3	1.1	62
BGC2-17	Lab D	BGC2_17_04	23.50	28.50	10	0.9	1.4	47	5.4	4.8	0.6	0.6	30
BGC2-17	Lab D	BGC2_17_01	1750	1755	44	0.7	1.9	34	2.0	2.6	0.1	1.5	13
BGC2-15	Lab E	BGC2-15-1-up	1569	1574	7	1.0	2.6	43	3.6	3.2	0.4	0.6	38
BGC2-15	Lab E	BGC2-15-1-down	1574	1579	26	1.0	3.4	43	3.2	3.5	0.2	0.4	20
BGC2-15	Lab E	BGC2-15-2-up	1581	1587	7	1.3	2.4	42	3.1	3.5	0.5	0.7	39
BGC2-15	Lab E	BGC2-15-2-down	1587	1591	14	3.1	5.2	39	2.8	3.5	0.4	0.5	31
BGC2-16	Lab E	BGC2-16-3 (negative)	1648	1658	13	0.8	2.9	42	2.9	3.2	0.3	0.6	34

A summary of the mineralogical composition of the cores is presented in Fig. 8. The values of calcite, quartz, clay, and other minerals are obtained as average from the measurements of the specimens obtained from the same core. The graphs clearly highlight the dominant clay and quartz content in the shaly and sandy OPA, respectively. Moreover, the sandy OPA exhibited much greater heterogeneity where variations greater than 20 – 30 % are observed in clay and calcite contents. The heterogeneity is also important on individual cores. Looking at the values in the Tab. 4, the specimens prepared from the core BGC2-19 (Lab B) and BGC2-17 (Lab D) show significant variations of calcite and clay contents; in the case of Lab B, this aspect can be also observed from the CT scan illustrated in the Fig. 2. As presented later in the section, this aspect has significant influence on the mechanical response of the material.

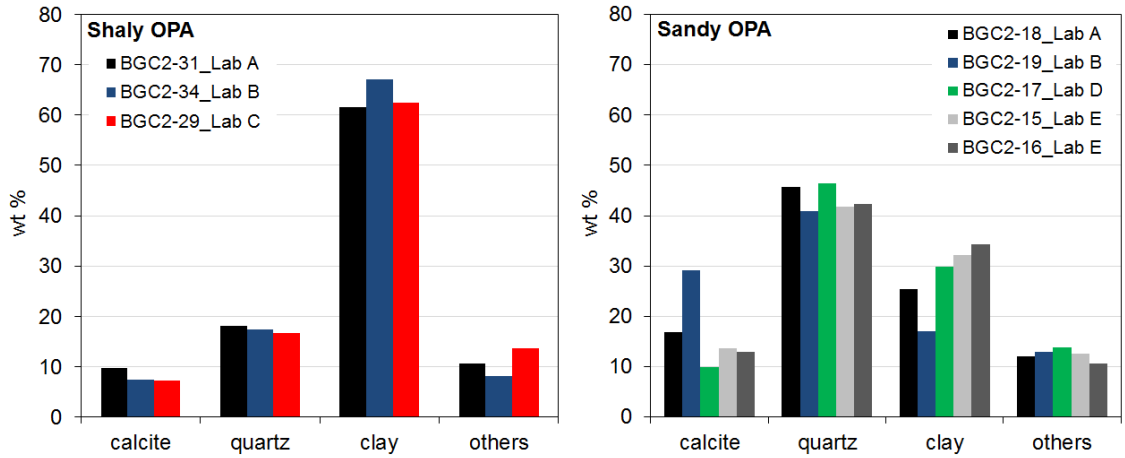

Fig. 8: Average mineralogical composition of the cores used for the preparation of the tested specimens

5 Saturation and consolidation phases

This section aims at analysing the phases of the tests before the shearing of the specimens for both conventional and alternative procedures. The results of each test are presented, and all the issues and deviations from the original procedures are highlighted. Detailed analyses of the swelling pressure and the assessment of the specimens' saturation with B-check tests are presented in the Sections 5.1 and 5.2, respectively.

The following figures (Fig. 9 to Fig. 13) show for each test an overview of the evolution in time of the total stresses (axial σ_a and radial σ_r), back fluid pressure, and strains. A detailed graph for the initial part of the saturation process is presented on the right side of the figures, which is used to estimate the swelling pressures (in the axial and radial directions for the conventional procedure) and check that the specimens did not experience significant swelling deformations. The sign convention used for the strain is positive for compression and negative for expansion. To this regard, it is important to take into account that a volumetric strain of 1 % induces a change of the void ratio equal to 0.012 considering an initial void ratio of 0.200. As described in the Section 2.1, this initial phase is particularly relevant in the conventional testing procedure (adopted by Lab A, Lab B, Lab D, and Lab E) where the tested specimens were subjected to saturation at constant volume, B-check tests, and consolidation before the shearing of the test. For the alternative procedure (adopted only by Lab C), the figures illustrate the initial undrained compaction, the B-check tests, and the eventual further stress change to achieve the desired confining effective stress.

Fig. 9 show the results of the tests performed by Lab A. An isotropic stress (equal to1 MPa) was initially applied before putting the specimens in contact with fluid. In some cases, this stress increase caused a compaction of the specimens (e.g. Test 3 in Fig. 9); however, this deformation can also be induced by the deformation of the apparatus that is not corrected in the very initial loading. Once the specimens were put in contact with the fluid, the axial and radial stresses started to further increase due to the constrained swelling response of the material; the stabilization of the stresses is used to evaluate the swelling pressures in both axial and radial directions. A good stabilization is observed for all the tests performed by Lab A. During this process, the deformations of the specimens were well constrained (negligible strains variations are exhibited). The increase of the back pressure to 2 MPa is always properly carried out after the stabilization of the stresses; only in the Test 1 the back pressure was raised before the achievement of a stable stress condition. Regarding the B-check tests, Lab A had leakage issues; this aspect is analysed in detail in the Section 5.2. For consolidation phase, a loading of the specimens was required in all the tests to achieve the target consolidation stress for the shearing; only in the Test 1 an unloading process was required due to the low target consolidation stress (4 MPa) required for the shearing. Overall, a time interval between 10 and 30 days was required for Lab A to get the specimens ready for the shearing phase.

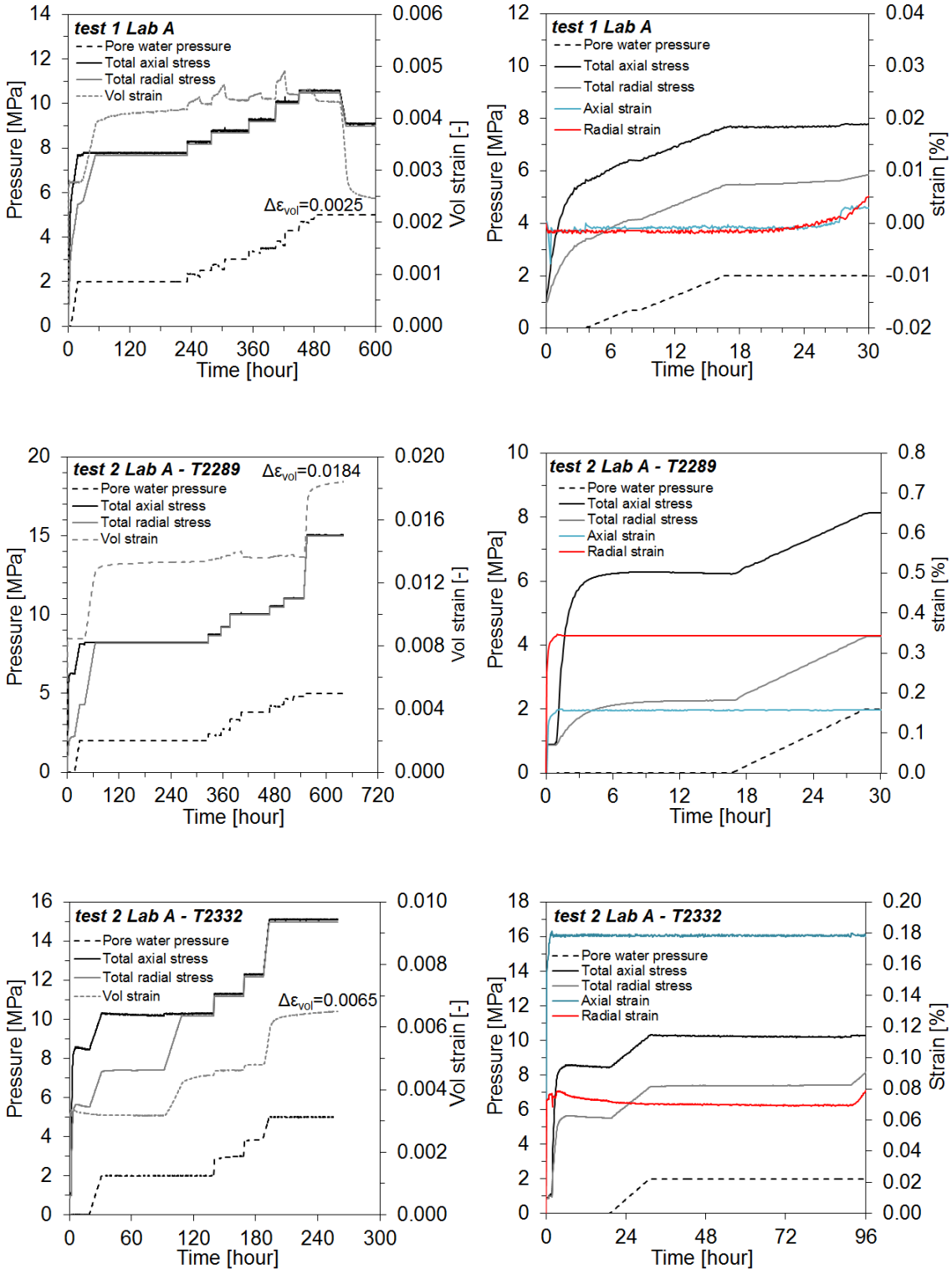

Fig. 9: Saturation and consolidation phases for the tests performed by Lab A

The graphs on the right side focus on the initial part of the saturation process to assess the swelling pressure.

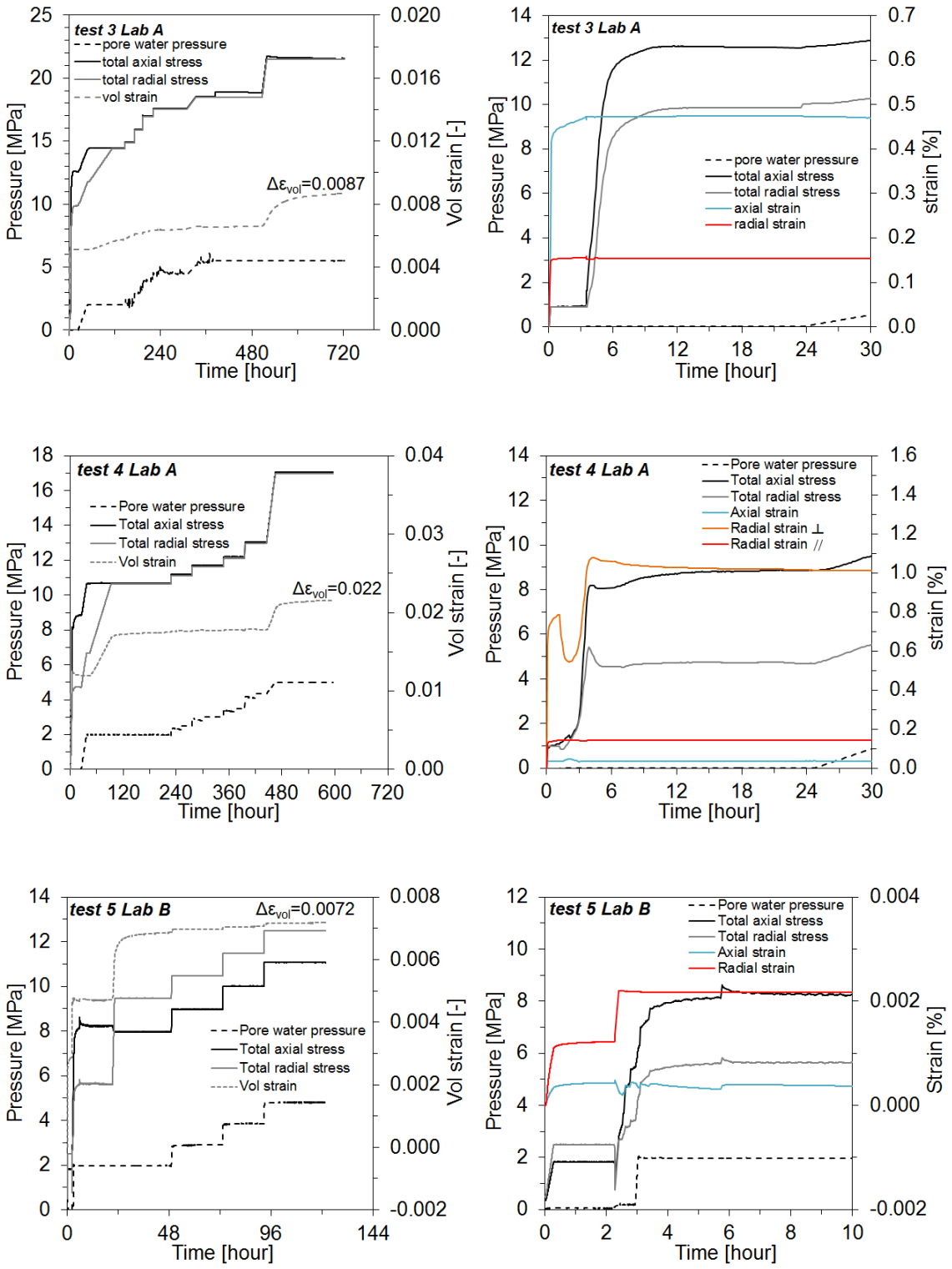
test 3 Lab A
pore water pressure
total axial stress
total radial stress
vol strain
Δεvol=0.0087
Pressure [MPa]
Vol strain [-]
Time [hour]
test 3 Lab A
pore water pressure
total axial stress
total radial stress
axial strain
radial strain
Pressure [MPa]
strain [%]
Time [hour]
test 4 Lab A
Pore water pressure
Total axial stress
Total radial stress
Vol strain
Δεvol=0.022
Pressure [MPa]
Vol strain [-]
Time [hour]
test 4 Lab A
Pore water pressure
Total axial stress
Total radial stress
Axial strain
Radial strain ⊥
Radial strain //
Pressure [MPa]
strain [%]
Time [hour]
test 5 Lab B
Δεvol=0.0072
Pore water pressure
Total axial stress
Total radial stress
Vol strain
Pressure [MPa]
Vol strain [-]
Time [hour]
test 5 Lab B
Pore water pressure
Total axial stress
Total radial stress
Axial strain
Radial strain
Pressure [MPa]
Strain [%]
Time [hour]

Fig. 9: Cont.

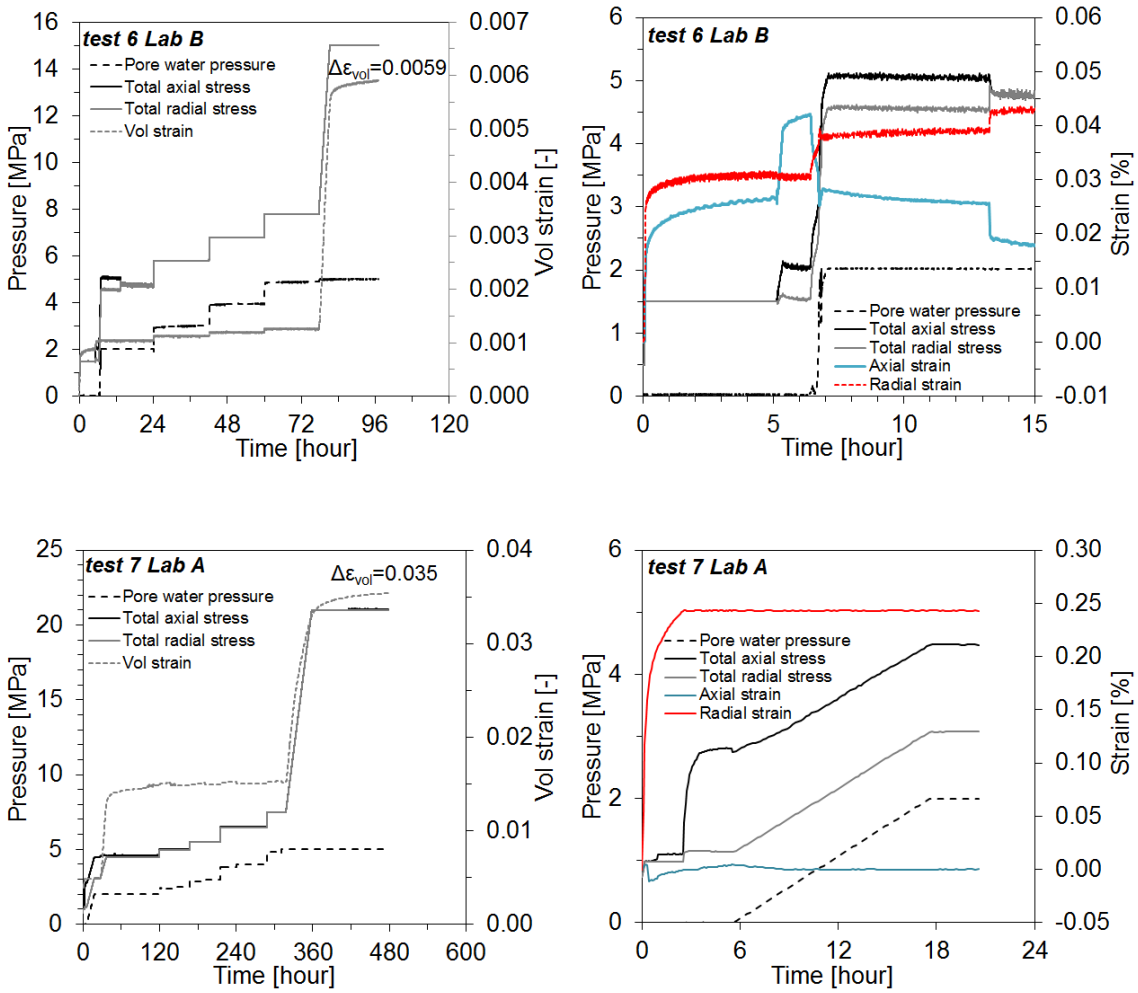
test 6 Lab B
Pore water pressure
Total axial stress
Total radial stress
Vol strain
Δεvol=0.0059
Pressure [MPa]
Vol strain [-]
Time [hour]
test 6 Lab B
Pore water pressure
Total axial stress
Total radial stress
Axial strain
Radial strain
Pressure [MPa]
Strain [%]
Time [hour]
test 7 Lab A
Pore water pressure
Total axial stress
Total radial stress
Vol strain
Δεvol=0.035
Pressure [MPa]
Vol strain [-]
Time [hour]
test 7 Lab A
Pore water pressure
Total axial stress
Total radial stress
Axial strain
Radial strain
Pressure [MPa]
Strain [%]
Time [hour]

Fig. 9: Cont.

Fig. 10 summarizes the results of the tests performed by Lab B. In this case, the conventional testing procedure was not always strictly followed. An initial isotropic stress equal to 1.5 MPa was applied, followed by a deviatoric stress equal to 0.5 MPa. This stress level was slightly greater than requested (cf. Section 2.1). The specimens were then put in contact with the fluid without back pressure and the volumetric deformation was constrained simply by controlling the confining stress. Therefore, the axial and radial stresses were not independently controlled during the saturation process and the swelling pressure could not be evaluated in the two directions. The back pressure was then increased to 2 MPa before the stabilization of the stresses. Regarding the consolidation phase of the tests, the results clearly show a good consolidation process of the specimens. As in the case of Lab A, the tests performed at low consolidation stress (4 MPa, Test 1, Test 4 in Fig. 10) required an unloading process during the consolidation phase to reach the target effective stress. Finally, in Test 5 performed by Lab B an incorrect load cell correction was applied and caused a deviatoric stress component during the initial segment of testing (which was meant to be isotropic). Overall, a time interval between 5 and 8 days was required for Lab B to get the specimens ready for the shearing phase. This short amount of time is related to the good preservation of the specimens during preparation, and in particular to the side-drains used to facilitate fluid pressure equilibration.

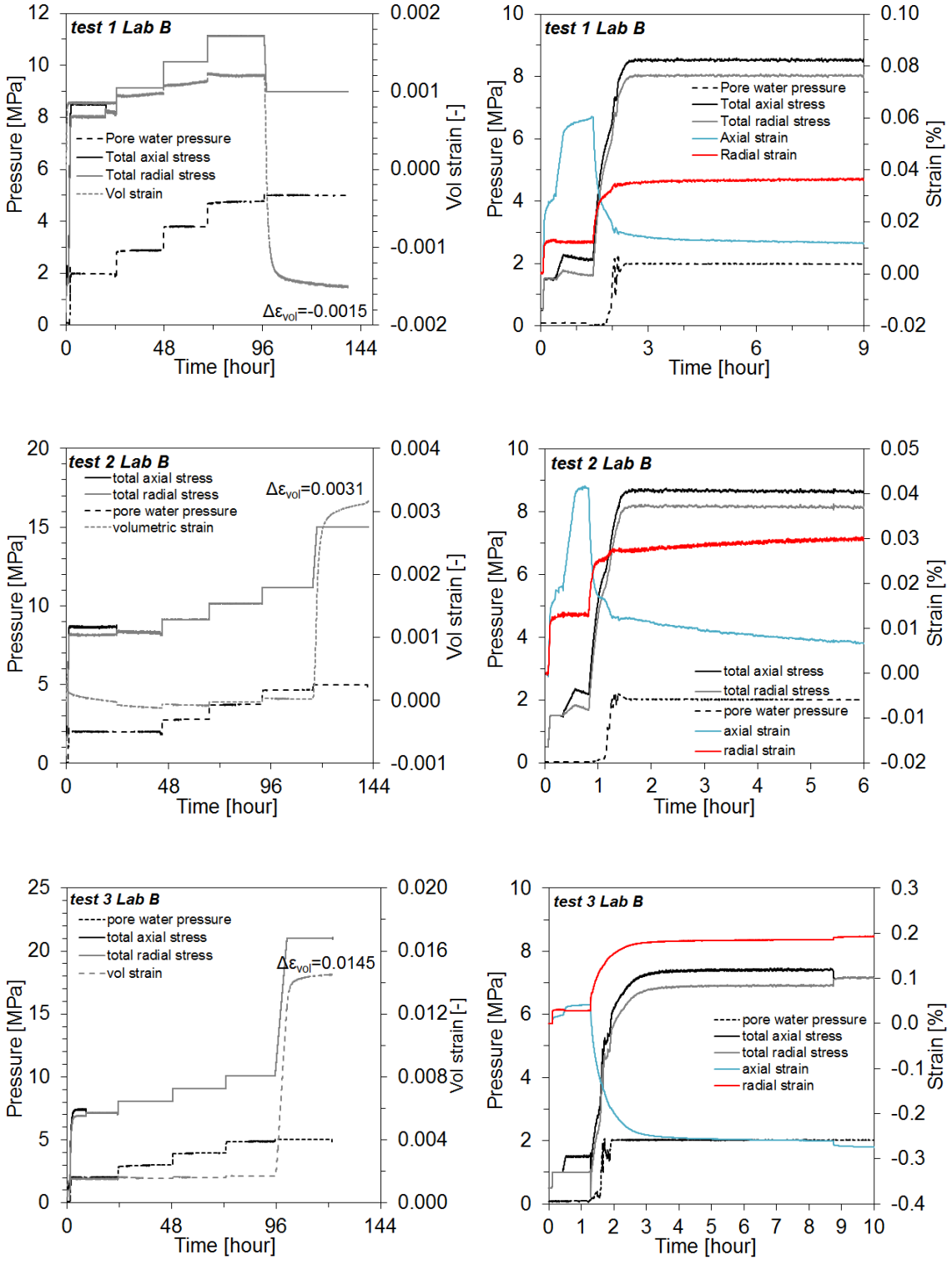

Fig. 10: Saturation and consolidation phases for the tests performed by Lab B

The graphs on the right side focus on the initial part of the saturation process to assess the swelling pressure.

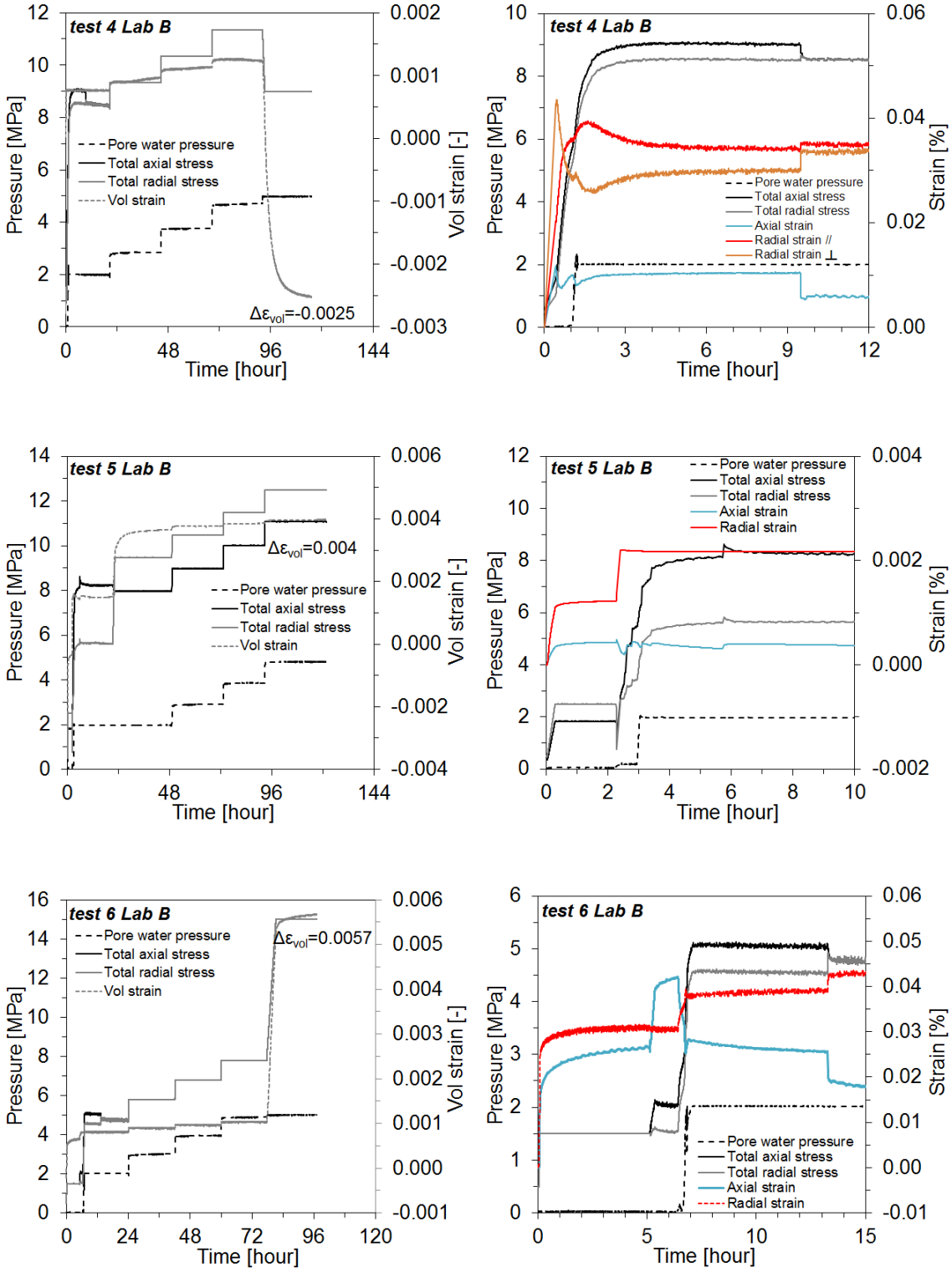
test 4 Lab B
Pore water pressure
Total axial stress
Total radial stress
Vol strain
Δεvol=-0.0025
Pressure [MPa]
Vol strain [-]
Time [hour]
test 4 Lab B
Pore water pressure
Total axial stress
Total radial stress
Axial strain
Radial strain //
Radial strain ⊥
Pressure [MPa]
Strain [%]
Time [hour]
test 5 Lab B
Δεvol=0.004
Pore water pressure
Total axial stress
Total radial stress
Vol strain
Pressure [MPa]
Vol strain [-]
Time [hour]
test 5 Lab B
Pore water pressure
Total axial stress
Total radial stress
Axial strain
Radial strain
Pressure [MPa]
Strain [%]
Time [hour]
test 6 Lab B
Pore water pressure
Total axial stress
Total radial stress
Vol strain
Δεvol=0.0057
Pressure [MPa]
Vol strain [-]
Time [hour]
test 6 Lab B
Pore water pressure
Total axial stress
Total radial stress
Axial strain
Radial strain
Pressure [MPa]
Strain [%]
Time [hour]

Fig. 10: Cont.

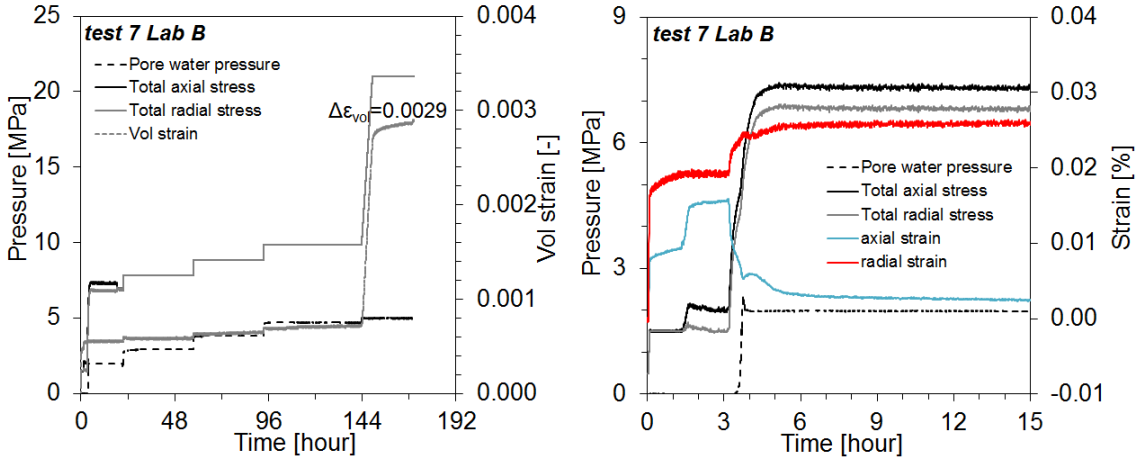
test 7 Lab B
Pore water pressure
Total axial stress
Total radial stress
Vol strain
Δεvol=0.0029
Pressure [MPa]
Vol strain [-]
Time [hour]
test 7 Lab B
Pore water pressure
Total axial stress
Total radial stress
axial strain
radial strain
Pressure [MPa]
Strain [%]
Time [hour]

Fig. 10: Cont.

Fig. 11 shows the results of the tests carried out by Lab C. As the alternative procedure was used in this case, the consolidation of the tested specimens was not carried out. No distinction is done between axial and radial stresses in this case as the specimens were subjected to isotropic loading by only using the confining fluid pressure. In most of the cases, the initial undrained isotropic loading was performed almost instantaneously, resulting in a compaction of the material; the reported data do not fully represent the response of the material as no correction was made for the deformation of the apparatus during this phase. The consequent increase of the pore fluid pressure was usually observed with a delay of few hours; only in Test 3 further loadings of the specimen were required to observe a consistent increase of the pore fluid pressure. In the Tests 2 (BGC2-1-4), 4 (BGC2-1-13), and 12 the increase of the pore fluid pressure induced by the loading was significant (pressure higher than 5 MPa), and a drainage of the pore fluid was necessary to reduce the pressure to achieve the target initial confining stress for the shearing phase; this drainage caused a reduction of the amount of fluid in the pore space which has to be considered for the water content measured after testing. Regarding the B-check test, it was not performed in the Test 10 to avoid perturbation of the specimen before shearing. Overall, a time interval between 4 and 11 days was required to get the specimens ready for the shearing phase of the test.

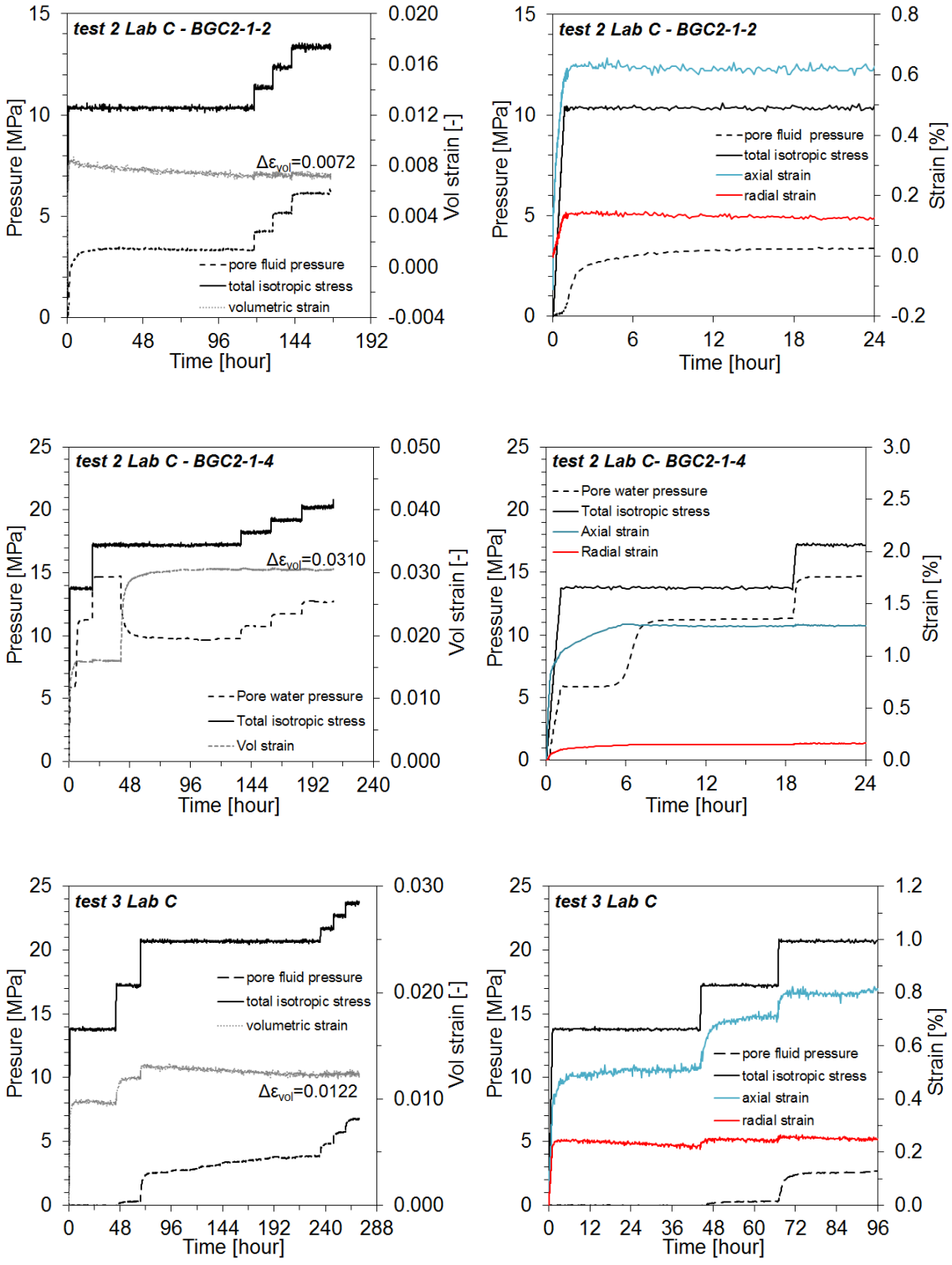

Fig. 11: Saturation and consolidation phases for the tests performed by Lab C

The graphs on the right-side focus on the initial compaction process.

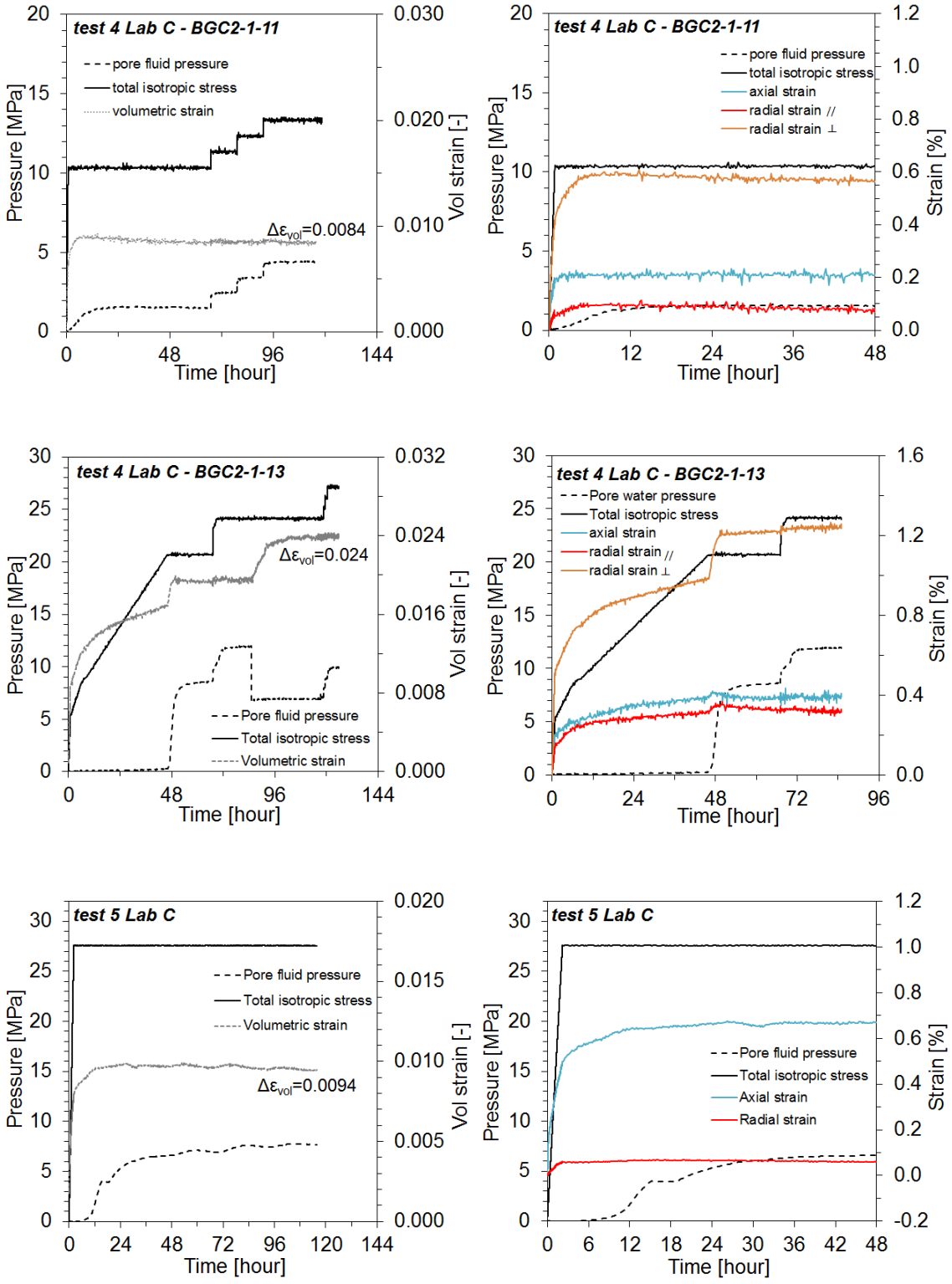
test 4 Lab C - BGC2-1-11
pore fluid pressure
total isotropic stress
volumetric strain
Δεvol=0.0084
Pressure [MPa]
Vol strain [-]
Time [hour]
test 4 Lab C - BGC2-1-11
pore fluid pressure
total isotropic stress
axial strain
radial strain //
radial strain ⊥
Pressure [MPa]
Strain [%]
Time [hour]
test 4 Lab C - BGC2-1-13
Δεvol=0.024
Pore fluid pressure
Total isotropic stress
Volumetric strain
Pressure [MPa]
Vol strain [-]
Time [hour]
test 4 Lab C - BGC2-1-13
Pore water pressure
Total isotropic stress
axial strain
radial strain //
radial srain ⊥
Pressure [MPa]
Strain [%]
Time [hour]
test 5 Lab C
Pore fluid pressure
Total isotropic stress
Volumetric strain
Δεvol=0.0094
Pressure [MPa]
Vol strain [-]
Time [hour]
test 5 Lab C
Pore fluid pressure
Total isotropic stress
Axial strain
Radial strain
Pressure [MPa]
Strain [%]
Time [hour]

Fig. 11: Cont.

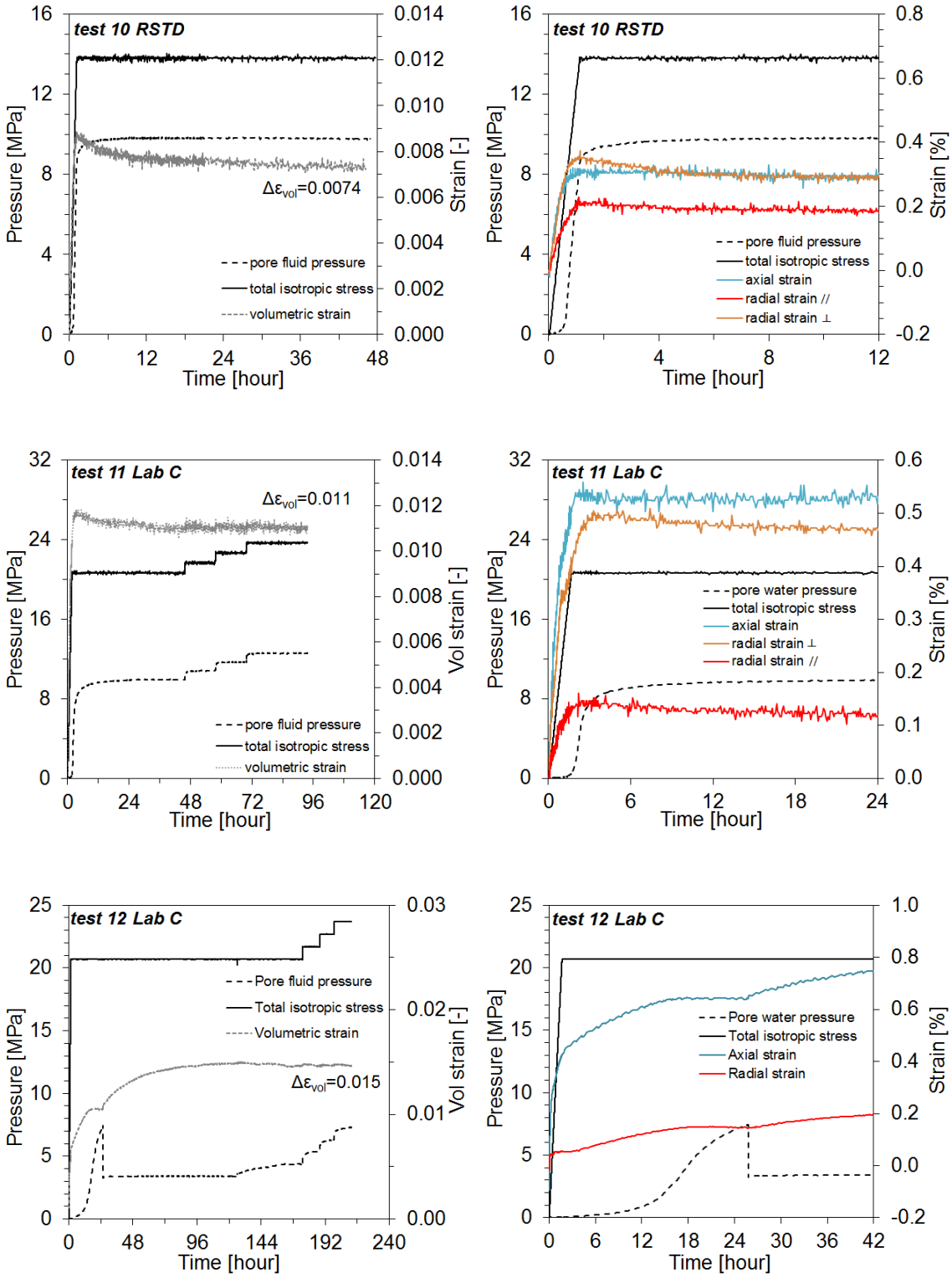
test 10 RSTD
Pressure [MPa]
Strain [-]
Time [hour]
Δεvol=0.0074
pore fluid pressure
total isotropic stress
volumetric strain
test 10 RSTD
Pressure [MPa]
Strain [%]
Time [hour]
pore fluid pressure
total isotropic stress
axial strain
radial strain //
radial strain ⊥
test 11 Lab C
Pressure [MPa]
Vol strain [-]
Time [hour]
Δεvol=0.011
pore fluid pressure
total isotropic stress
volumetric strain
test 11 Lab C
Pressure [MPa]
Strain [%]
Time [hour]
pore water pressure
total isotropic stress
axial strain
radial strain ⊥
radial strain //
test 12 Lab C
Pressure [MPa]
Vol strain [-]
Time [hour]
Pore fluid pressure
Total isotropic stress
Volumetric strain
Δεvol=0.015
test 12 Lab C
Pressure [MPa]
Strain [%]
Time [hour]
Pore water pressure
Total isotropic stress
Axial strain
Radial strain

Fig. 11: Cont.

Fig. 12 illustrates the results of the tests performed by Lab D. The initial isotropic loading (1 MPa) induced a small compaction of the specimens; during the saturation the volumetric deformations were well constrained. However, the back pressure was always increased to 2 MPa before the stabilization of the stresses. Anomalous variations of the volumetric strain (expansion) and the pore fluid pressure (drop) before the starting of the B-check tests were observed in Test 6, which are however not explained in the provided report. In Test 8, experimental data are missing in the initial phase of the saturation process due to a technical issue. However, the deformations were well constrained during the saturation process. The consolidation phase was properly performed in all the tests. Overall, a time interval between 12 and 20 days was required to get the specimens ready for the shearing phase of the test.

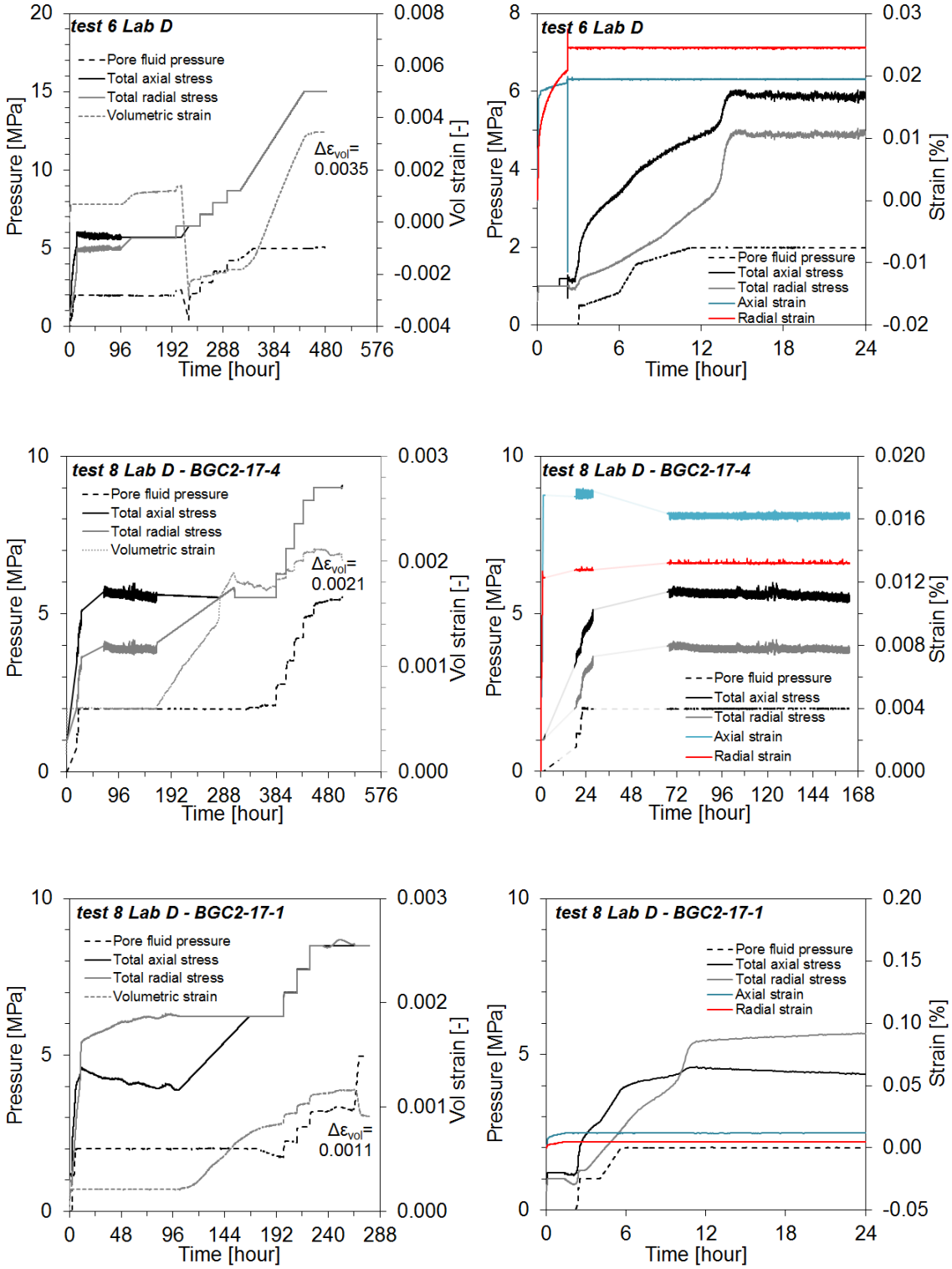

Fig. 12: Saturation and consolidation phases for the tests performed by Lab D

The graphs on the right side focus on the initial part of the saturation process to assess the swelling pressure.

As mentioned above, Lab E used a "hybrid" approach between the conventional and the unconventional procedures, respectively. An initial stress of 4 MPa was always applied before starting the saturation of the specimens (as the water potential of the specimens equilibrated in the desiccators was measured as approximately minus 4 MPa). Hence this value was higher than the suggested value (0.5 – 1 MPa) and complicated the evaluation of the swelling pressure. Moreover, issues with the transducers for the measurement of the radial strain were reported. Extremely small values were recorded during the phases of the tests before shearing. Hence, the volumetric response presented in Fig. 13 was significantly underestimated. Overall, a time interval between 12 and 20 days was required to get the specimens ready for the shearing phase of the test.

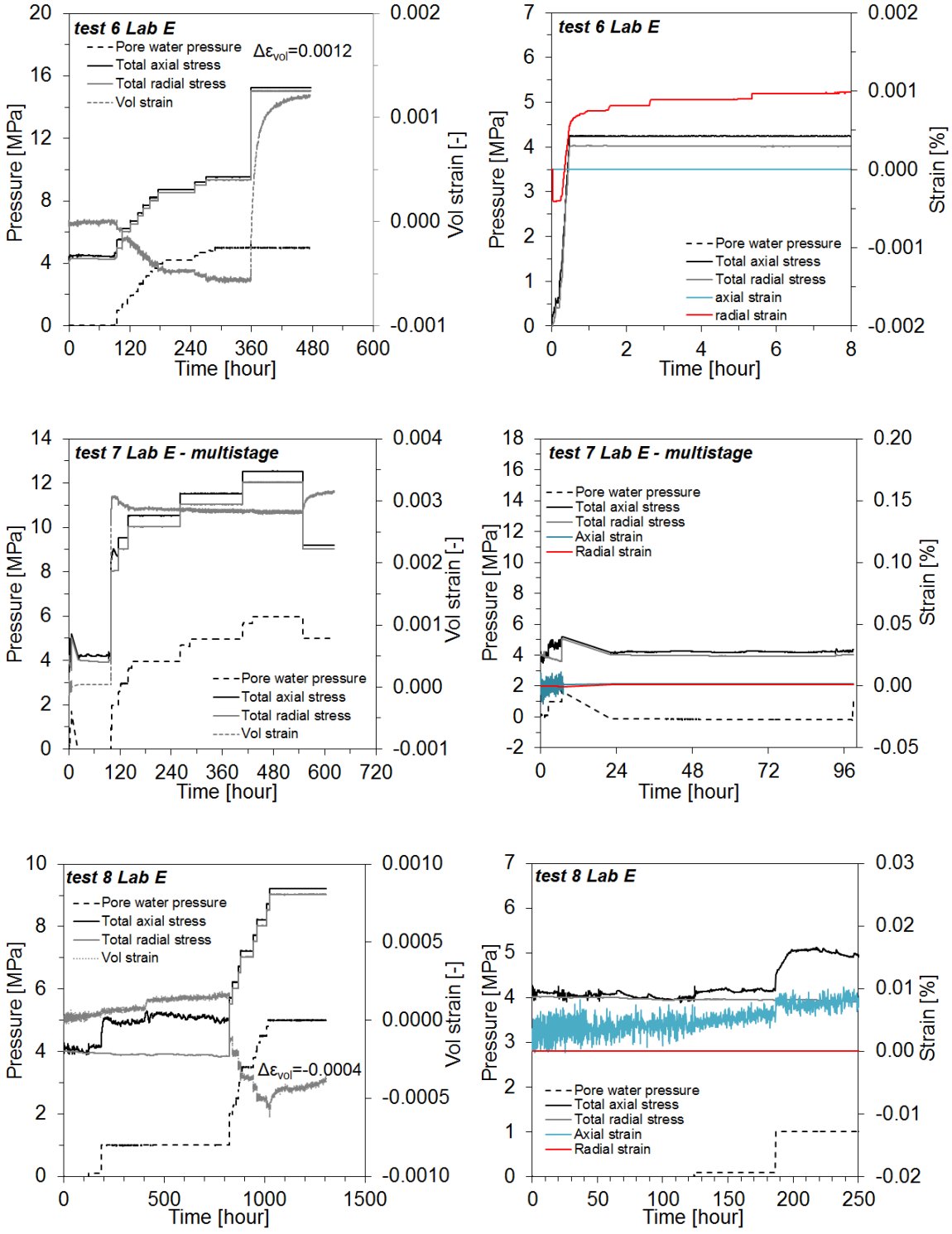

Fig. 13: Saturation and consolidation phases for the tests performed by Lab E

5.1 Swelling pressure

Fig. 14 illustrates the measured swelling pressure in terms of mean effective stress p' as a function of the specimens' water content before starting the tests. The mean effective stress is defined as follow:

$$p' = \frac{\sigma'_a + 2\sigma'_r}{3}$$

where σ_a' and σ_r' are the effective axial and confining stresses respectively.

The values measured by Lab B should be considered with caution as the axial and radial stresses cannot be independently controlled due to a feature of the testing set-up (see the report for more details). The results provided by Lab C and Lab E are not included as they pre-conditioned their specimens in desiccators (alternative testing procedure).

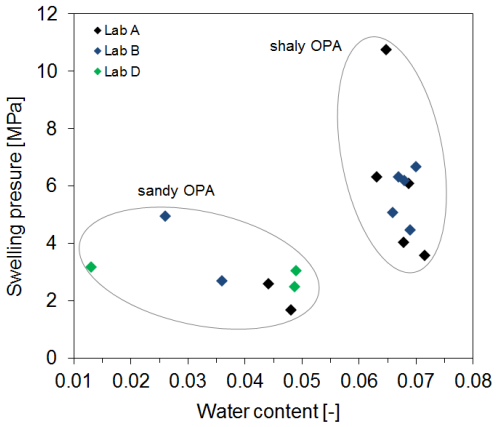

Fig. 14: Relationship between measured swelling pressure and water content (w) of the samples before testing

5.2 B-check test

The B-check test consisted in the assessment of Skempton's B coefficient by applying an isotropic loading in undrained conditions and measuring the corresponding increment of the pore fluid pressure. The measurements of the B coefficient were always performed after the saturation phase. The performed loading steps were in the range between 0.5 or 1 MPa. No correction was applied to the values of the B coefficients presented in the following figures (Fig. 15 to Fig. 20). Fig. 20 summarizes the obtained values of the B coefficients as function of the mean effective stress (p'); each point refers to the average value obtained from the different measurements along with the corresponding interval. As anticipated in the previous sections, Lab A had difficulties with these measurements as the fluid pressure was constantly decreasing at each step after the increase of the stress (Fig. 15). Fluid leakages through the nitrile rubber membrane were considered as a possible cause of this feature. For this reason, a Viton rubber membrane was adopted to perform the Test 2 (T2332, Fig. 15), where good measurements of the B coefficient were obtained. However, a nitrile membrane was used to protect the specimens from the confining fluid in all the other tests performed by Lab A. Regarding the measurements of the Lab B, Lab C, Lab D, and Lab E showed a good response during the B-check tests. Constant fluid pressure was typically observed after the increase of the mean total stress. Moreover, differences between two consecutive measurements of the B coefficients were lower than 0.1; this feature is a good indication that the specimens were well saturated.

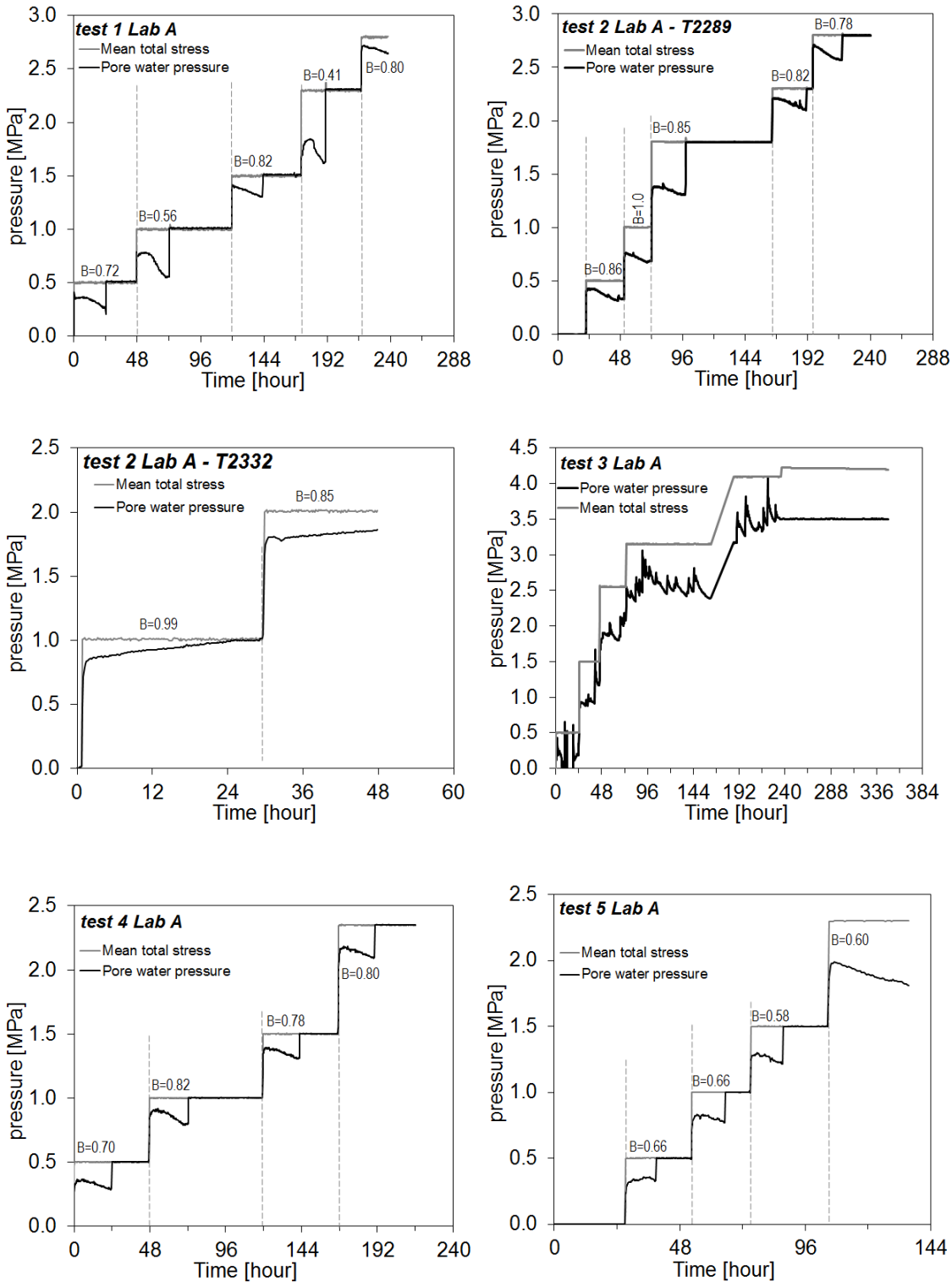

Fig. 15: B-check measurements for the tests performed by Lab A

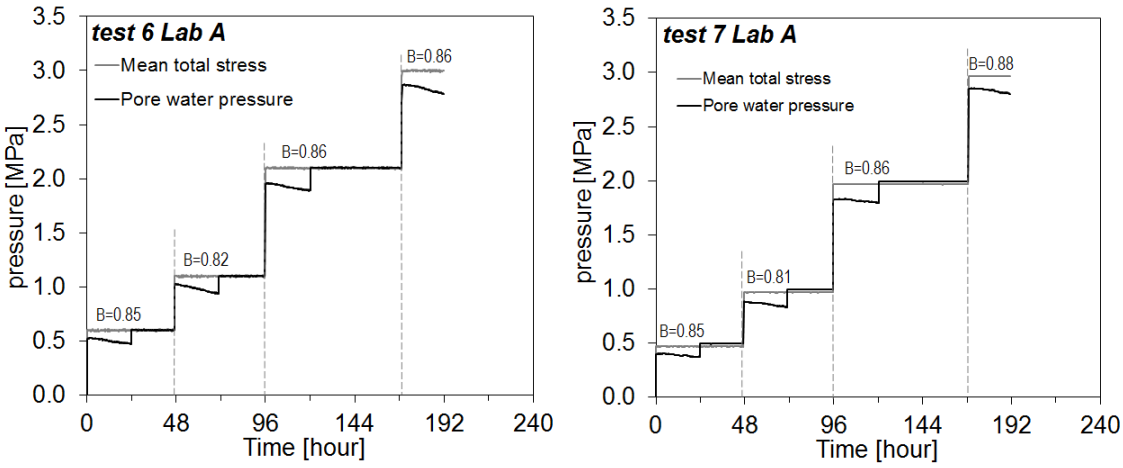
test 6 Lab A
Mean total stress
Pore water pressure
B=0.85
B=0.82
B=0.86
B=0.86
pressure [MPa]
Time [hour]
test 7 Lab A
Mean total stress
Pore water pressure
B=0.85
B=0.81
B=0.86
B=0.88
pressure [MPa]
Time [hour]

Fig. 15: Cont.

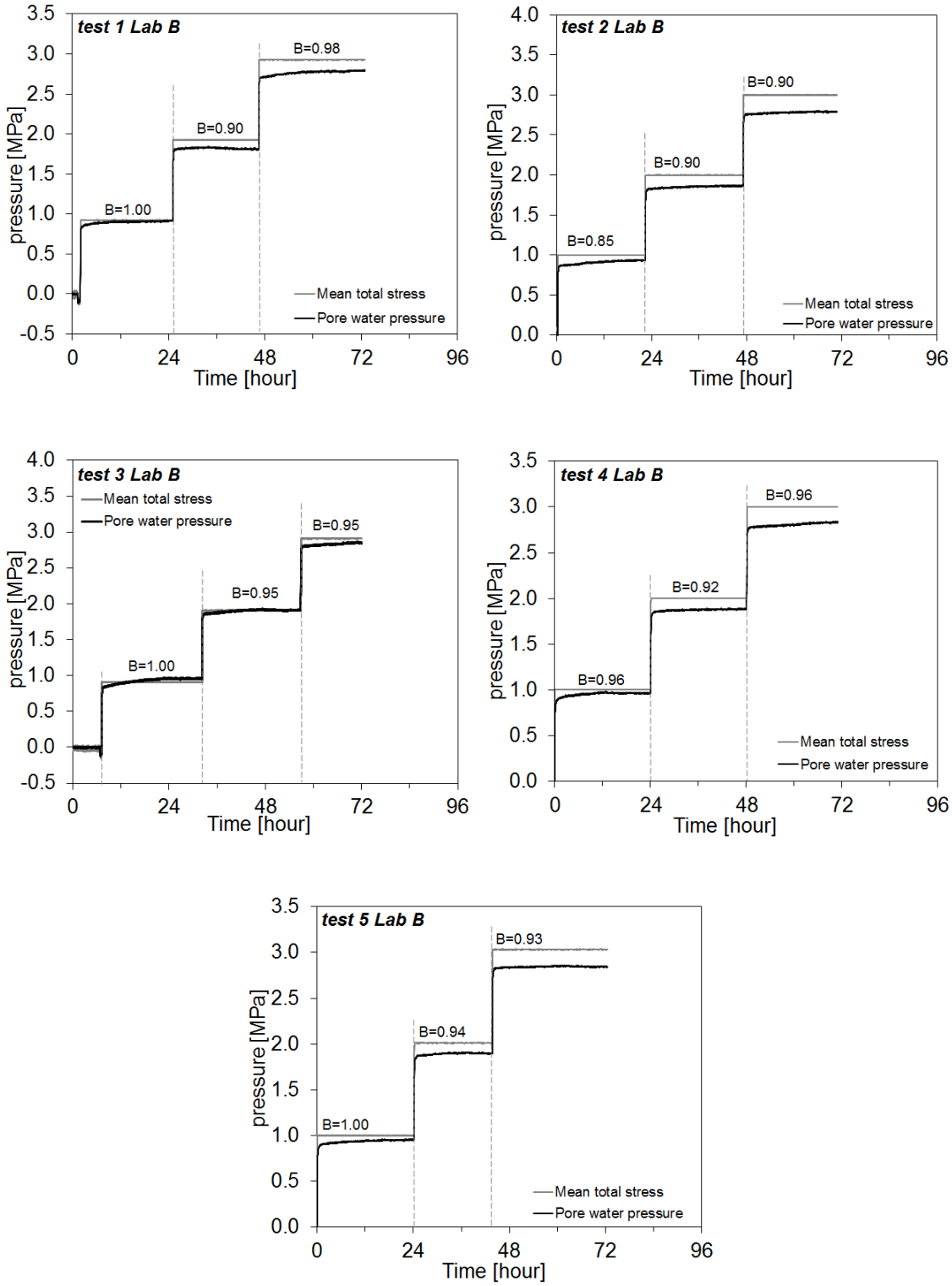

Fig. 16: B-check measurements for the tests performed by Lab B

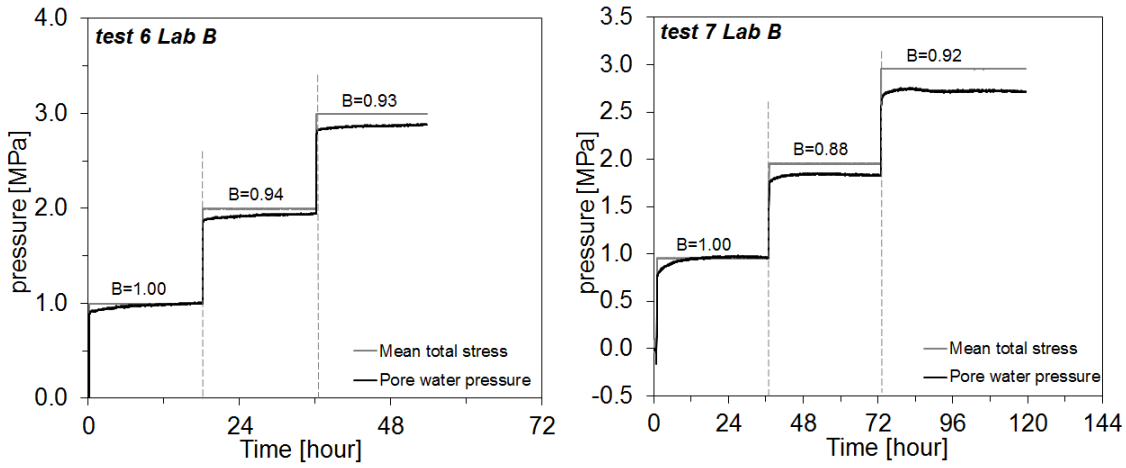
test 6 Lab B
B=1.00
B=0.94
B=0.93
Mean total stress
Pore water pressure
pressure [MPa]
Time [hour]
test 7 Lab B
B=1.00
B=0.88
B=0.92
Mean total stress
Pore water pressure
pressure [MPa]
Time [hour]

Fig. 16: Cont.

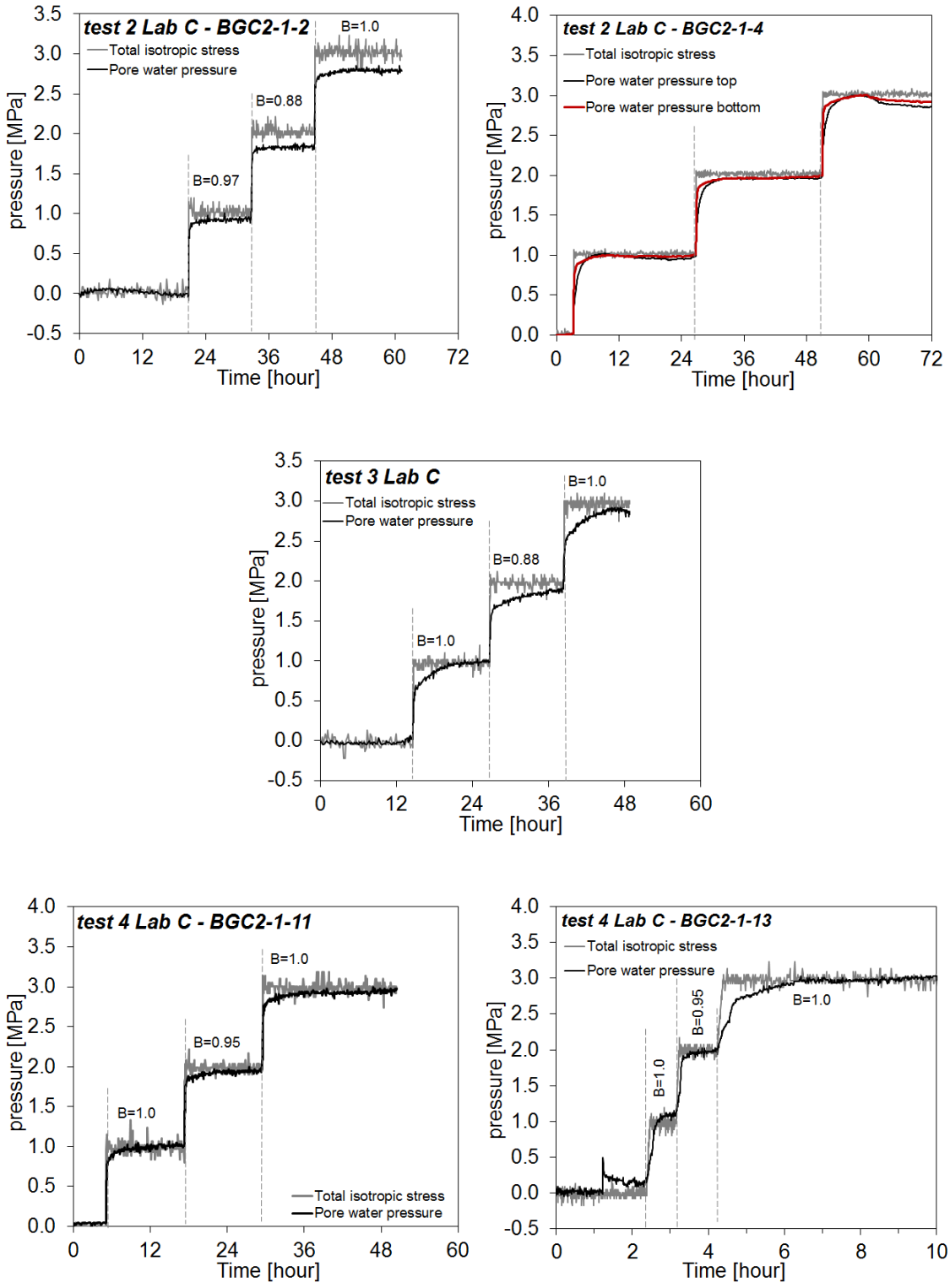

Fig. 17: B-check measurements for the tests performed by Lab C

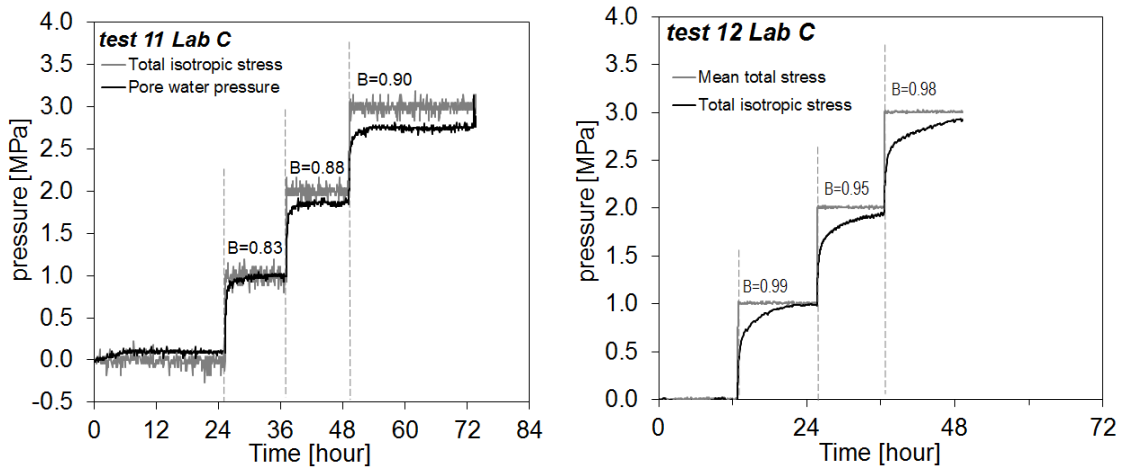

Fig. 17: Cont.

In the Lab C Test 2 (BGC2-1-4) in Fig. 17, two pressures transducers placed at the top and bottom of the specimen were used. The transducers recorded very similar evolutions of the back pressure at the two sides.

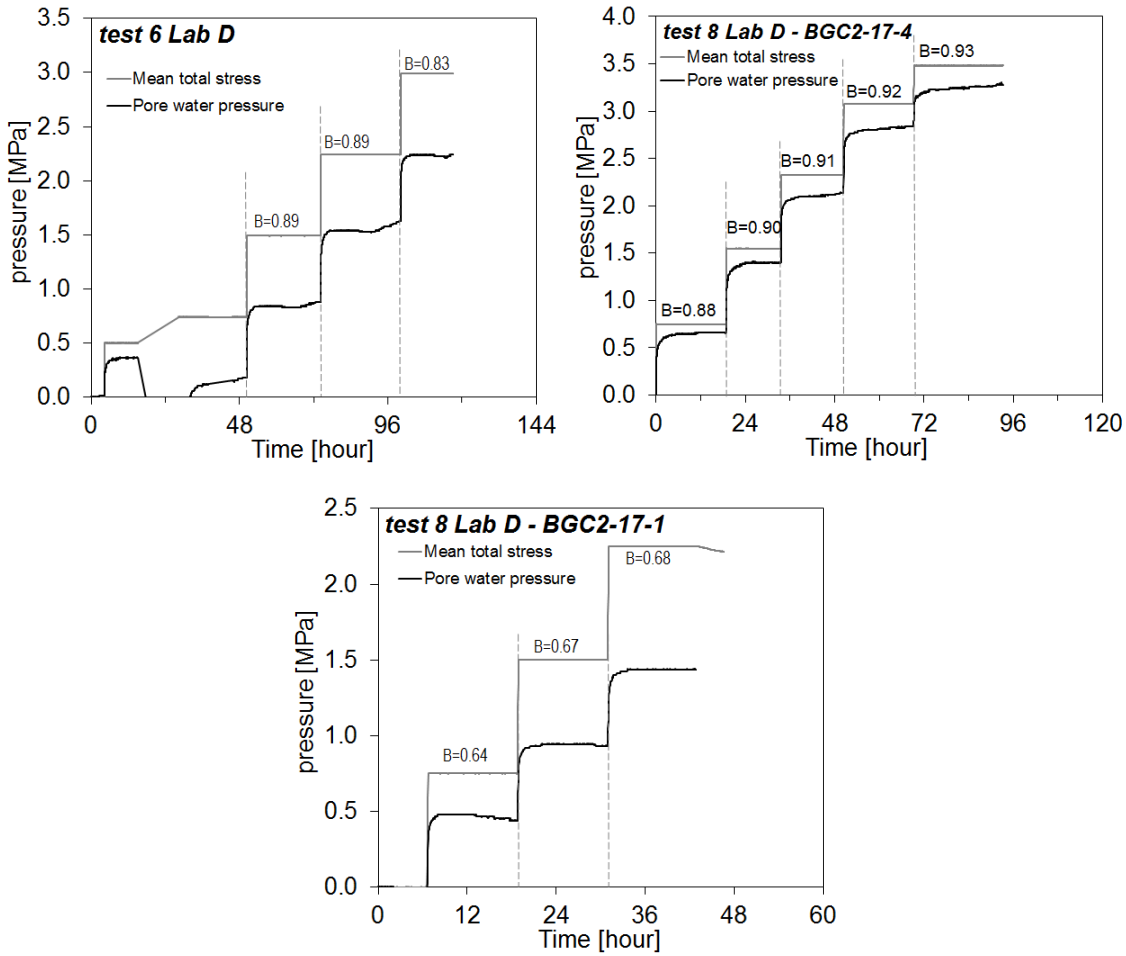

Fig. 18: B-check measurements for the tests performed by Lab D

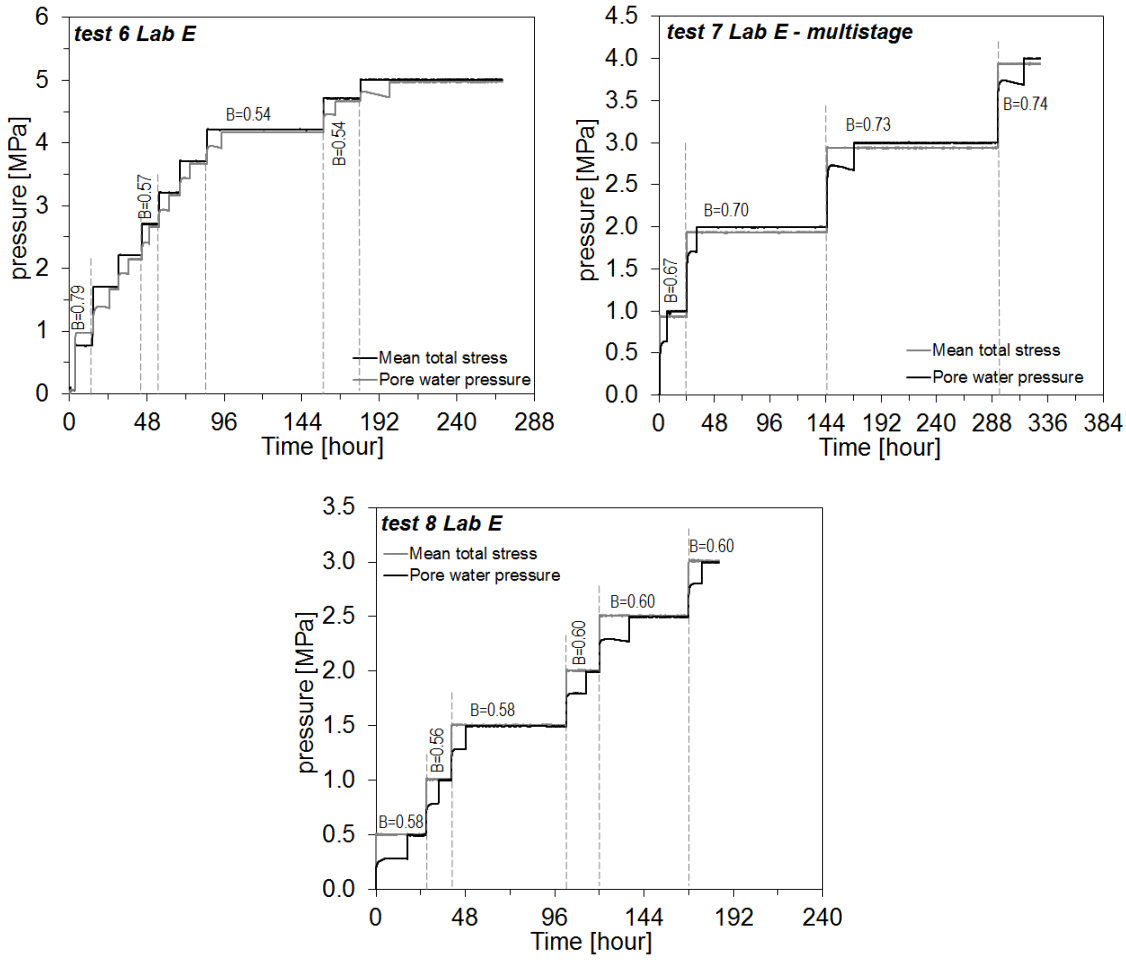

Fig. 19: B-check measurements for the tests performed by Lab E

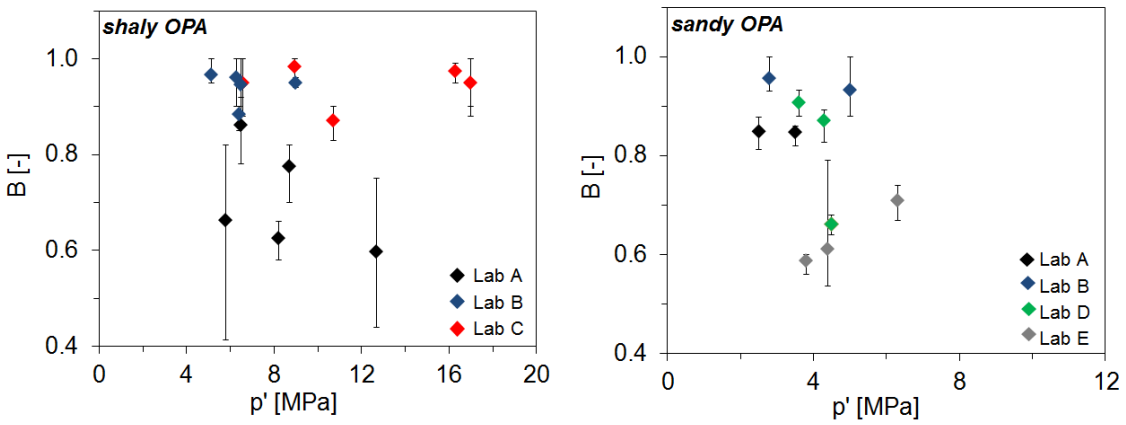

Fig. 20: Measured values of the B coefficient for the tests performed by the different contractors

6 Shearing phase

This section aims at providing a diagnostic analysis of the shearing phase of each test. The following plots are presented in the planes: q-ε_a, q-p', Δu_w-ε_a, q-ε_r(-ε_{vol}), q-Δu_w, q-AB, where q is the deviatoric stress (defined here as the axial stress σ_a minus the radial stress σ_r), p' is the mean effective stress, ε_a is the axial strain, ε_r is the radial strain, ε_{vol} is the volumetric strain, Δu_w is the variation of pore fluid pressure, AB is the ratio between the Δu_w and q. Moreover, the maximum values of q, Δu_w, and AB during the shearing are also illustrated on the different graphs. These values are used in the section for the evaluation of the strength envelopes. The results are sorted by contractors; reference to the Tab. 1 is required to identify tested facies, bedding orientation, and type of stress path. When available, pictures of the specimens after testing are included in the figures to evaluate the failure mode.

6.1 Lab A tests

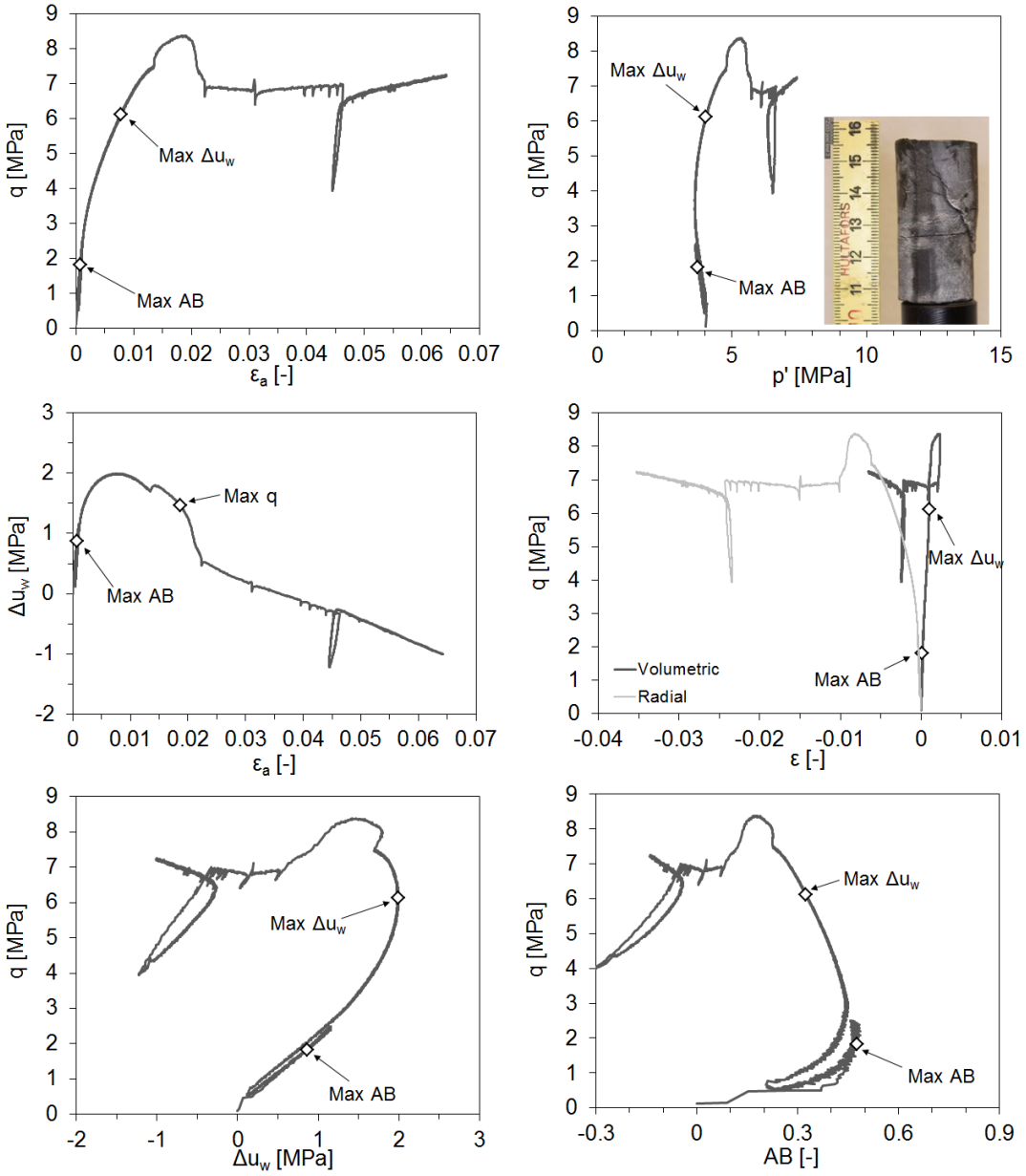

Fig. 21: Results Test 1 Lab A at p'_{in} = 4.0 MPa

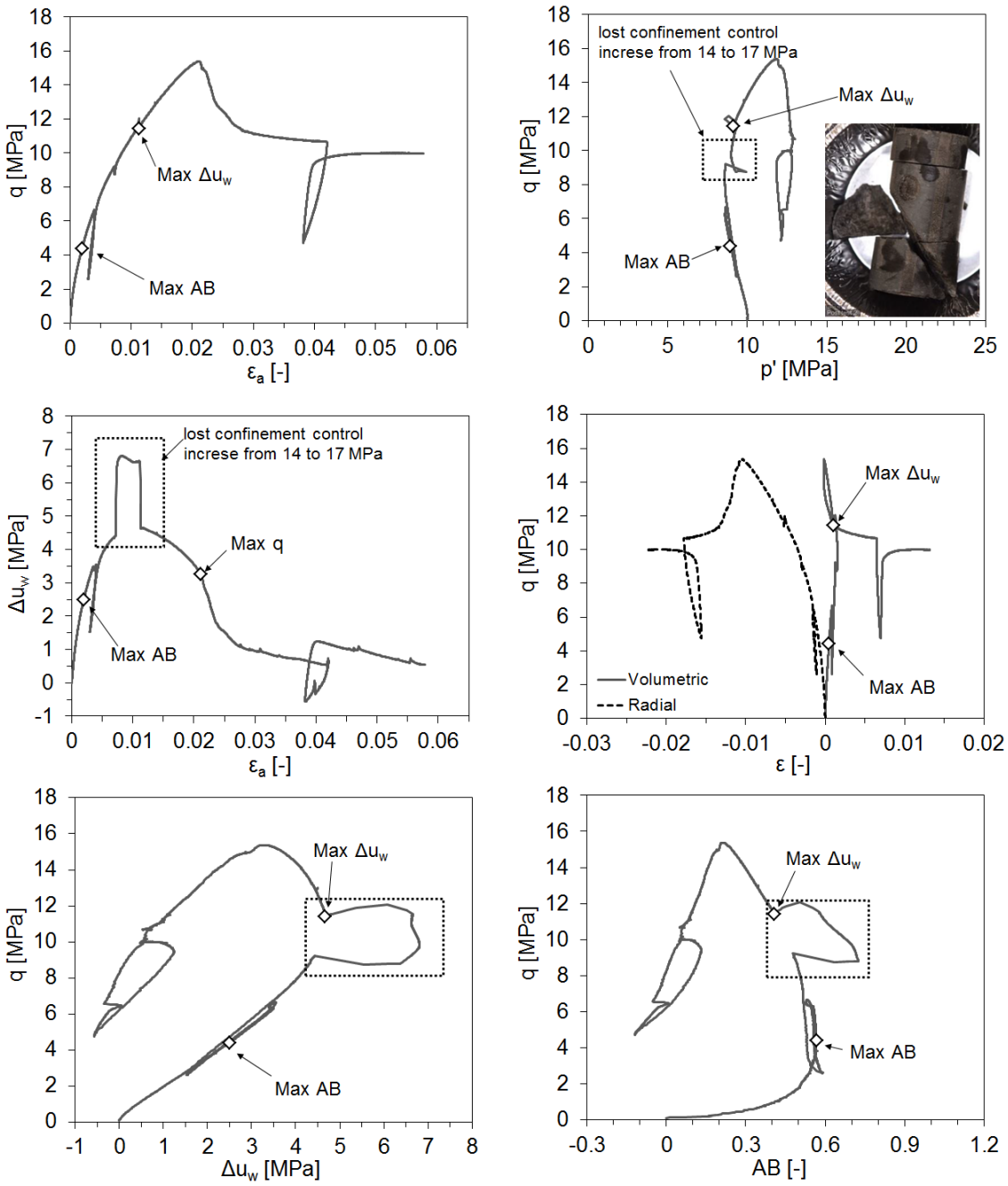

Fig. 22: Results Test 2 (T2289) Lab A at p'_{in} =10 MPa

During the shearing phase of the Test 2 (T2289) by Lab A (Fig. 22), the control of the confining stress was lost and an increase of the total radial stress from 14 MPa to 17 MPa occurred (dashed square in the graphs). After 23 minutes, the confining stress was re-established to its correct value. This issue caused an increase of the pore fluid pressure, which was not considered for the evaluation of the maximum Δu_w.

Fig. 23 shows the results of the test (Test 2 T2332) performed with the Viton rubber membrane. The outcomes are consistent with those observed in the Test 2 T2289 performed with the nitrile membrane. This aspect suggests a minor impact of possible leakages through the nitrile membrane on the evolution of the fluid pressure during the shearing of the specimen.

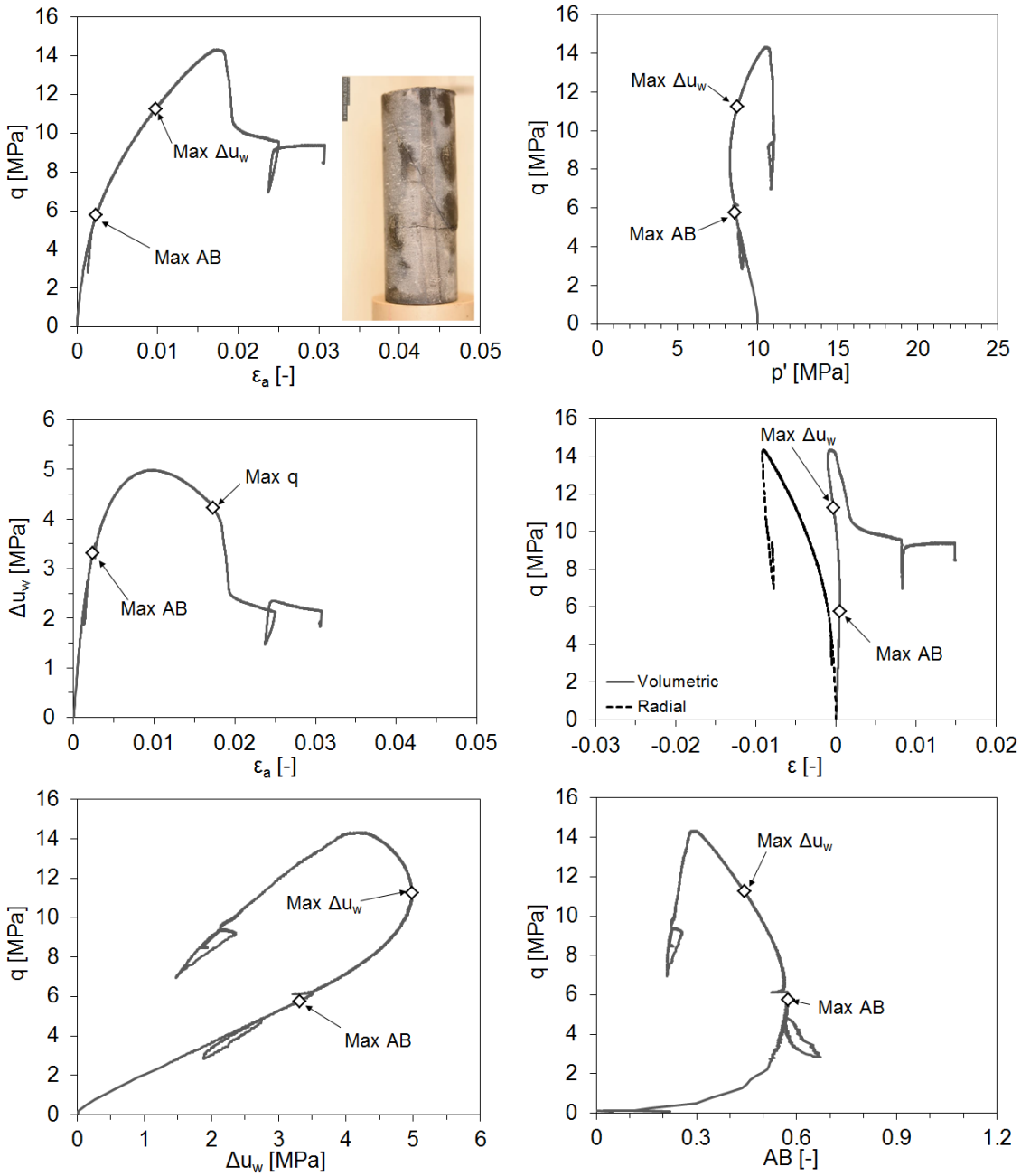

Fig. 23: Results Test 2 (T2332) Lab A at p'_{in} =10 MPa

In Fig. 24 (Test 3 by Lab A) a good achievement of the post-peak conditions after failure was not obtained. Considering the response observed in Fig. 22, the specimen in the Test 3 should have been sheared to an axial strain of at least 0.04.

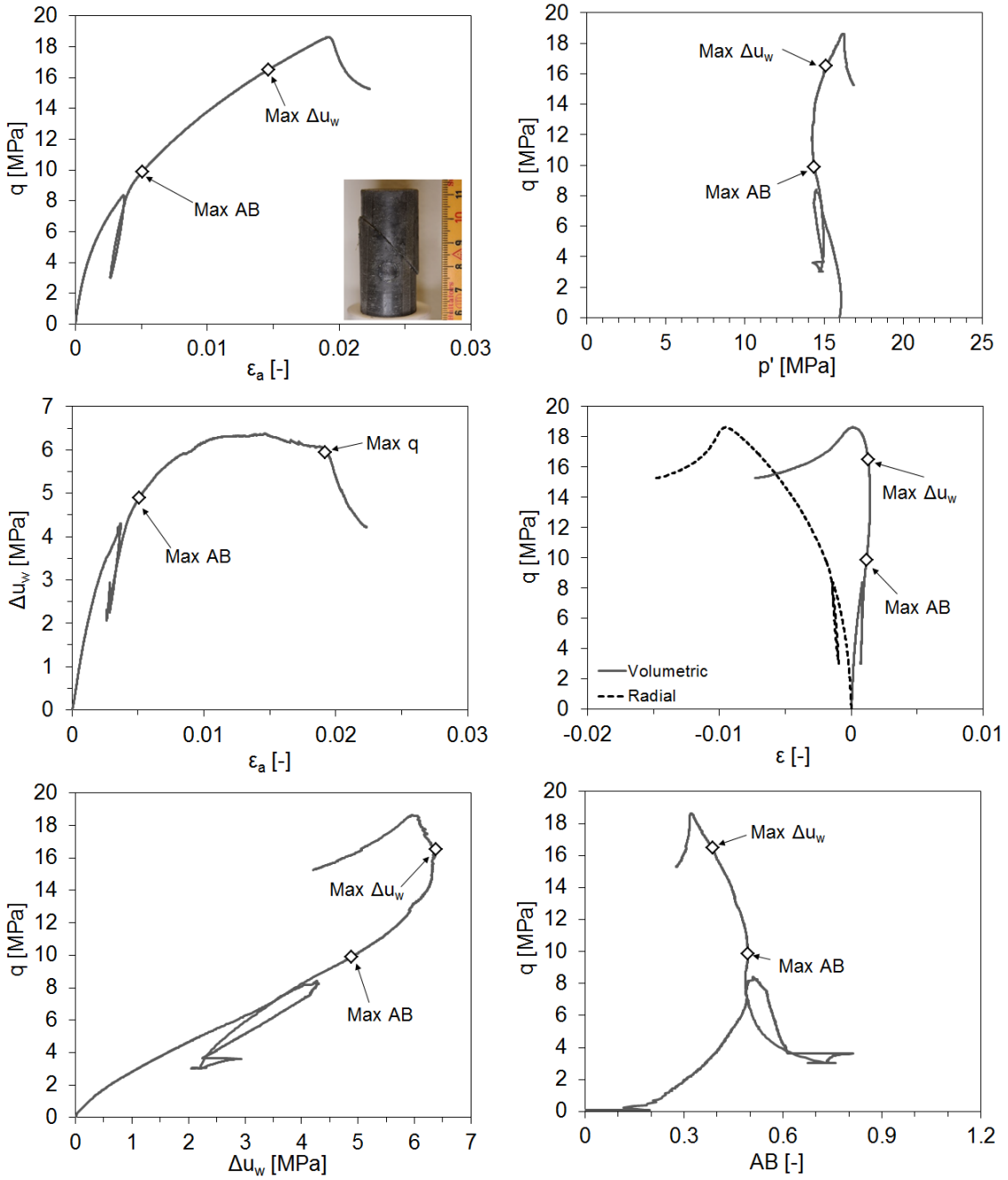

Fig. 24: Results Test 3 Lab A at p'_{in} = 16 MPa

Fig. 25 shows the response of the specimen tested parallel to the bedding (P-test). The main differences compared to the S-tests are related to the stress-strain response, stress path, and development of pore fluid pressure. These aspects are analysed in detail in Section 8.

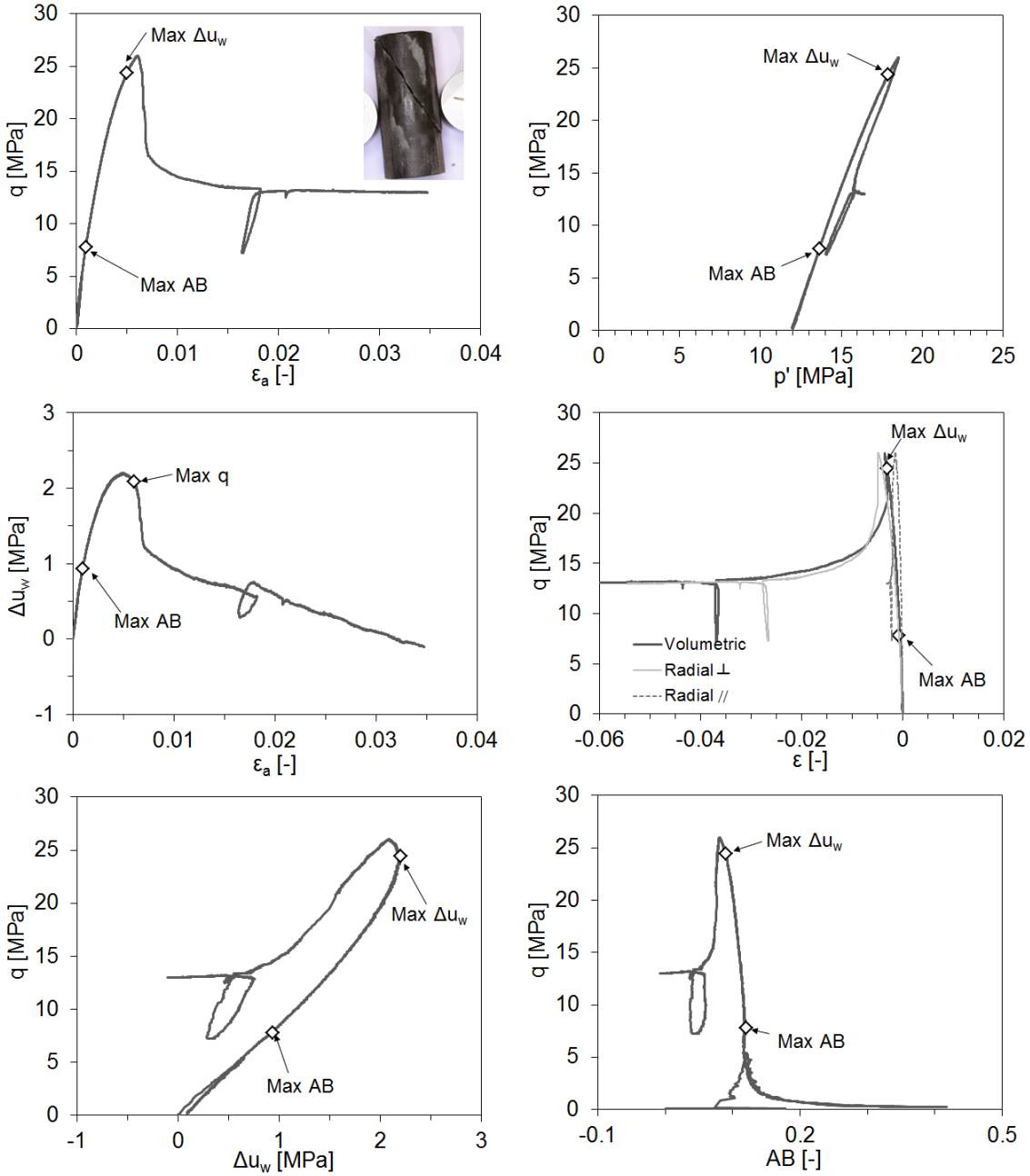

Fig. 25: Results Test 4 Lab A at p'_{in} = 12 MPa (P test)

The Test 5 was performed according to different stress paths than the previous CTC tests. Lab A (Fig. 26) adopted a conventional triaxial extension (CTE) stress path, where the axial stress was kept constant and the radial stress was progressively increased until the failure of the specimen.

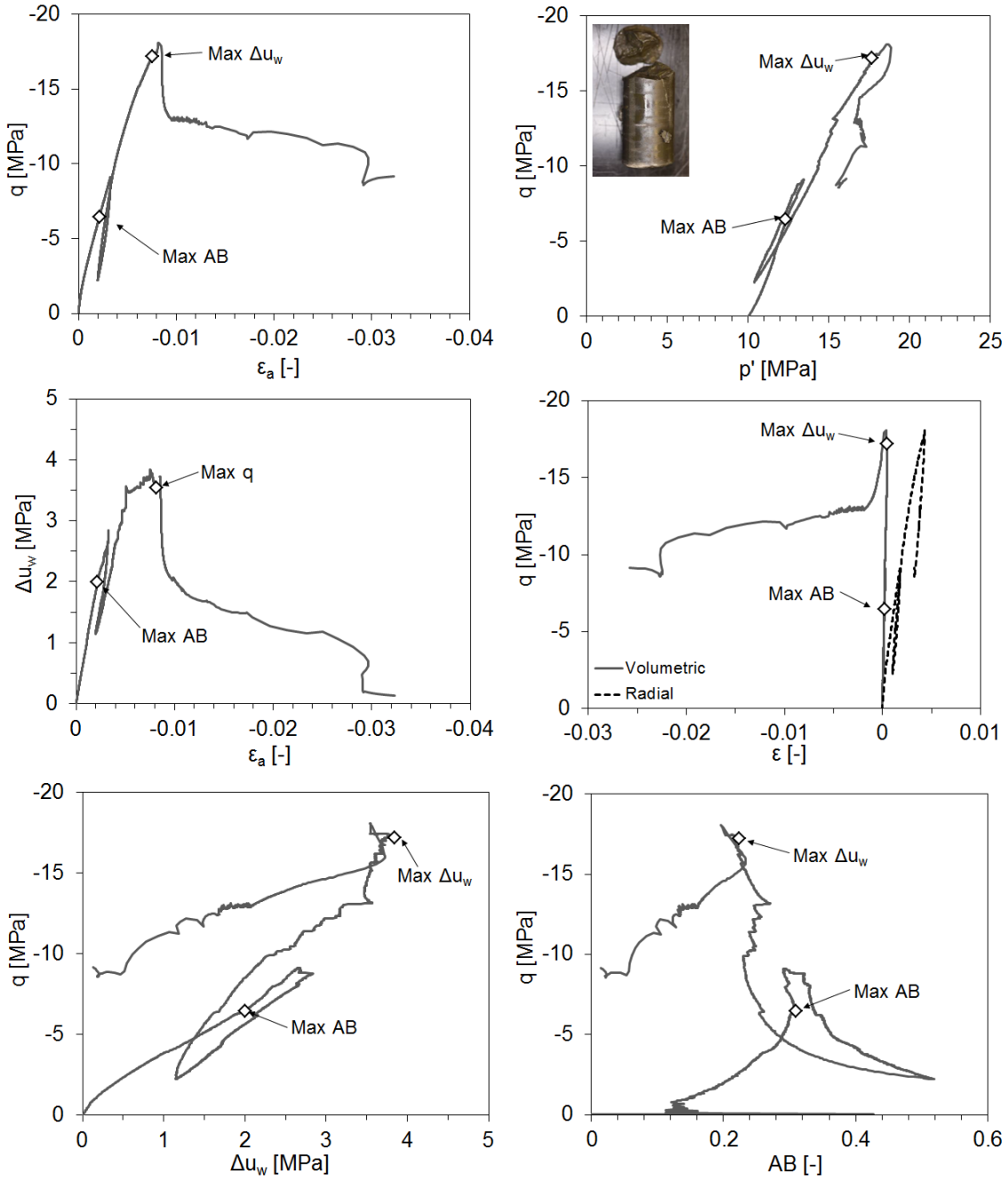

Fig. 26: Results of the CTE test Lab A (Test 5) at p'_{in} = 10 MPa

Fig. 27 and Fig. 28 illustrate the results of the tests carried out on the sandy OPA. Compared to the results observed for the shaly OPA in the previous figures, a clear brittle failure is not observed in this case. Moreover, the picture of the specimens after the tests does not show the development of a clear failure surface as in the case of the shaly specimens (see Fig. 21 to Fig. 24).

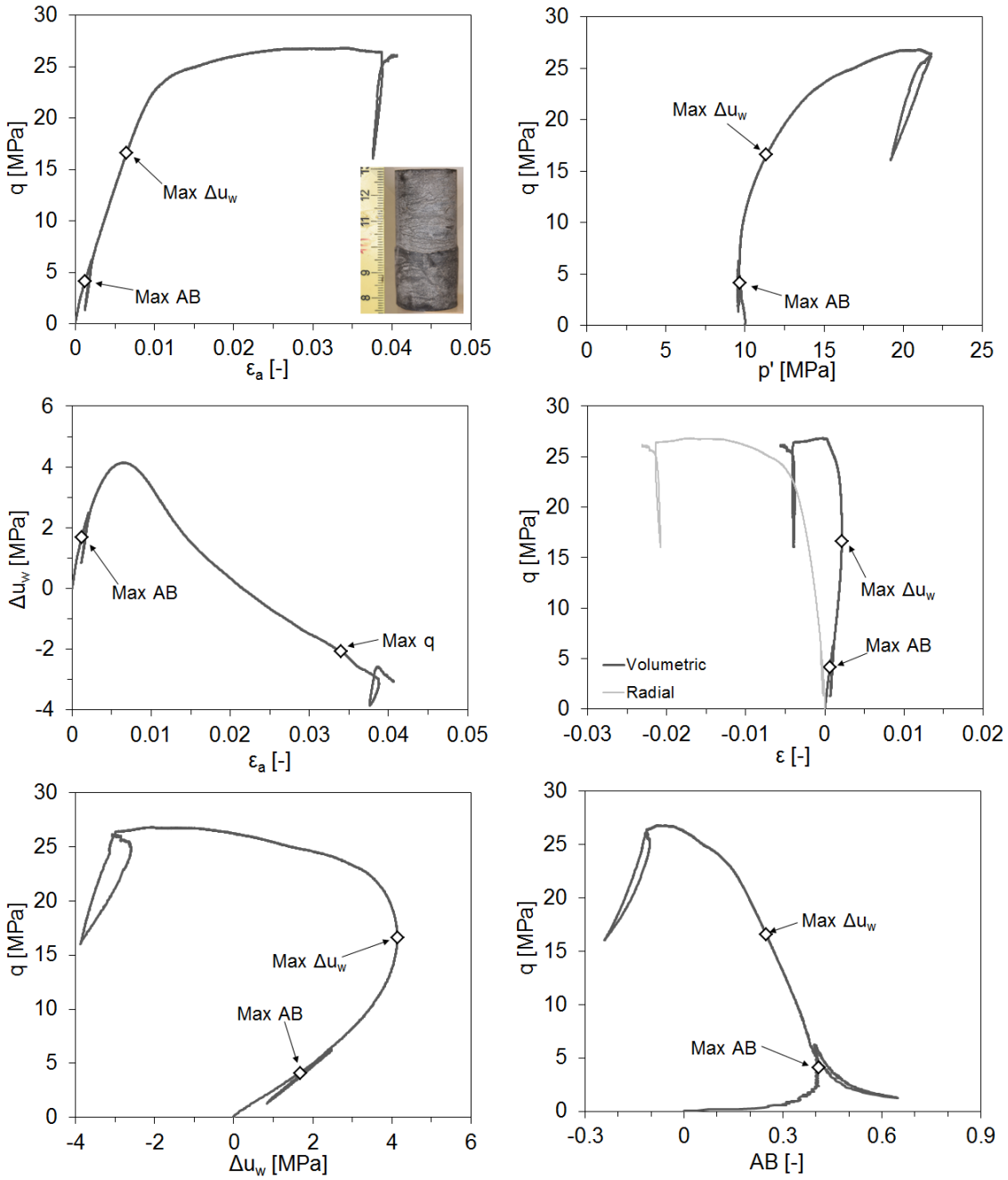

Fig. 27: Results Test 6 Lab A at p'_{in} = 10 MPa

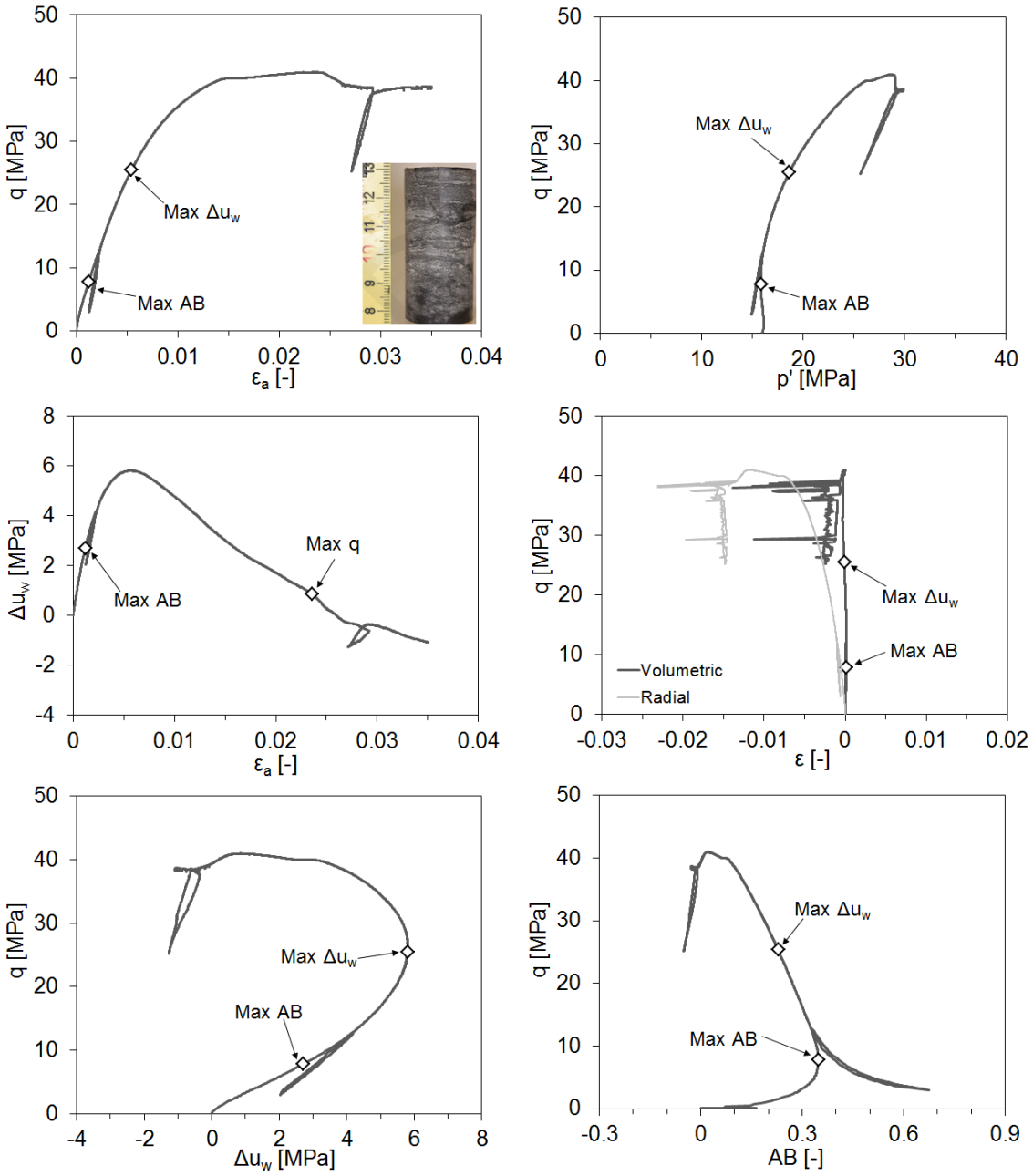

Fig. 28: Results Test 7 Lab A at p'_{in} = 16 MPa

6.2 Lab B tests

Fig. 29 to Fig. 32 show the results of the S- and P-tests performed on the shaly OPA. No particular issues were reported in these tests.

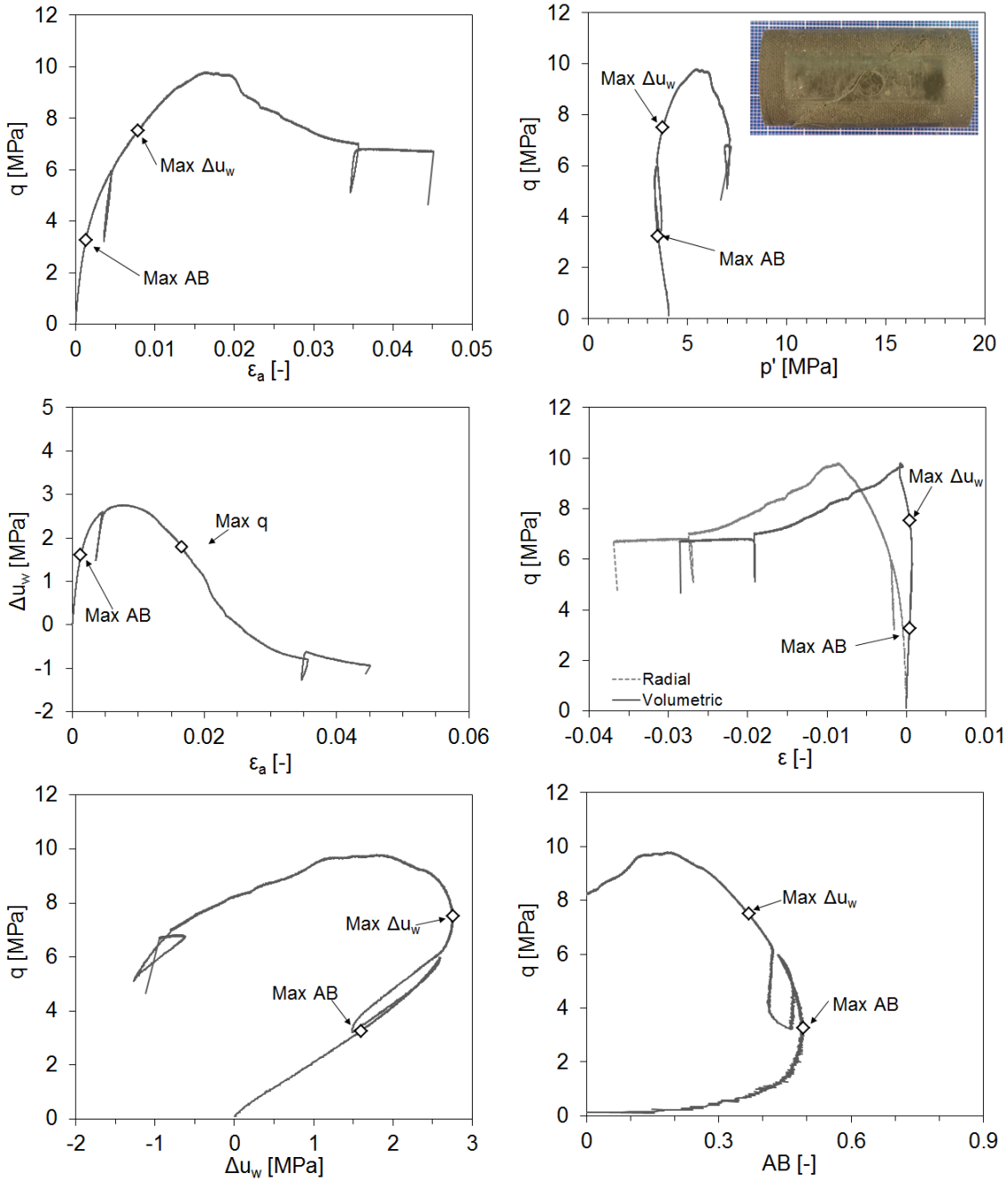

Fig. 29: Results Test 1 Lab B at p'_{in} = 4.0 MPa

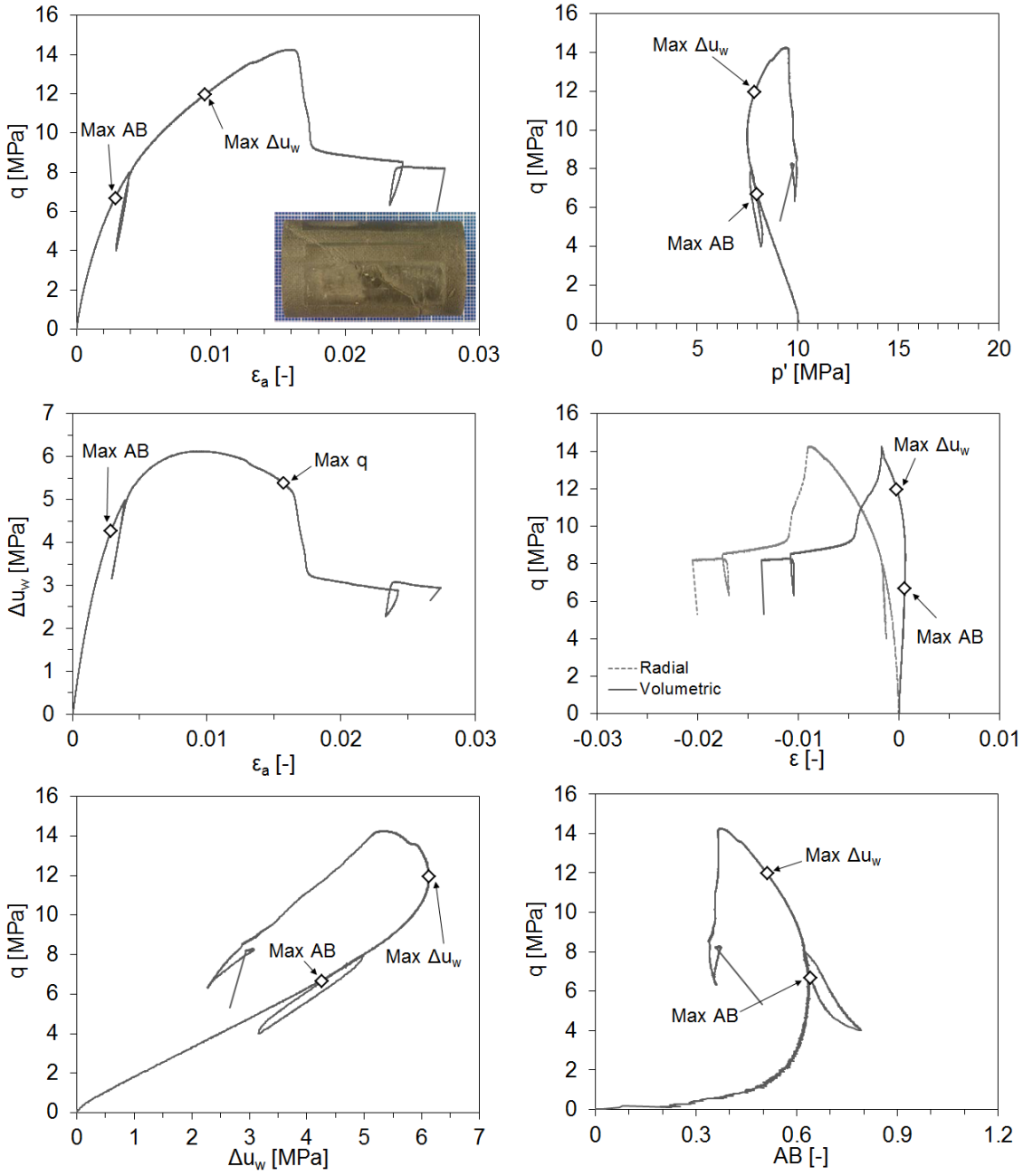

Fig. 30: Results Test 2 Lab B at p'_{in} = 10 MPa

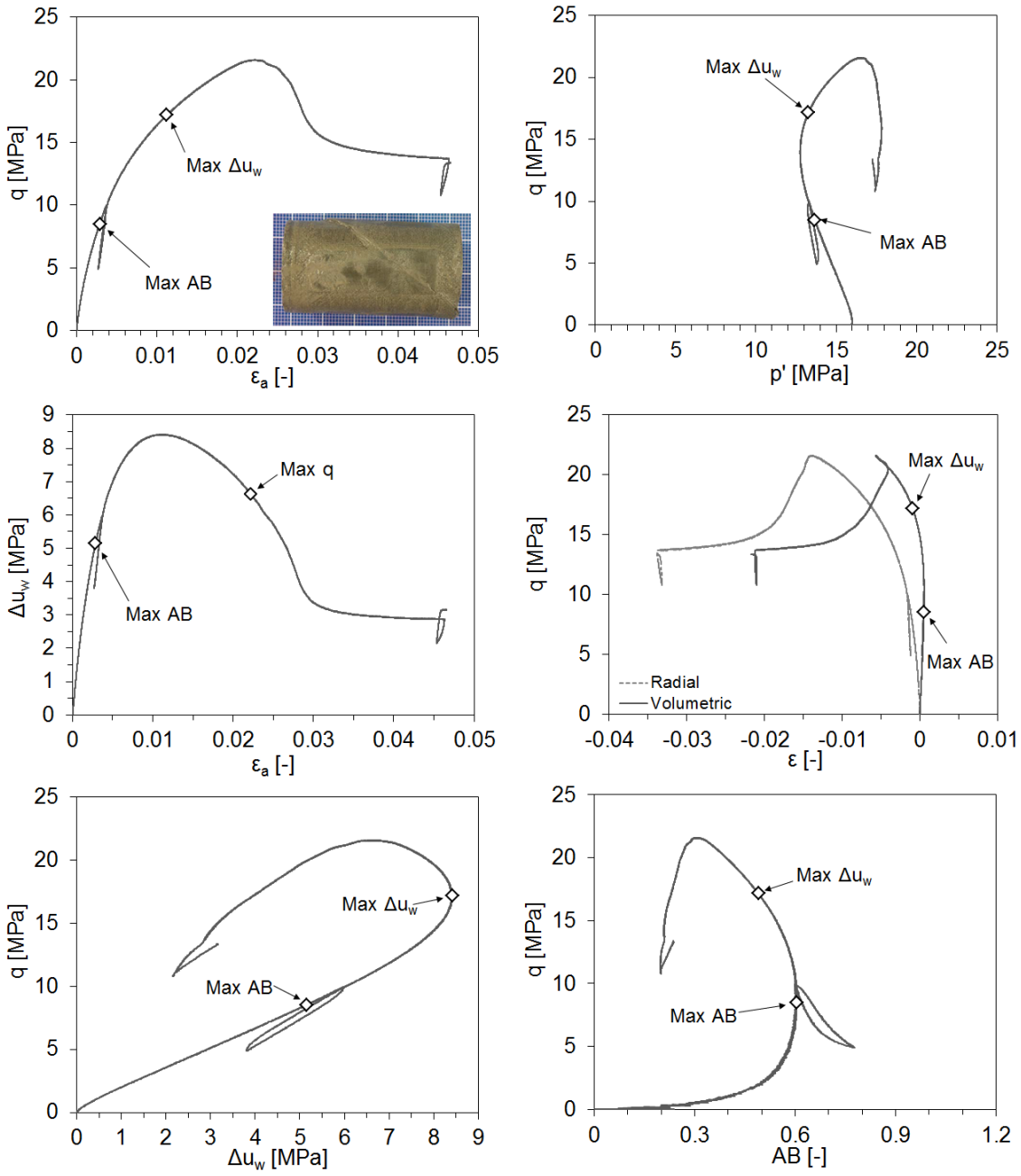

Fig. 31: Results Test 3 Lab B at p'_{in} = 16 MPa

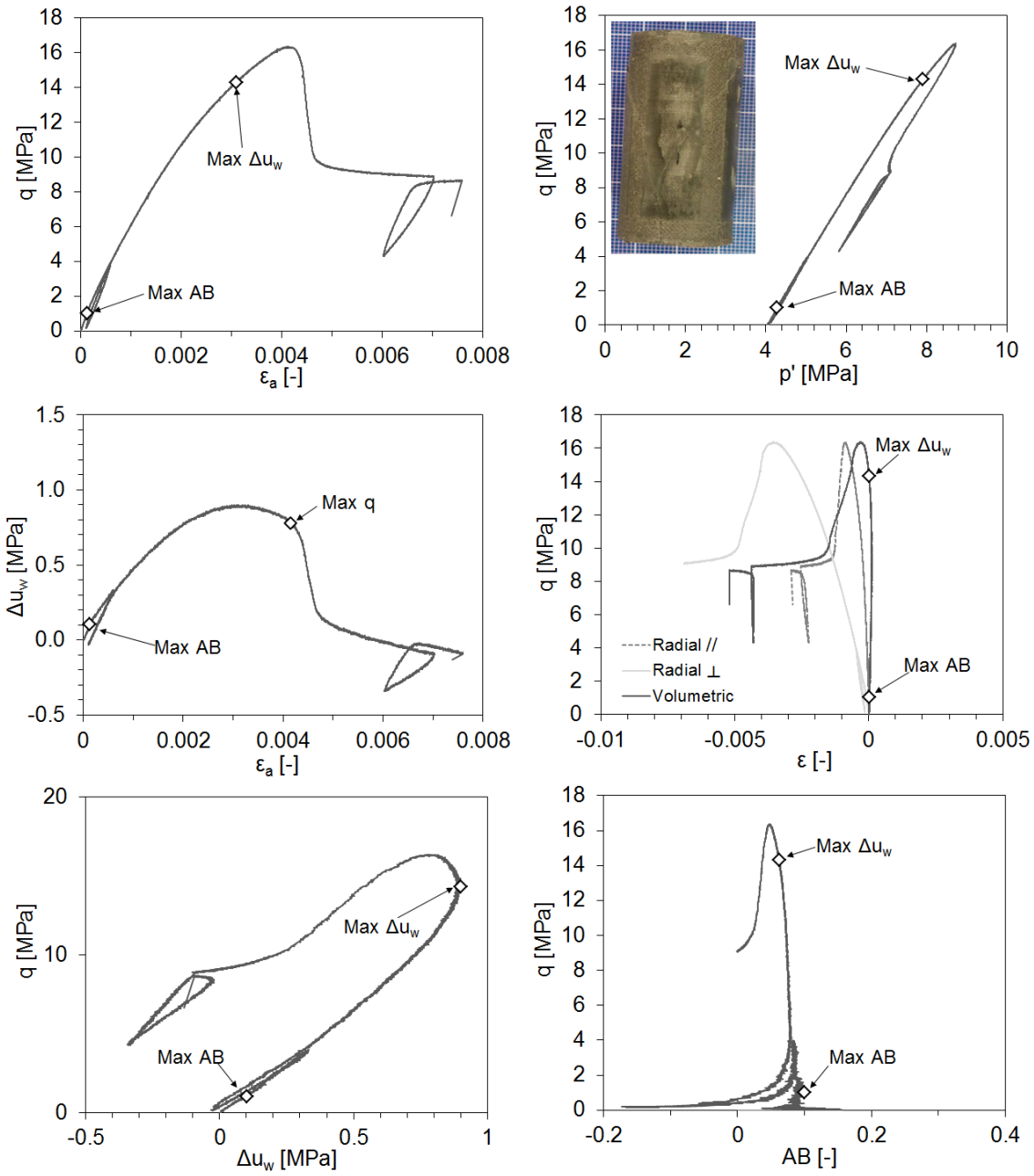

Fig. 32: Results Test 4 Lab B at p'_{in} = 4 MPa

Lab B adopted for the Test 5 (Fig. 33) a reduced triaxial extension (RTE) stress path, where the radial stress was kept constant and the axial stress was progressively decreased. Due to an error in the performance of the experiment related to the load cell, a deviatoric stress was already present at the beginning of the shear phase. This aspect explains why the curves in Fig. 33 do not start from 0 MPa of deviatoric stress.

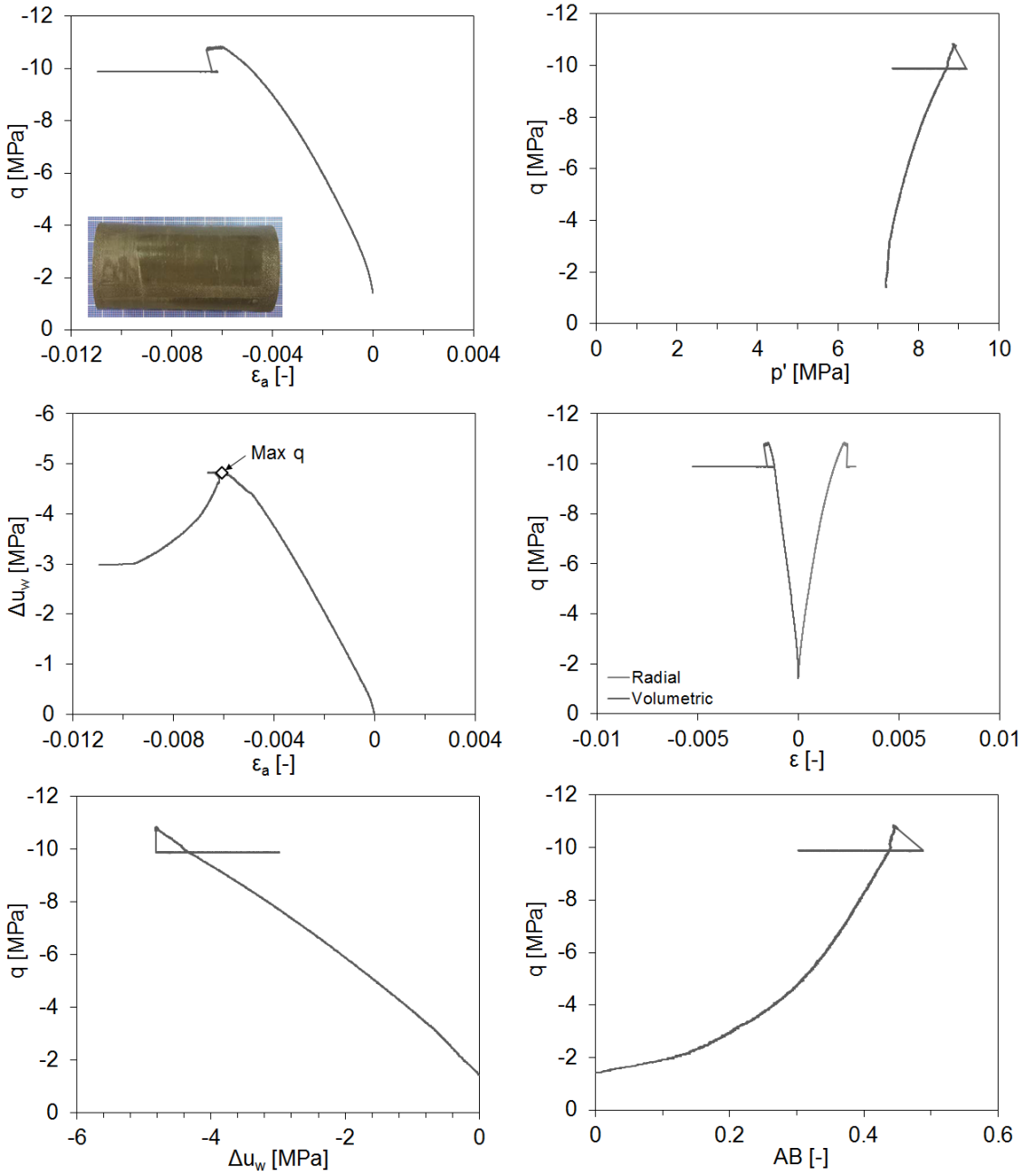

Fig. 33: Results of the RTE test Lab B (Test 5) at p'_{in} = 7.2 MPa

The pore fluid pressure variation is negative (with respect to the 5 MPa at the beginning of the shearing) in this case due to the reduction of the axial stress (Fig. 33). However, the extension leads to a pressure decreased to 0 MPa before the achievement of the specimen's failure. To avoid the generation of negative pore water pressure, the test was concluded by keeping the axial and radial stresses constant and increasing the pore water pressure until the failure of the specimen. However, the picture of the specimen after testing did not show a clear failure plane.

Fig. 34 and Fig. 35 show the results of the Tests 6 and 7 performed on the sandy OPA. Beside the higher strength compared to the shaly facies, a significant reduction of the pore fluid pressure after maximum is observed. In the Test 7 the pressure decreased to 0 MPa (-5 MPa in the Fig. 35) in correspondence of the peak stress; hence, pore fluid pressure in the specimen was not controlled and suction might have developed during the entire post-peak phase. Moreover, the picture of the specimen after the test does not show the development of a clear failure surface.

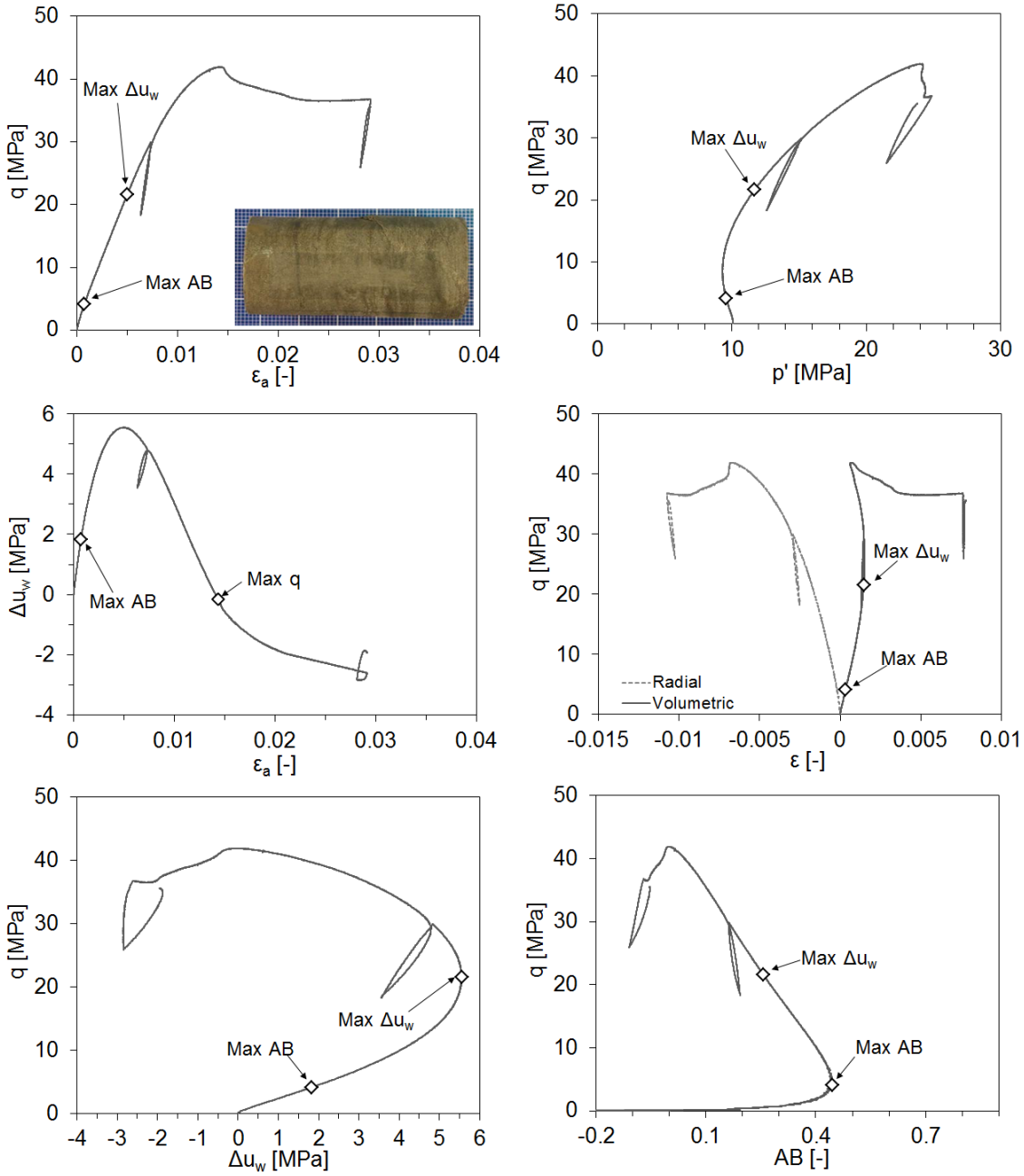

Fig. 34: Results Test 6 Lab B at p'_{in} = 10 MPa

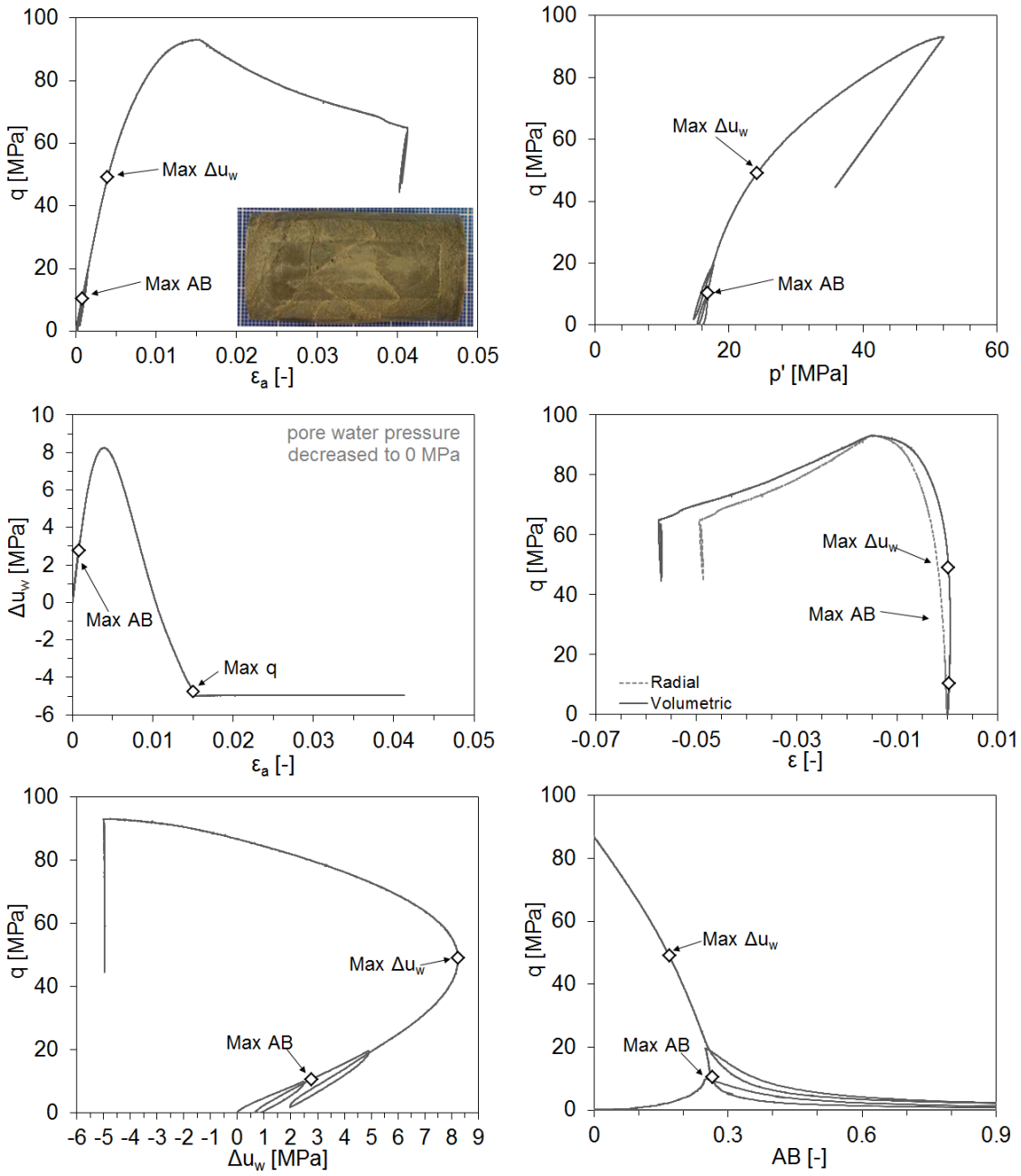

Fig. 35: Results Test 7 by Lab B at p'_{in} = 16 MPa

6.3 Lab C tests

The achievement of the target effective confining stress before the shearing phase was challenging in the case of Lab C due to the adopted alternative testing procedure that did not allow the direct control of the pore fluid pressure. For this reason, the initial mean effective stresses were slightly different than the planned values in the following figures.

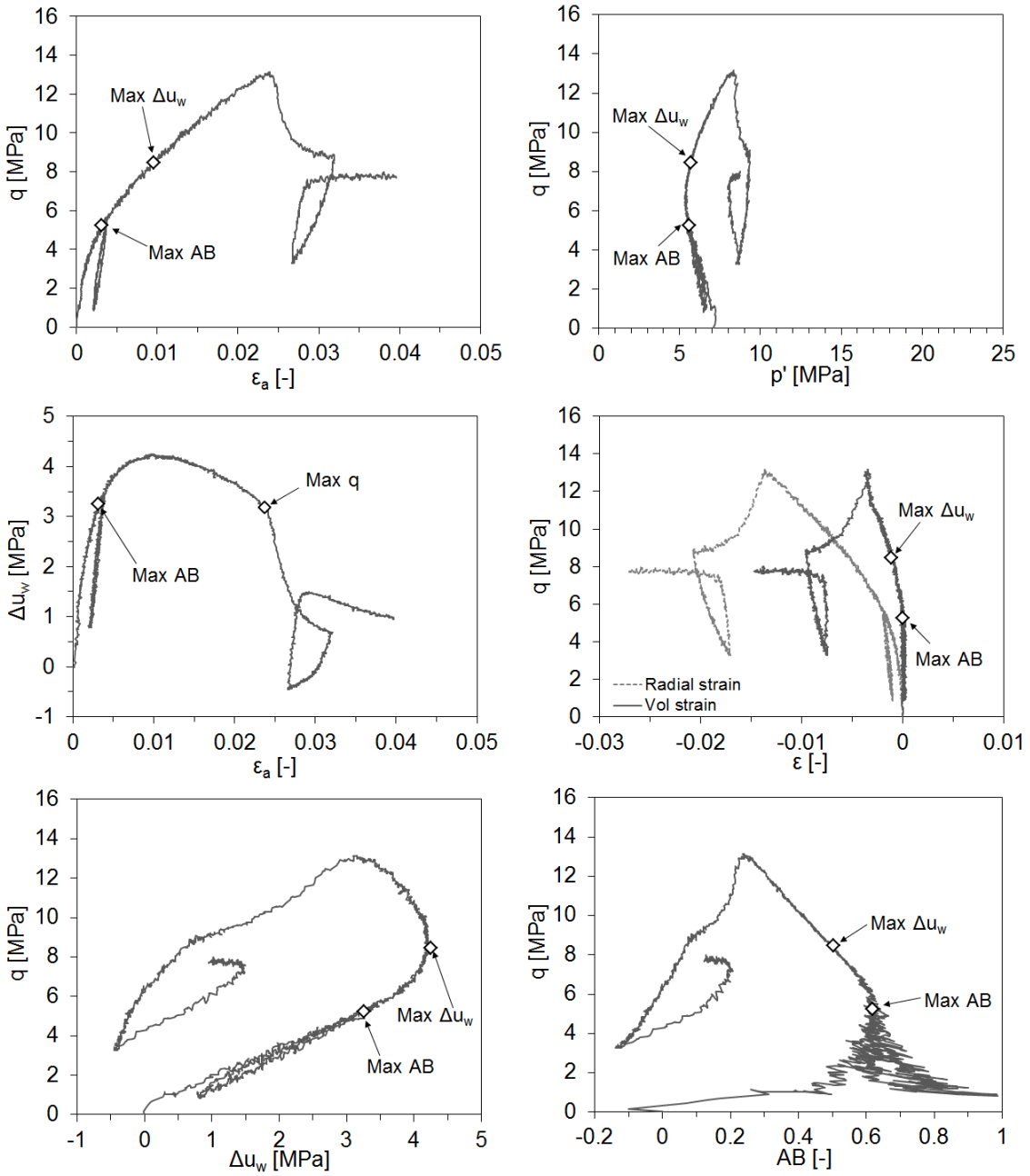

Fig. 36: Results Test 2 (BGC2-1-2) Lab C at p'_{in} = 7.5 MPa

Fig. 37 shows the results of the Test 2 (BGC2-1-4) that was performed with a strain rate of 2×10^{-6} s^{-1}. Two pressure transducers were used to evaluate the fluid pressure evolution during shearing at the top and bottom of the specimen. However, only the bottom pressure transducer is connected to the side screen, while the top transducer is just measuring the pressure at top centre of the specimen. The results are also compared with the Test 2 (BGC2-1-2, Fig. 36). A slightly different fluid pressure evolution between top and bottom side is observed, with a slower fluid pressure increase at the top. The consequent effect on the stress path is highlighted. On the other hand, the consistence between the two tests when the bottom fluid pressure is considered for the test BGC2-1-4 is clearly highlighted. Moreover, the absence of unloading-reloading cycle in the test BGC2-1-4 allowed for a better evaluation of the maximum AB parameter.

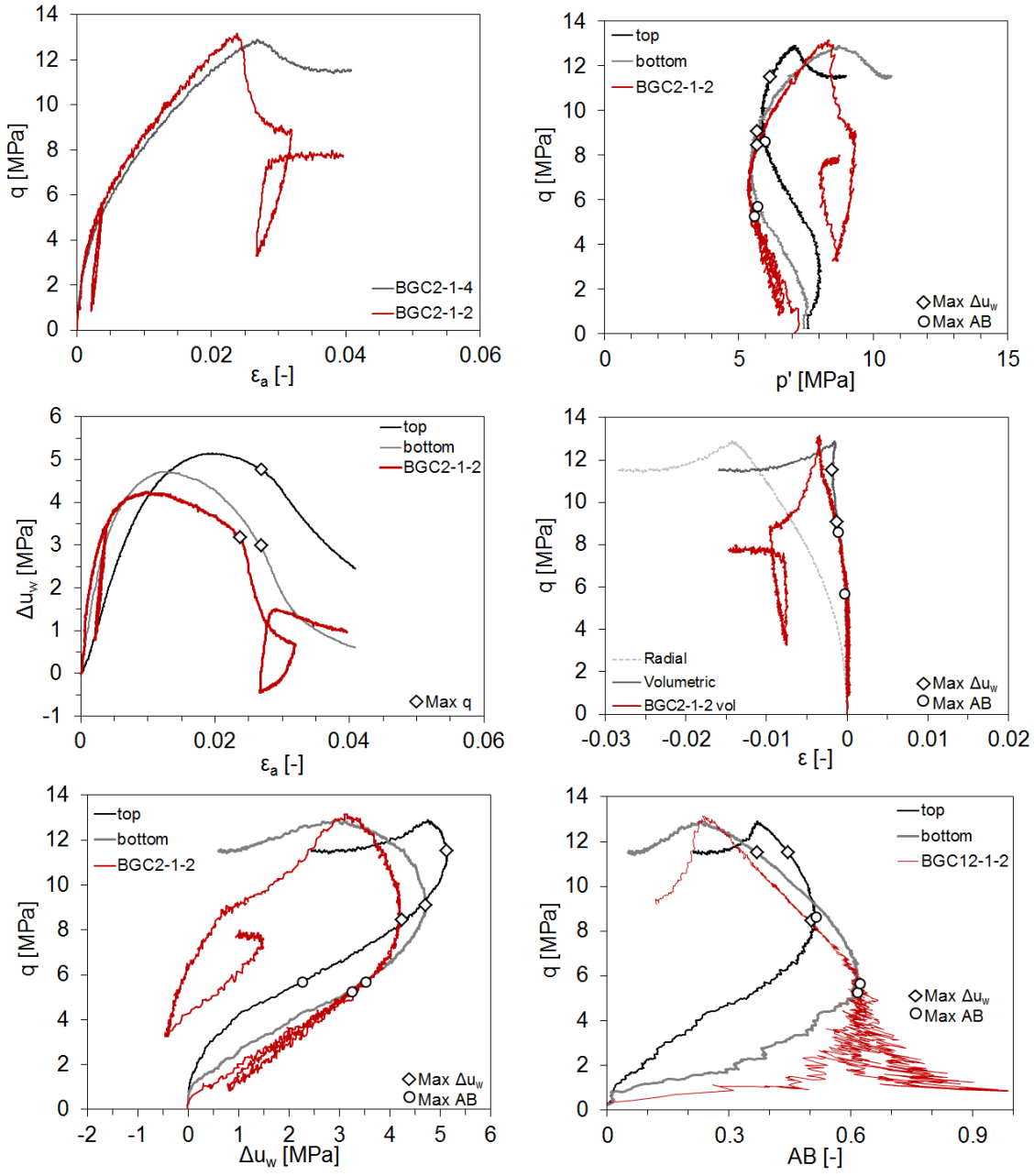

Fig. 37: Results Test 2 (BGC2-1-4) Lab C at p'_{in} = 7.5 MPa

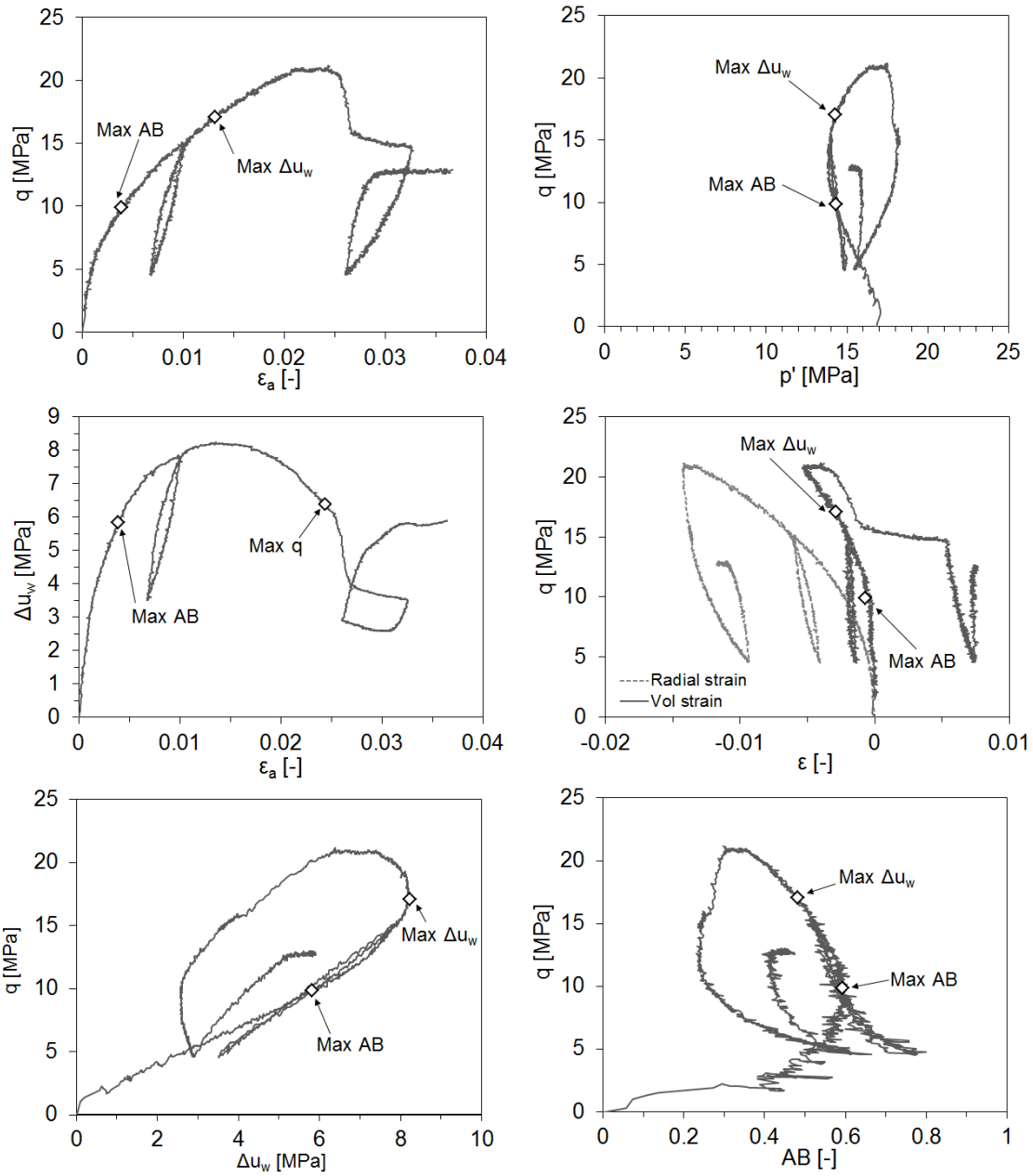

Fig. 38: Results Test 3 Lab C at p'_{in} = 16.8 MPa

Two P tests were performed by Lab C, in the following named as Test 4 BGC2-1-11 at p'_{in} = 9 MPa and Test 4 BGC2-1-13 at p'_{in} = 16.5 MPa. In the test BGC2-1-13 no unloading/ reloading cycles were performed before and after the failure of the specimen.

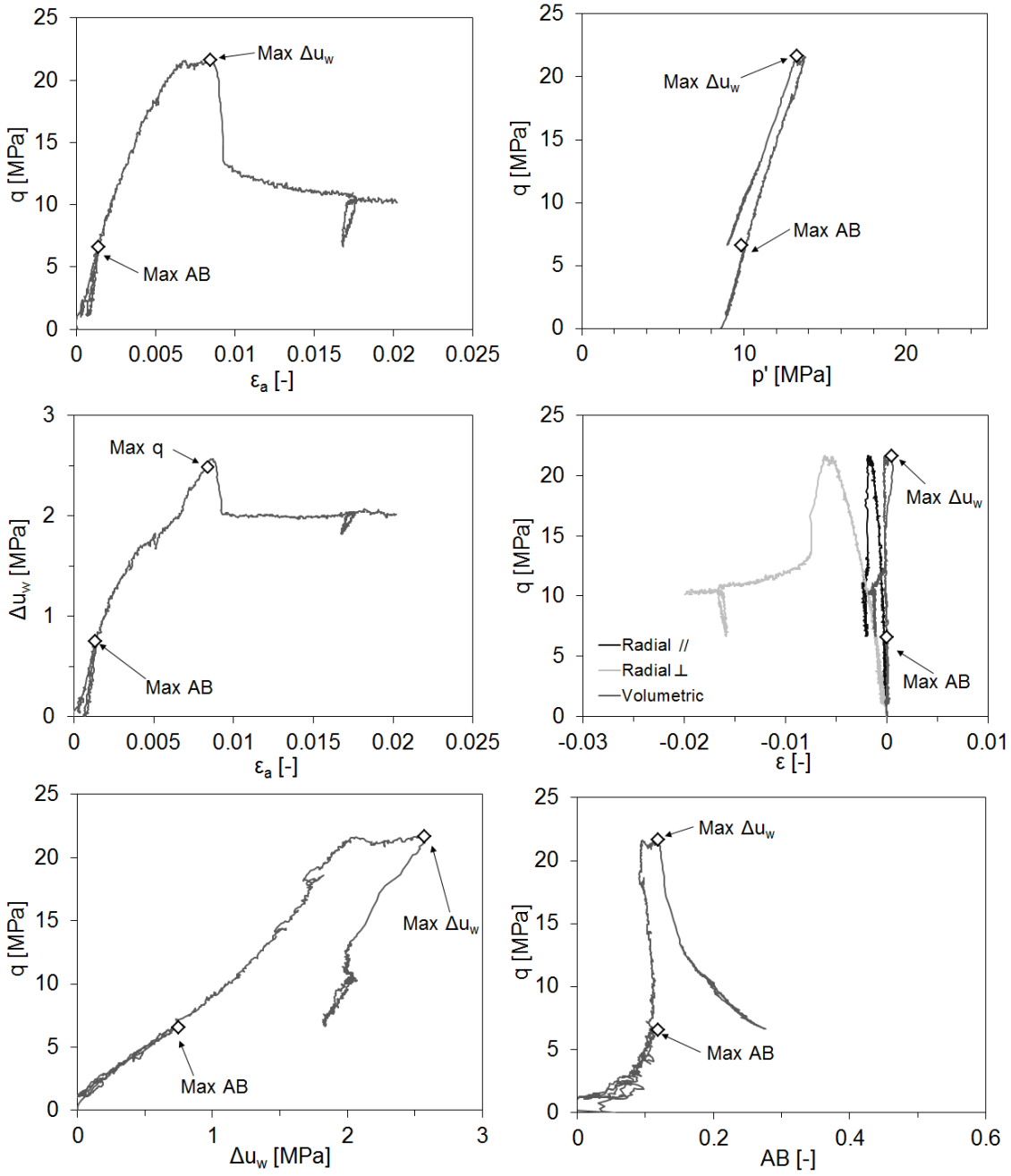

Fig. 39: Results Test 4 (BGC2-1-11) Lab C at p'_{in} = 9 MPa

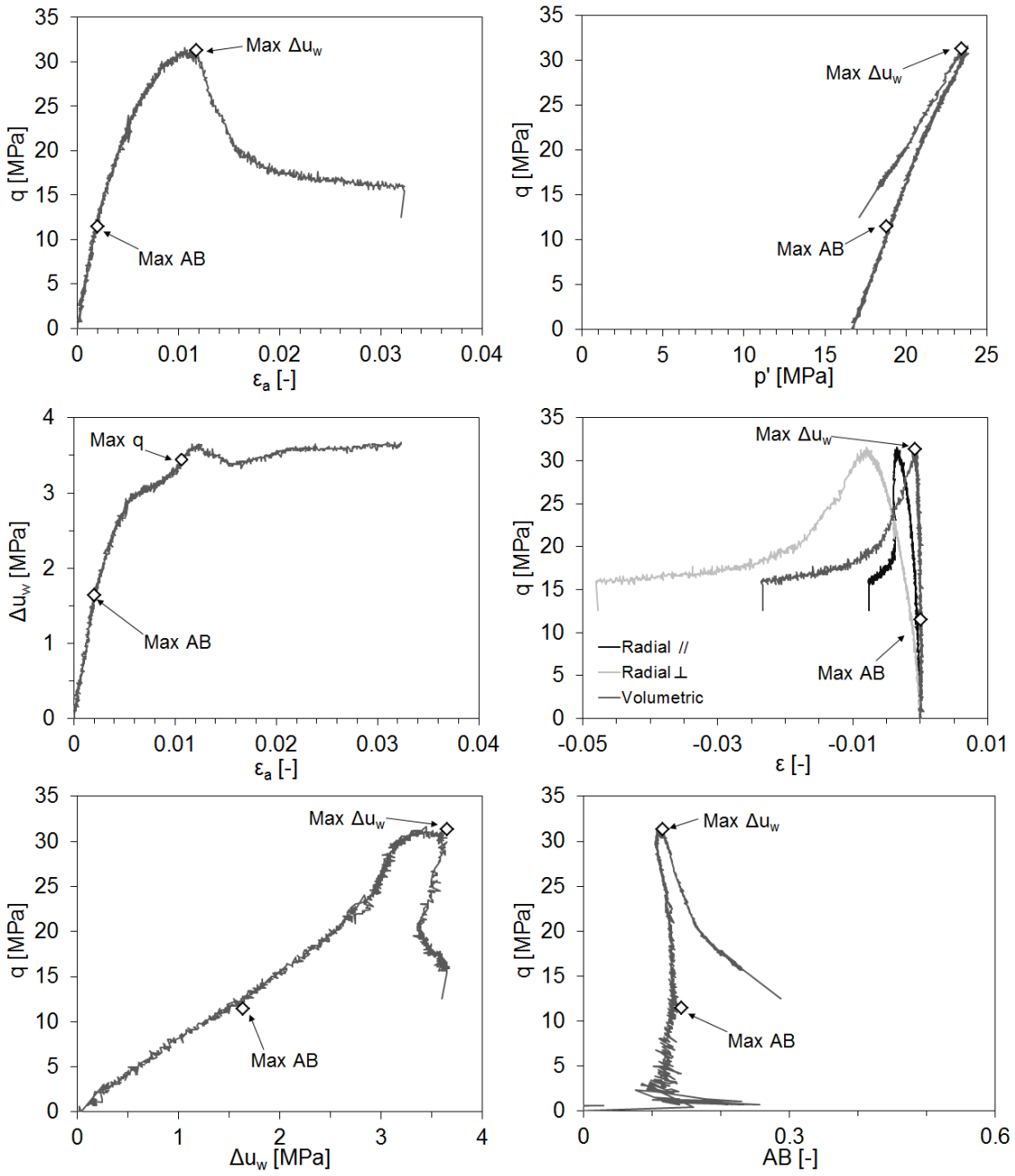

Fig. 40: Results Test 4 (BGC2-1-13) Lab C at p'_{in} = 16.5 MPa

For the Test 5, Lab C adopted a Triaxial Compression (TC) stress path, where axial stress was increased and radial stress was decreased to keep the mean total stress constant during shearing.

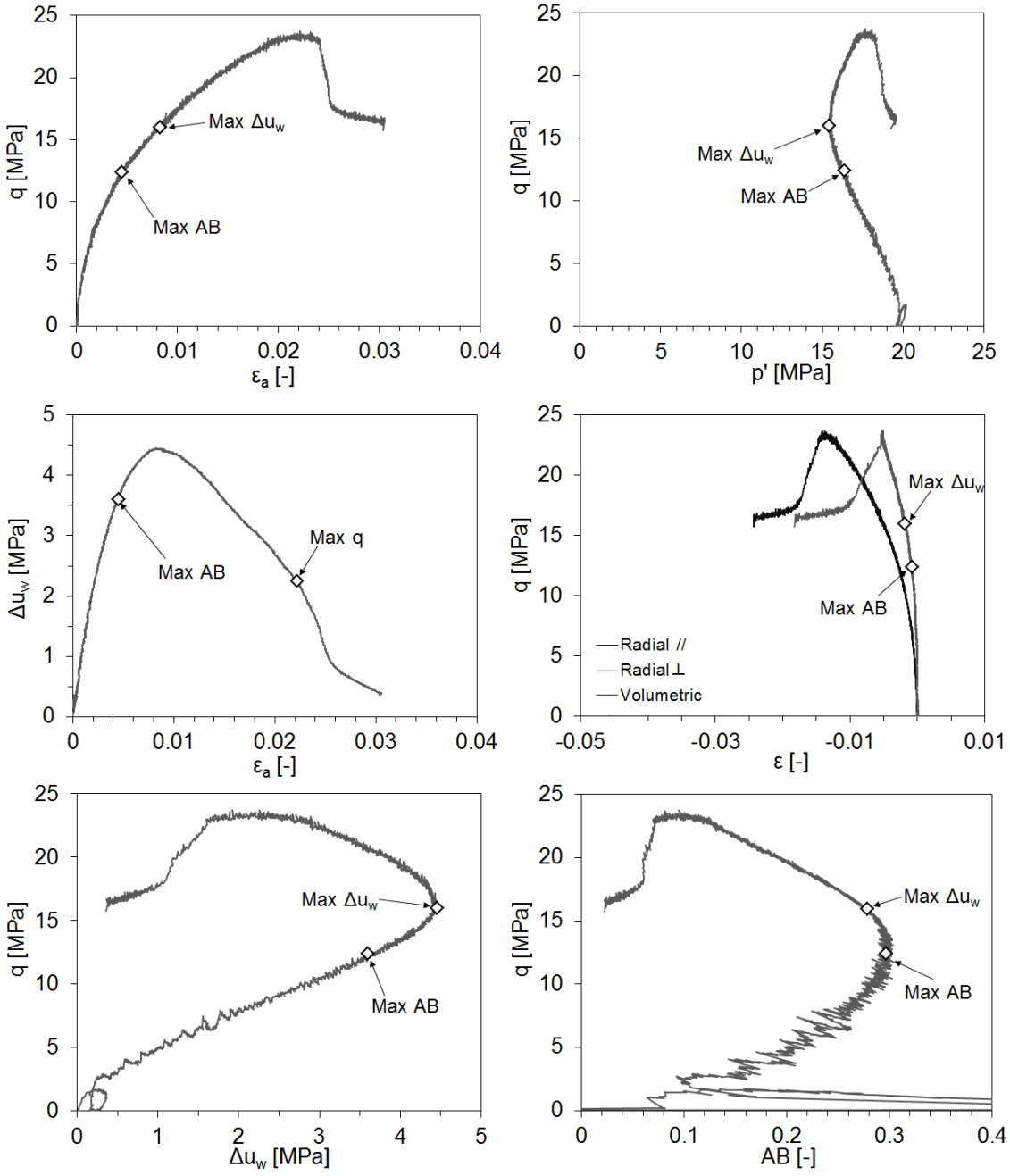

Fig. 41: Results of the triaxial compression (TC) test Lab C (Test 5) at p'_{in} = 20 MPa

Lab C is the only contractor that performed also Z tests (bedding orientation oblique to the axial loading). Three tests were carried out at three different effective confining stresses. The preparation of the specimens for Z-tests was a challenging aspect due to the orientation of the bedding. To avoid disturbance during shearing, in the Test 10 and Test 11 unloading/reloading cycles were not performed. The unloading-reloading cycle was only carried out in the Test 12 (Fig. 44).

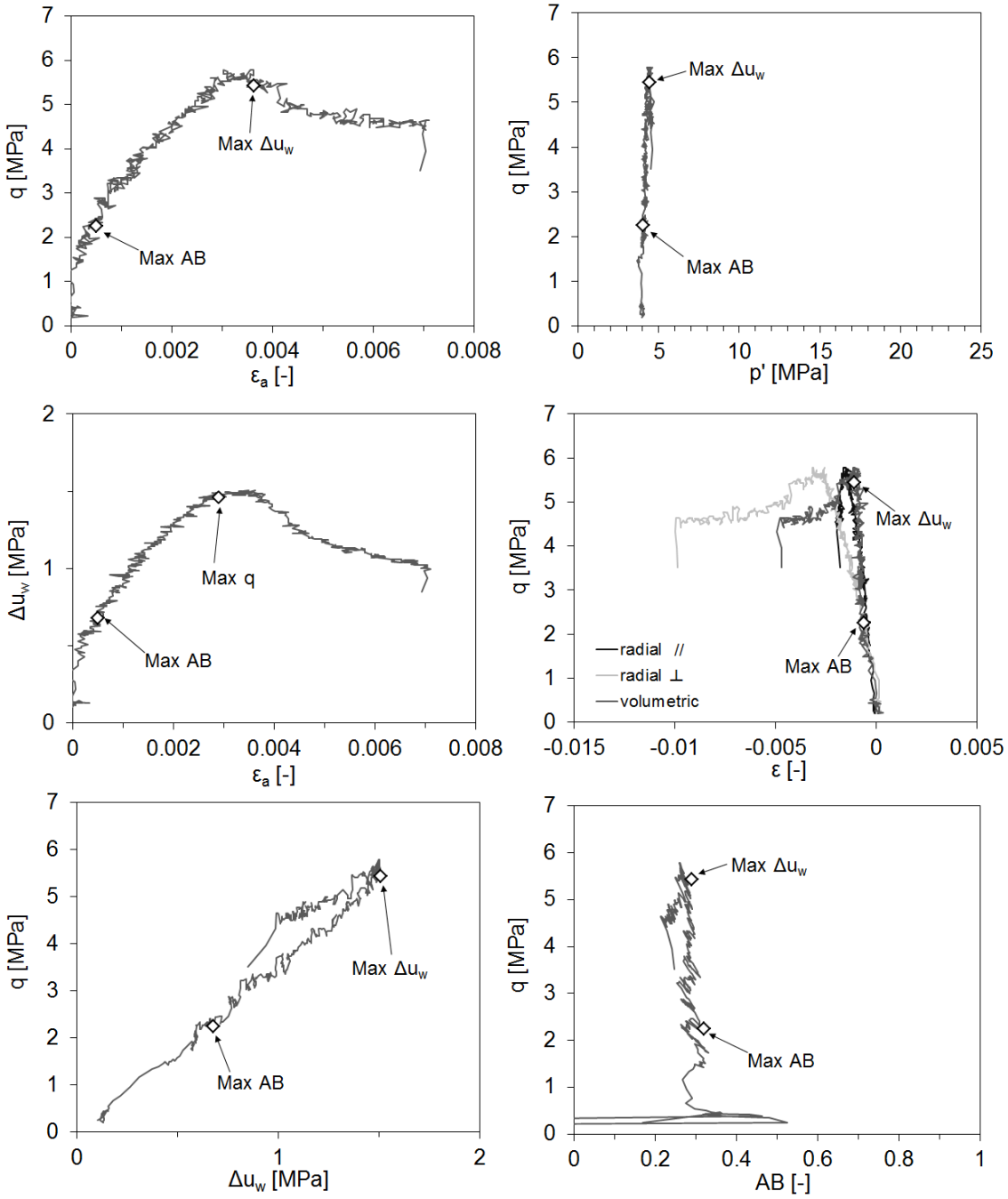

Fig. 42: Results Test 10 Lab C at p'_{in} = 4 MPa

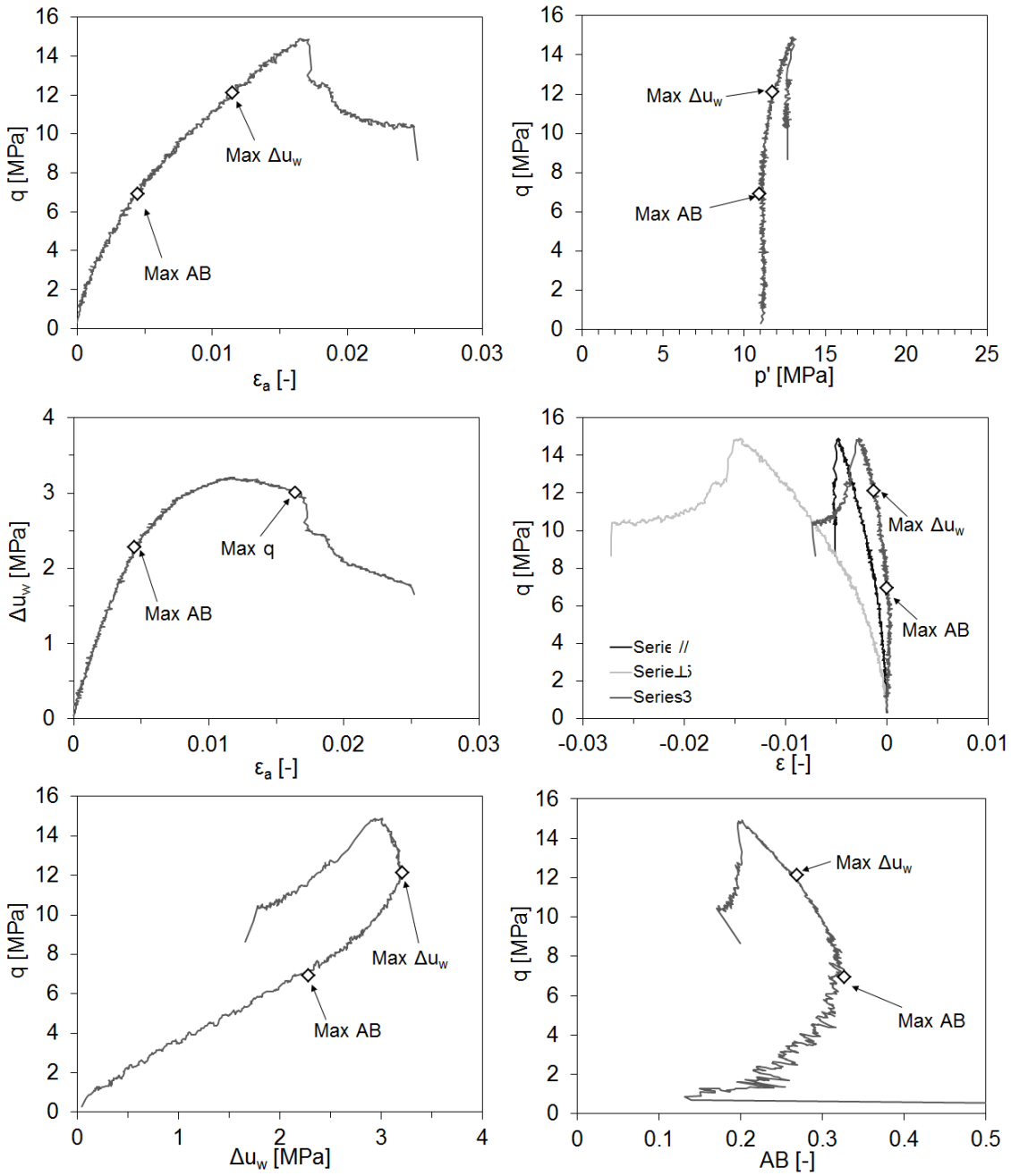

Fig. 43: Results Test 11 Lab C at p'_{in} = 11 MPa

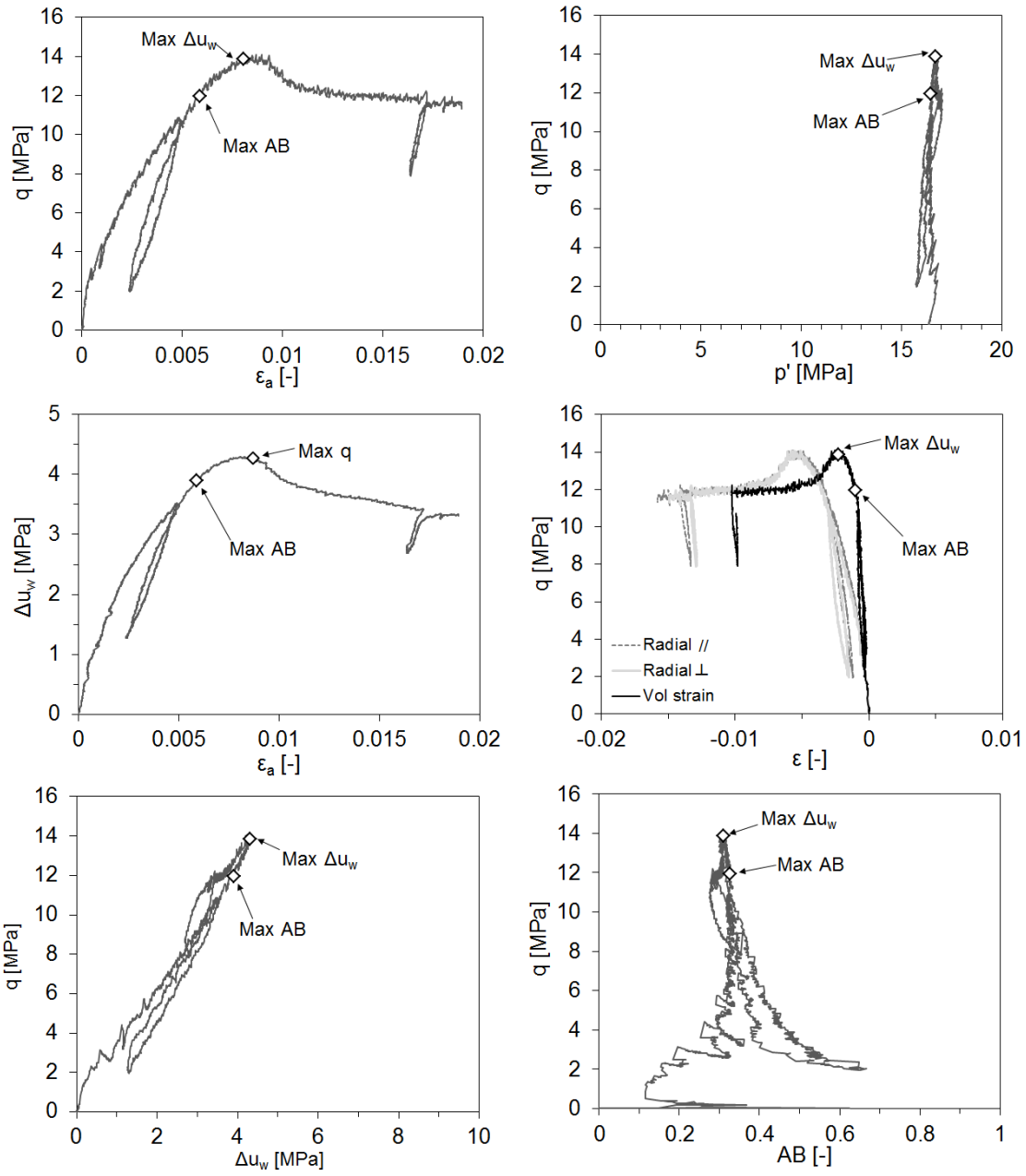

Fig. 44: Results Test 12 Lab C at p'_{in} = 16.4 MPa

6.4 Lab D tests

Lab D carried out tests just on the sandy OPA. Only the Test 8 (BGC2-17-4) in Fig. 46 showed a clear brittle failure of the specimen. The Test 8 (BGC2-17-1) in Fig. 47 was stopped before the achievement of the specimen's failure because of the decrease of the pore fluid pressure to almost zero (this aspect is also observed in the Test 7 by Lab B in Fig. 35); the post-peak conditions could not be defined, while the maximum achieved deviatoric stress is considered as peak strength. The Test 6 (Fig. 45) exhibited an initial ductile response followed by a further increase of the deviatoric stress; for this test, the post-peak conditions could be defined. The fractures of the specimens in the Test 6 and Test 8 (BGC2-17-1) are due to the extraction of the specimens from the apparatus after testing.

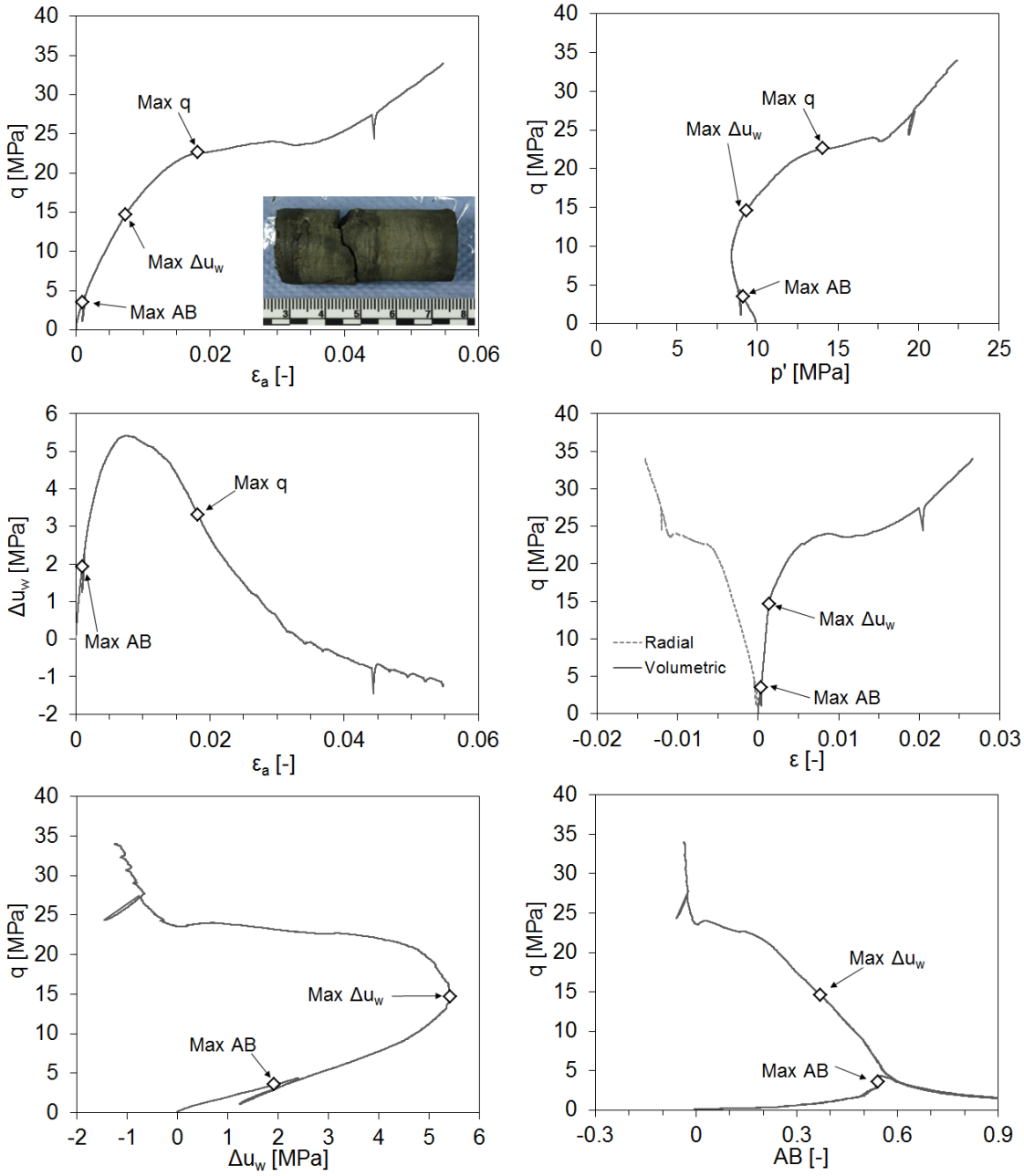

Fig. 45: Results Test 6 Lab D at p'_{in} = 10 MPa

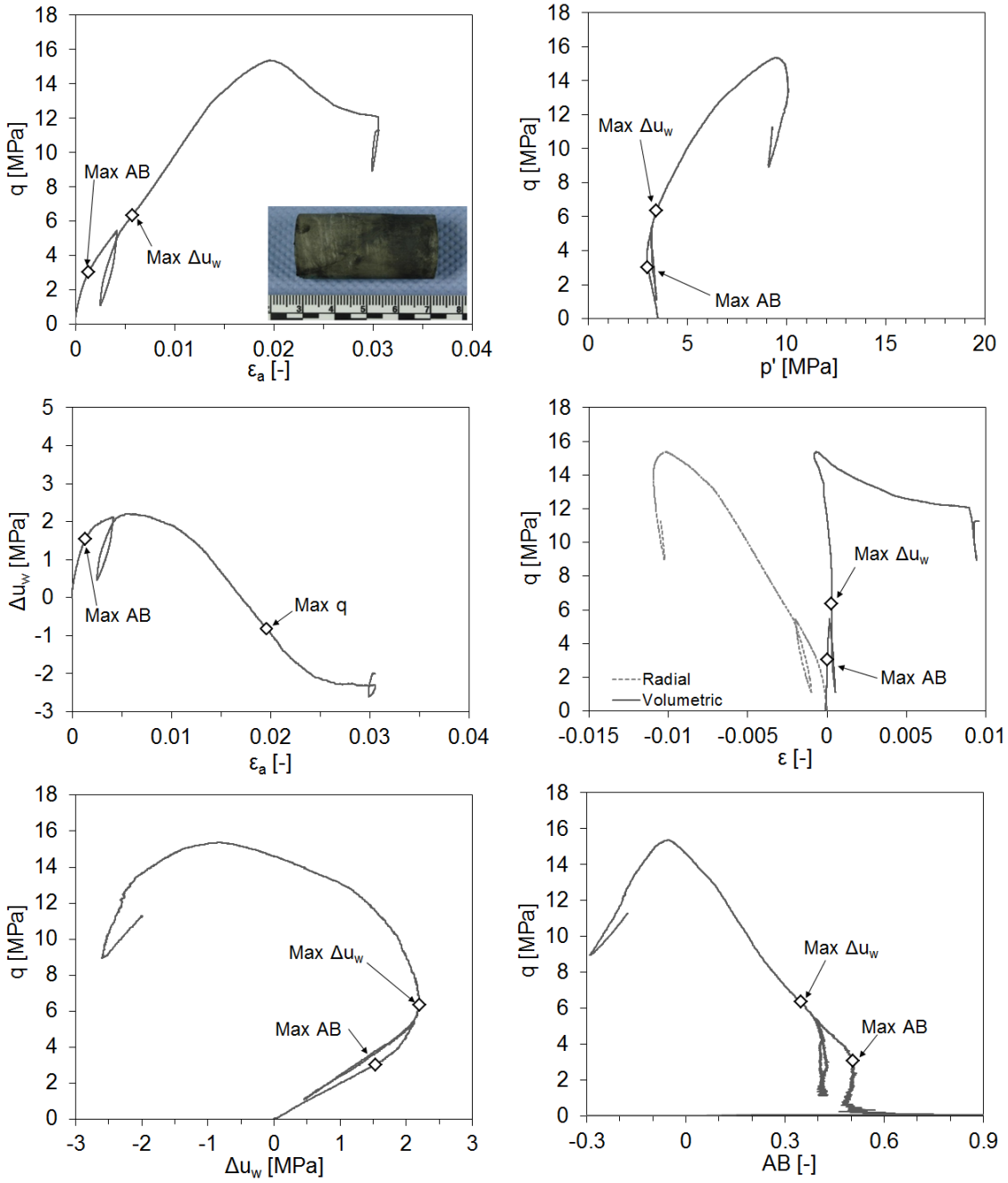

Fig. 46: Results Test 8 (BGC2-17-4) Lab D at p'_{in} = 3.6 MPa

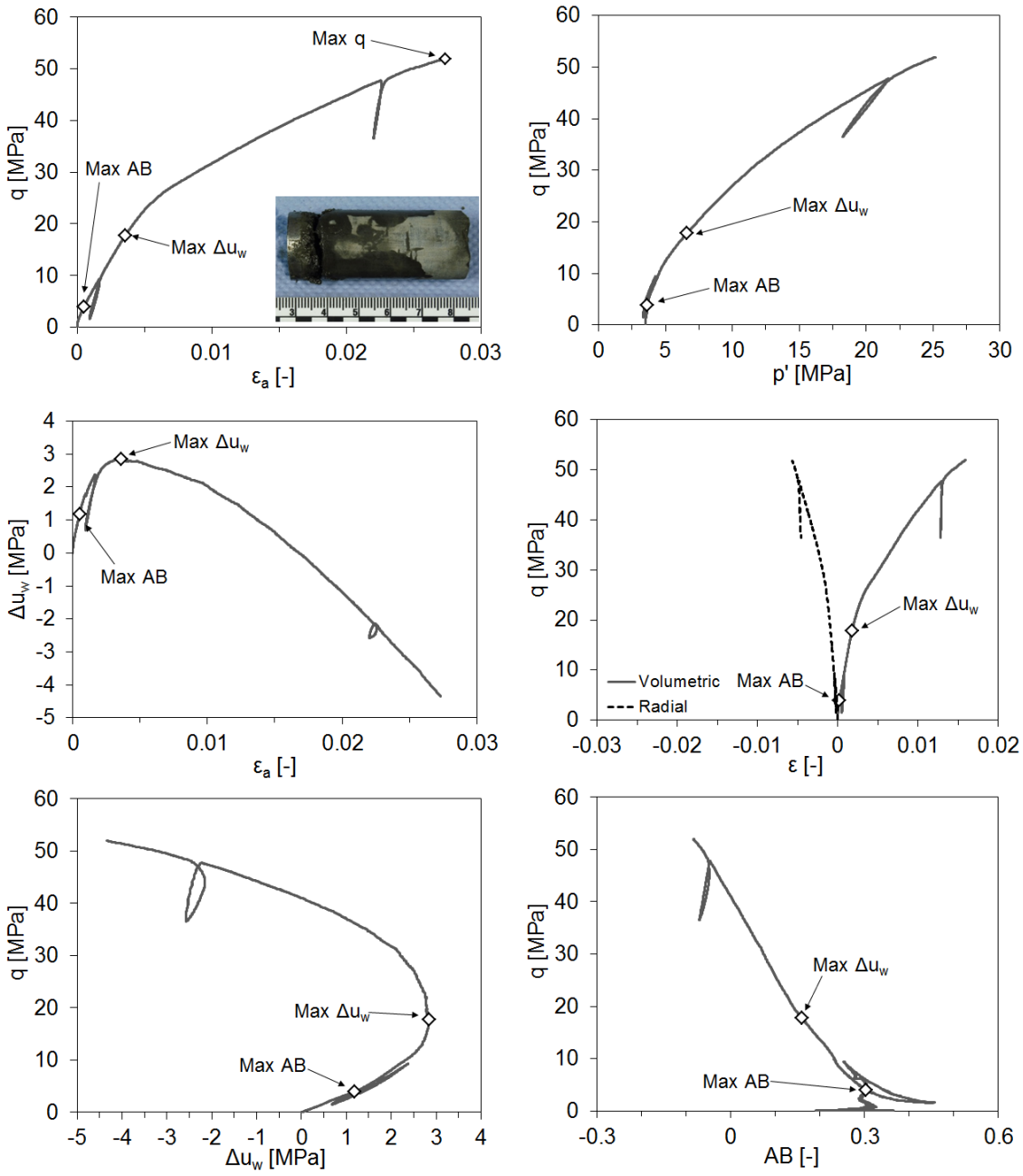

Fig. 47: Results Test 8 (BGC2-17-1) Lab D at p'_{in} = 3.5 MPa

6.5 Lab E tests

Lab E performed tests also exclusively with cores from the sandy OPA. As reported in the previous sections, Lab E had issues with the measurement of the radial strain. The radial strain presented in the Test 6 and Test 7 (Fig. 48 to Fig. 51) was back calculated from the volume variations of the pump used to control the confining pressure. In Test 8 (Fig. 52) this correction seemed not to be applied as no radial deformation was recorded during shearing. As a consequence of this issue, the volumetric strain cannot be considered as reliable.

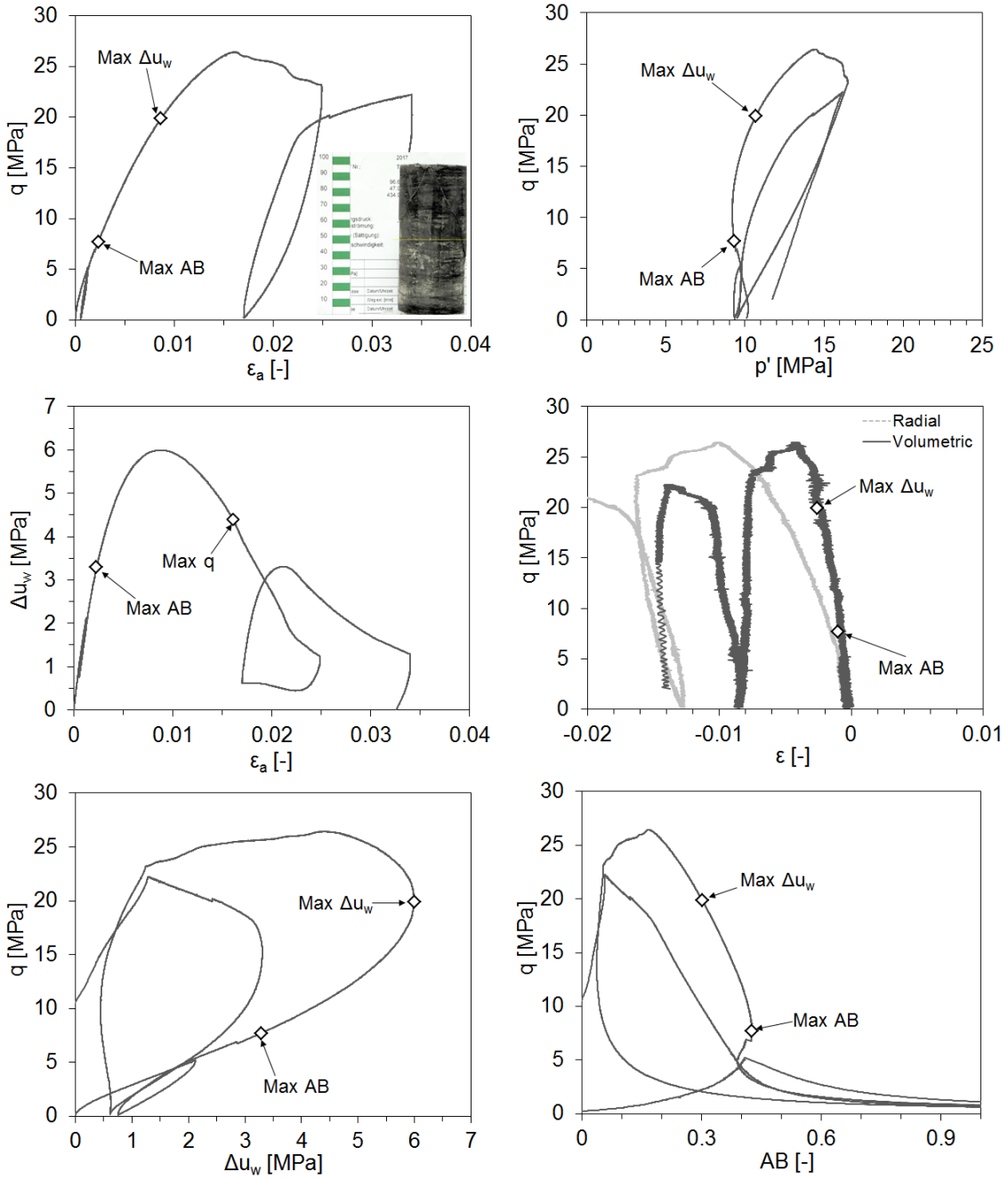

Fig. 48: Results Test 6 Lab E at p'_{in} = 10 MPa

Fig. 49, Fig. 50, and Fig. 51 show the results of the multistage Test 7 performed by Lab E. Three stages were performed at effective confining stresses of 4, 10, and 16 MPa. The transition between two stages was done by decreasing the deviatoric stress to zero, re-establishing the back pressure to the target value of 5 MPa, and consolidating the specimen to the new effective confining stress.

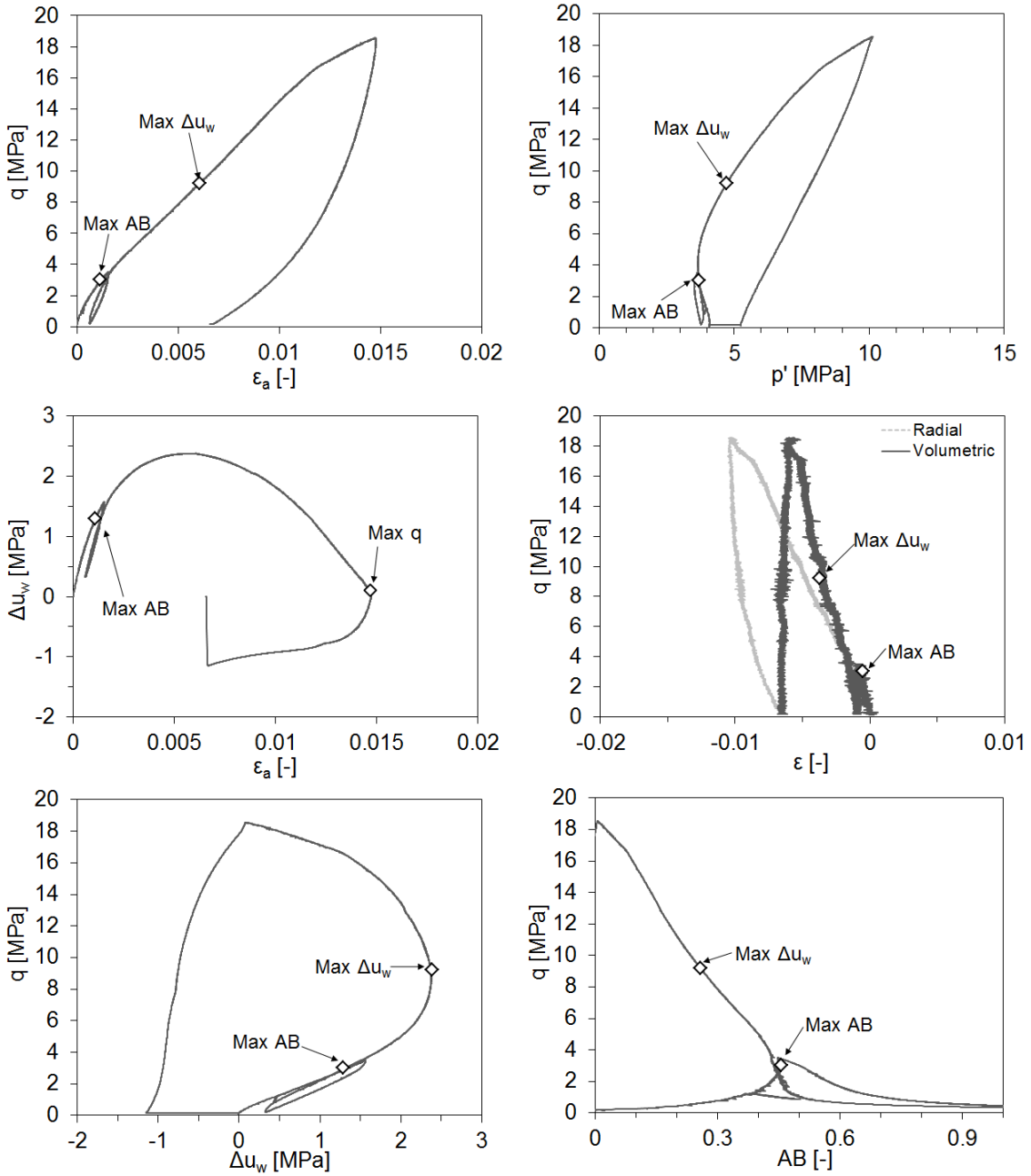

Fig. 49: Results Stage 1 of the multistage Test 7 Lab E at p'_{in} = 4 MPa

At the end of the Stage 2, the back pressure was not allowed to decrease below 5 MPa during the reduction of the deviatoric stress.

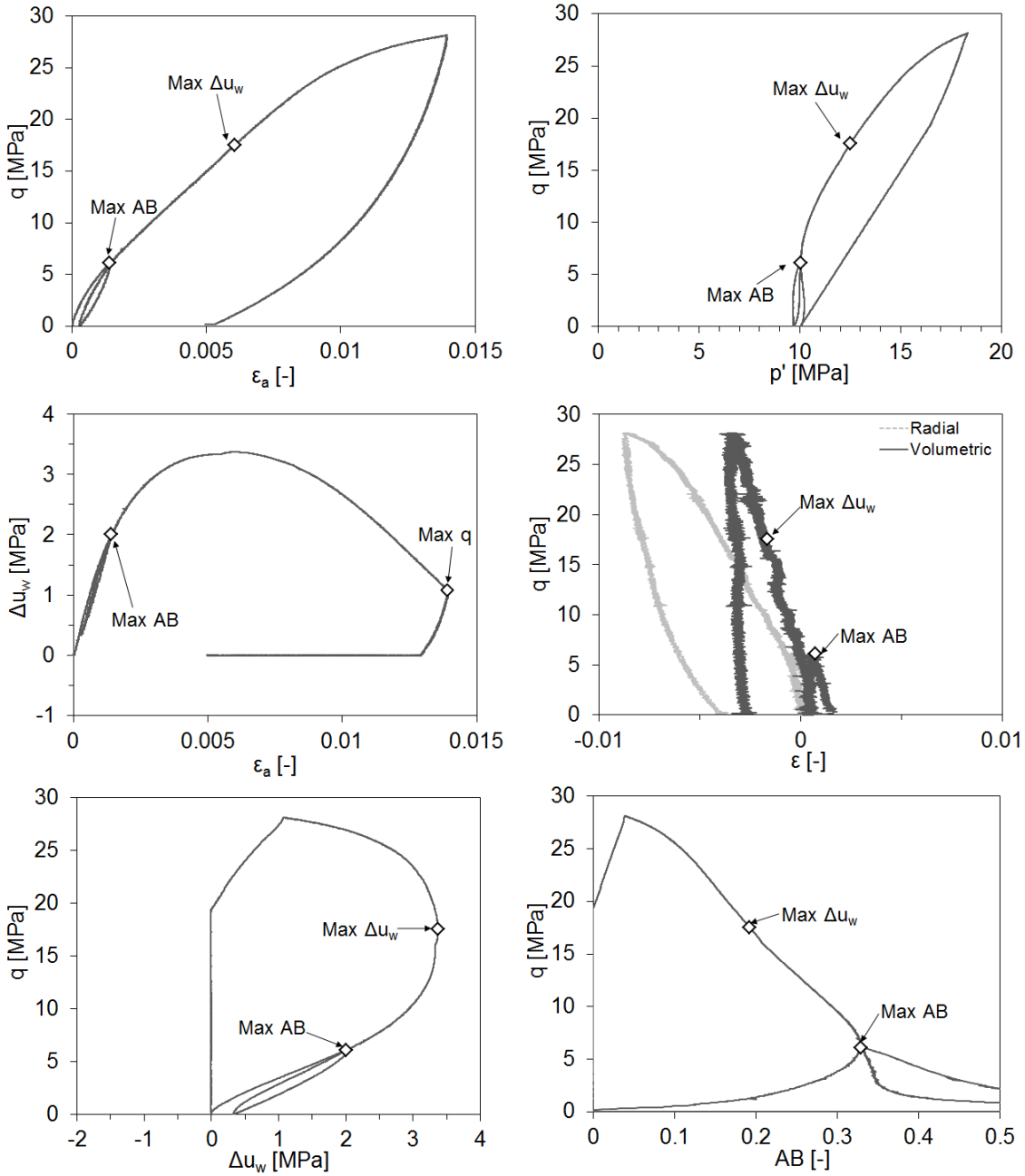

Fig. 50: Results Stage 2 of the multistage Test 7 Lab E at p'_{in} = 10 MPa

In the Stage 3 of the multistage Test 7 (Fig. 51), the specimen did not exhibit a brittle failure. The response might be due to a damage of the specimen after the Stage 2, when a complete unloading of the specimen was performed to solve a technical issue with the apparatus. The picture of the specimen after testing does not show a clear oblique failure plane as observed also in other sandy specimens tested by other contractors.

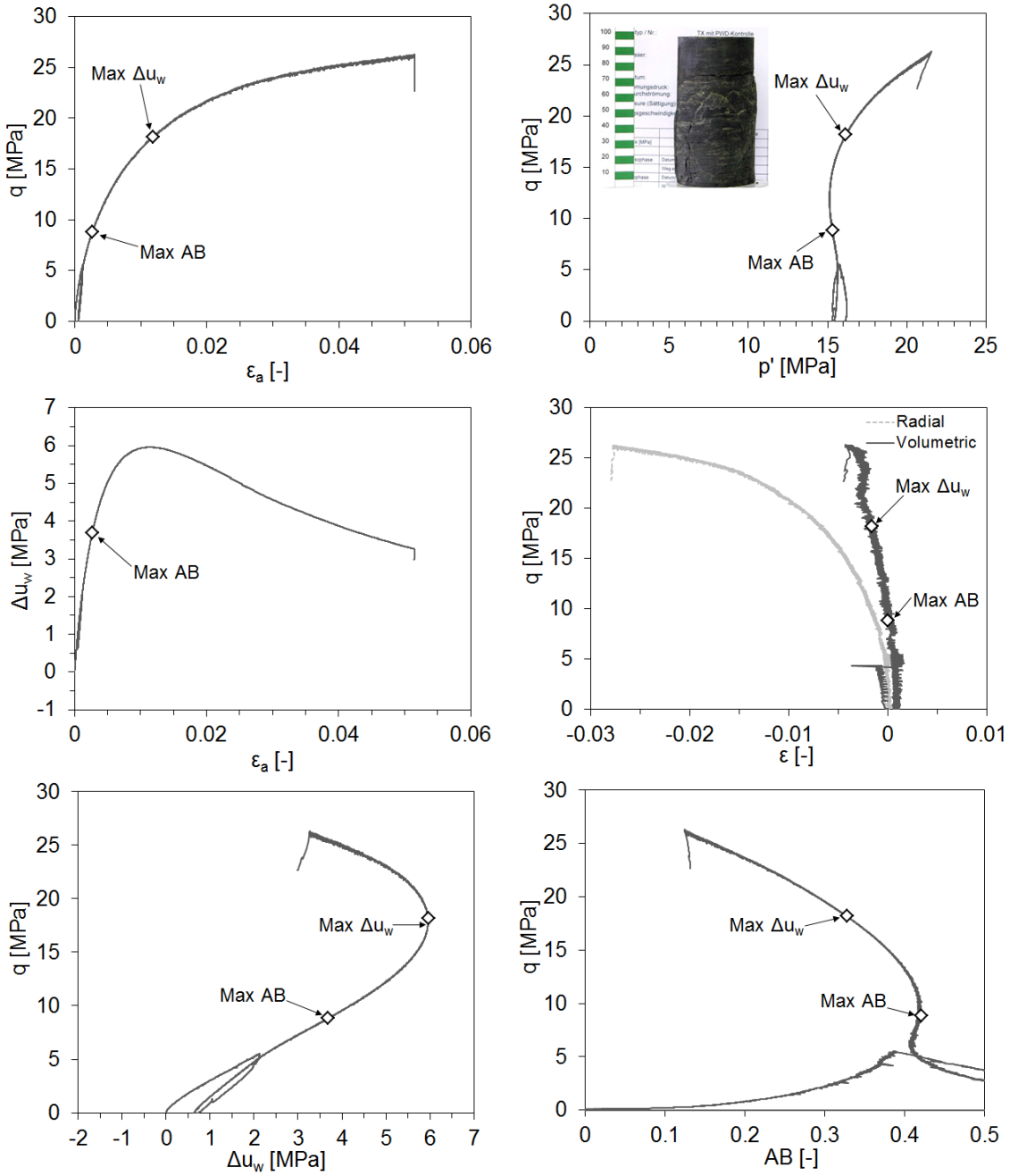

Fig. 51: Results Stage 3 of the multistage Test 7 Lab E at p'_{in} = 16 MPa

The specimen in the Test 8 (Fig. 52) showed a clear brittle failure and an oblique fracture can be observed in the picture of the specimen after testing. As anticipated previously, the radial and volumetric strain cannot be considered reliable.

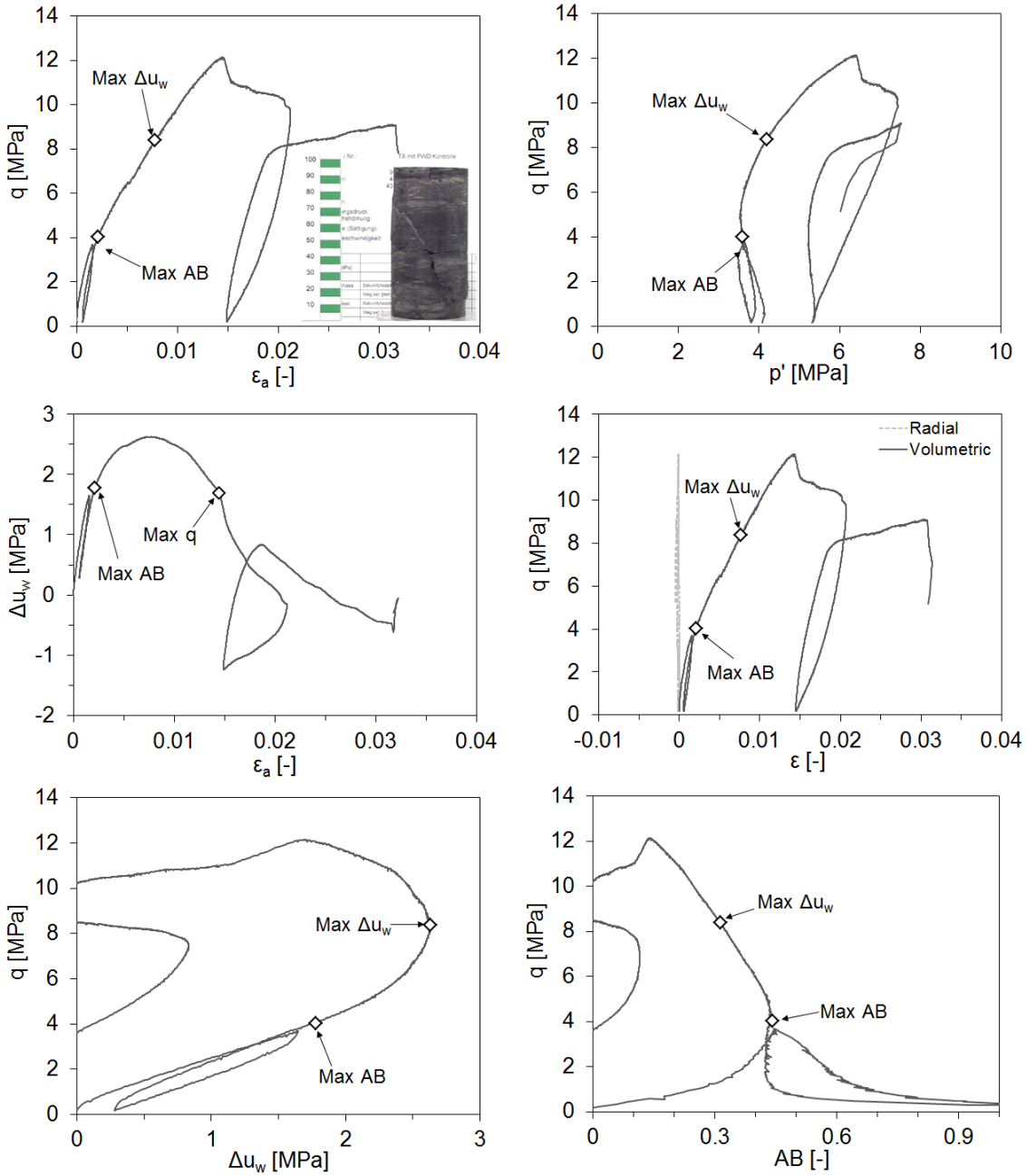

Fig. 52: Results Test 8 (BGC2-15-2) Lab E at p'_{in} = 4 MPa

7 Elastic response

All the presented elastic parameters in this section (elastic moduli and Poisson's ratio) refer to undrained conditions. Unloading/reloading cycles were performed to estimate the elastic response of the material during an unloading process. According to the testing procedure suggested by Nagra, the cycles should have been carried out during the shearing of the specimens before the achievement of the peak stress and after the failure of the specimens once ultimate conditions are achieved; in particular, the unloading phase should have been performed until an axial strain of 0.001 is exhibited by the specimen. These prescriptions were however not always strictly respected. The unloading phase of the cycles allows the determination of the secant undrained elastic modulus (E_{uc}), which was computed as the ratio between the axial stress interval ($\Delta\sigma_a$) and the corresponding axial strain variation experienced by the specimen ($\Delta\varepsilon_a$). Fig. 53 illustrates an example of unloading-reloading cycle with graphical identification of the undrained elastic modulus during the unloading phase.

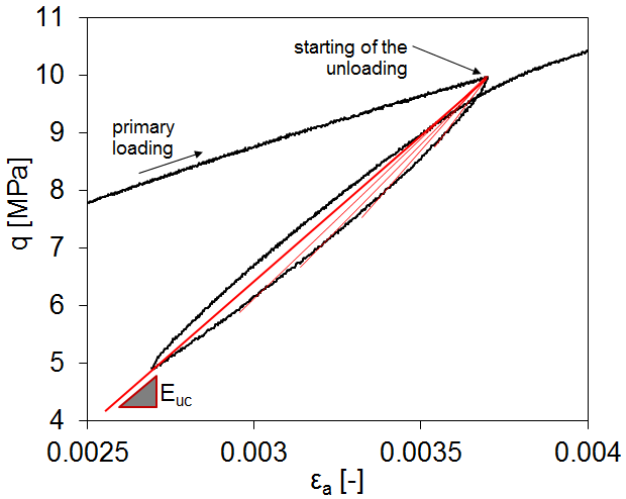

Fig. 53: Example of unloading-reloading cycle with determination of the secant undrained elastic moduli (E_{uc}) during the unloading phase (Lab B Test 3)

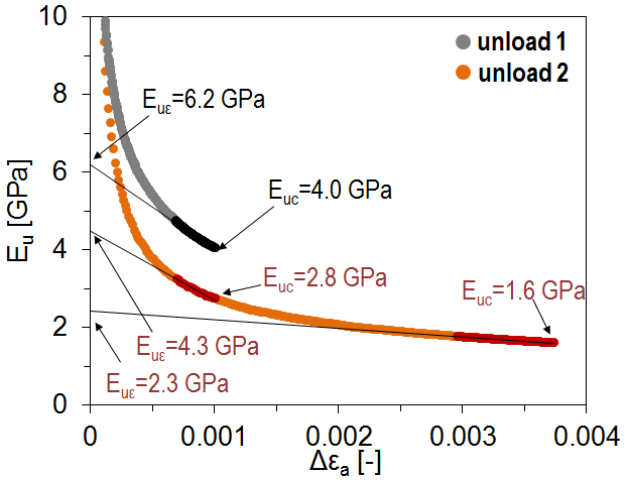

Fig. 54: Undrained elastic moduli measured on the unloading phase of the cycles performed before and after specimen's failure in the Test 2 Lab A

Small-strain moduli ($E_{u\varepsilon}$) were also evaluated from the stress cycles according to the procedure presented in Giger et al. (2018). An example of their determination and comparison with the secant moduli E_{uc} is presented in the Fig. 54 for the Test 2 performed by Lab A; the graph shows the evolution of the secant moduli with the axial strain range used for their computation, for the unloading phase of the cycles performed before (Unload 1) and after (Unload 2) specimen's failure. A clear nonlinear decrease of the moduli is observed with the axial strain, which reflects the nonlinearity of the material's response. This feature highlights the importance of the axial strain range adopted to perform unloading-reloading cycles. Different ranges lead to different moduli, making the comparison among the tests difficult and misleading. Generally, larger strain ranges lead to lower moduli (both E_{uc} and $E_{u\varepsilon}$).

In the following figures (Fig. 55 to Fig. 59) the analysis of the undrained elastic moduli on the unloading phase of the cycles before and after specimens' failure is presented for all the performed tests. Beside the nonlinear evolution of the moduli, three main features are observed. (i) Small strain moduli are always higher than the secant moduli computed over the entire strain range. (ii) The moduli computed on the unloading phase performed after specimen's failure are usually lower than those obtained on the unloading phase carried out before failure. Exceptions to this feature are limited to the sandy OPA. (iii) In the case of P-tests, higher values of the undrained elastic moduli with respect to S-tests are observed.

In the tests by Lab A (Fig. 55), the indicated axial strain range (0.001) was almost always respected for the Unload 1 but not for the Unload 2. This aspect further highlights the dependence of the moduli on the strain. In the Test 4 (P-test), a lower axial strain range (0.00048) was observed for the Unload 1; this strain was experienced during a complete unloading of the specimen, meaning that the deviatoric stress was almost completely decreased to zero MPa. Therefore, in the case of P-tests, the definition of the deviatoric stress to start the unloading phase of the cycle should be carefully considered in order to allow the specimens to experience the desired axial strain for the evaluation of the elastic response. In the Test 6 (sandy OPA), higher moduli were observed in the second cycle (Unload 2). This feature might be related to the response of the specimen observed during the shearing phase (Fig. 27), where a complete brittle failure was not exhibited.

A better consistency in terms of axial strain can be observed in the Fig. 56, which illustrates the response of the tests performed by Lab B. Also in this case, the specimen in the P-test (Test 4 in Fig. 56) experienced a low axial strain due to the limited stress interval available at the starting of the unloading phase; the second unloading (Unload 2) was not performed in this test. Moreover, the sandy specimen in the Test 7 (Fig. 56) exhibited higher moduli for the Unload 2; this aspect might be related again to the response during the shearing phase, where the fluid back pressure dropped to zero and a clear failure of the material was not observed.

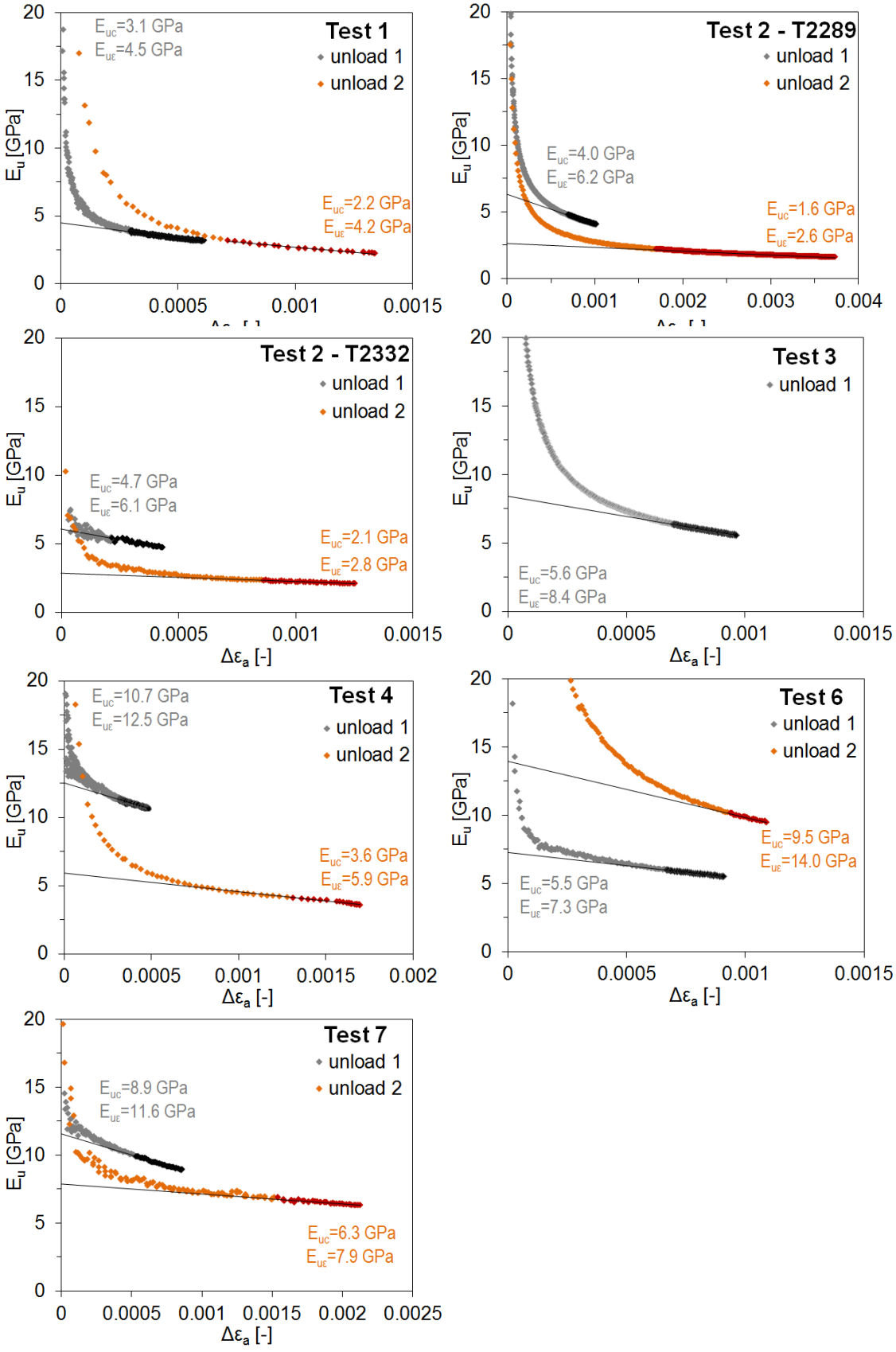

Fig. 55: Analysis of the elastic response during the cycles in the tests performed by Lab A

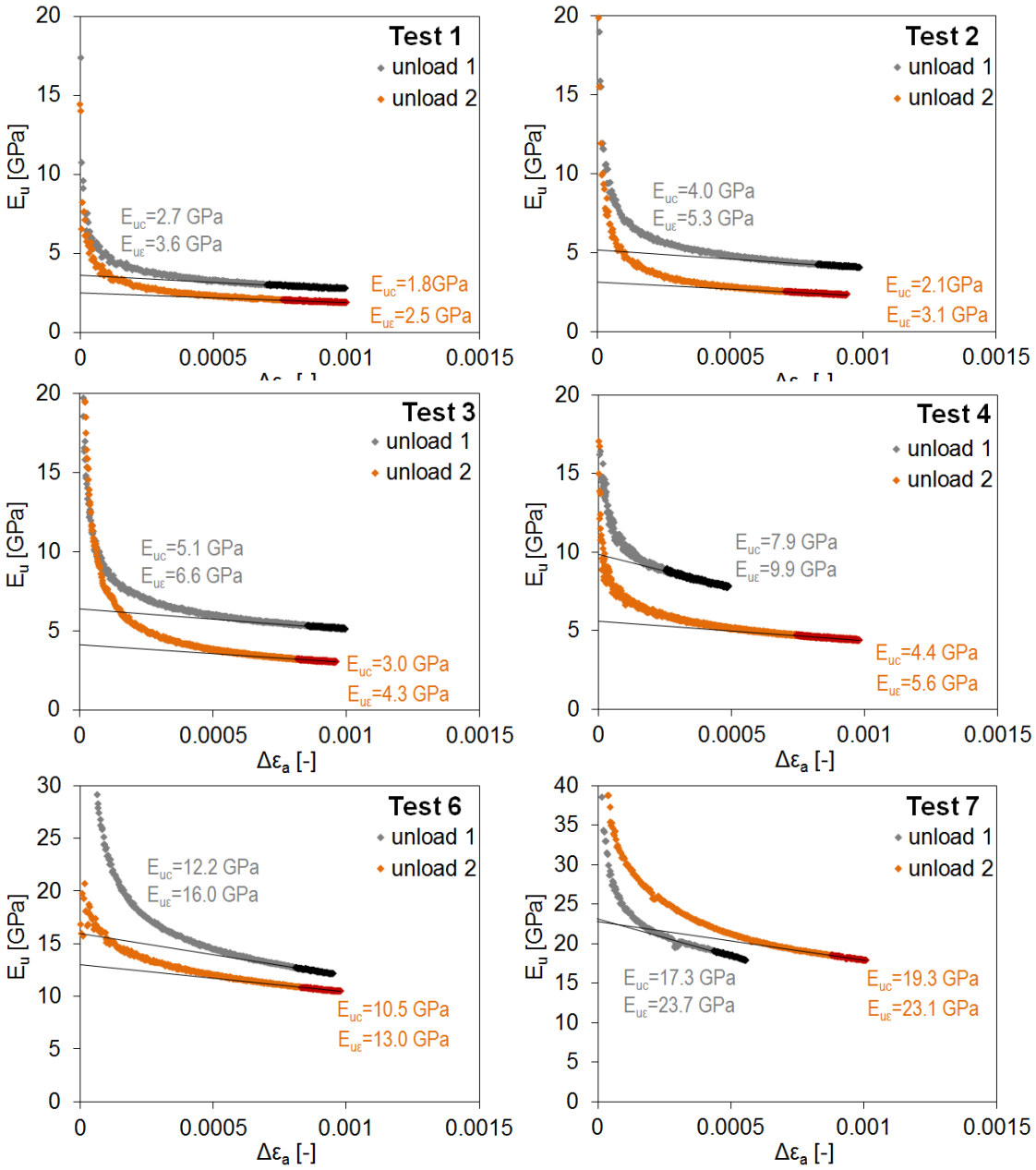

Fig. 56: Analysis of the elastic response during the cycles in the tests performed by Lab B

Four tests performed by Lab C included unloading-reloading cycles (Fig. 57). The P-test (Test 4 in Fig. 57) exhibited an axial strain lower than 0.001, for the same reason explained above for Lab A and Lab B. The cycle "Unload 1" in the Test 3 was performed with a higher strain interval (~ 0.003) than the target value (0.001). The slightly higher scatter observed in the graphs of the Fig. 57 compared the results of the other contractors was related to the resolution of the system used to measure the axial force; a clear trend of the moduli is however well highlighted.

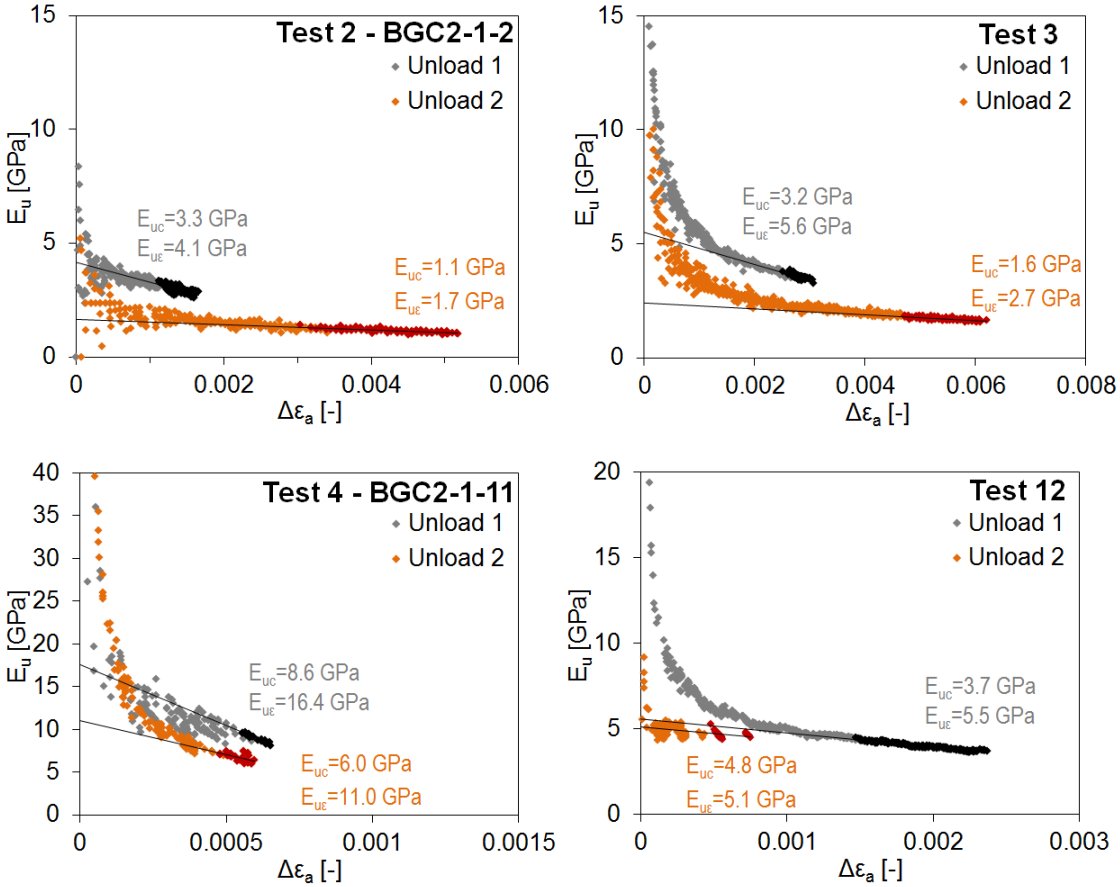

Fig. 57: Analysis of the elastic response during the cycles in the tests performed by Lab C

The results related to the tests carried out by Lab D are presented in the Fig. 58. Only one cycle before failure was performed in the Test 6. The Test 6 and Test 8 (BGC2-17-1) do not show a clear peak and post-peak response. This feature might be again responsible for the higher moduli observed in the second cycle (Unload 2) of the Test 8 (BGC2-17-1).

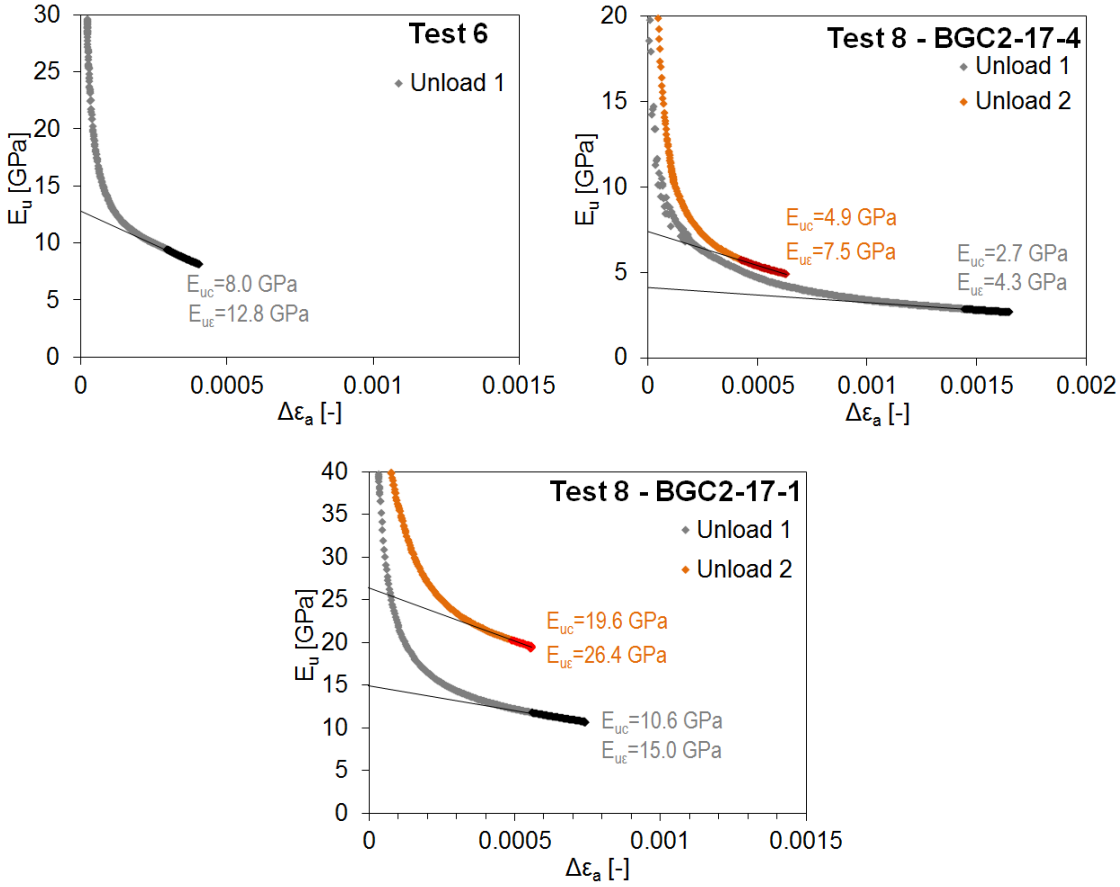

Fig. 58: Analysis of the elastic response during the cycles in the tests performed by Lab D

Fig. 59 shows the response for the tests performed by Lab E. An important aspect of these tests is that the second unloading (Unload 2) in the Test 6 and Test 8 was always carried out by reducing the deviatoric stress to almost 0 MPa. For this reason, the axial strain intervals of the second unloading (Unload 2) presented in the graphs of Fig. 59 were significantly higher than those of the first unloading (Unload 1). This feature led to significant lower moduli measured on the cycle after failure, as in the case of the Test 8 (Fig. 59).

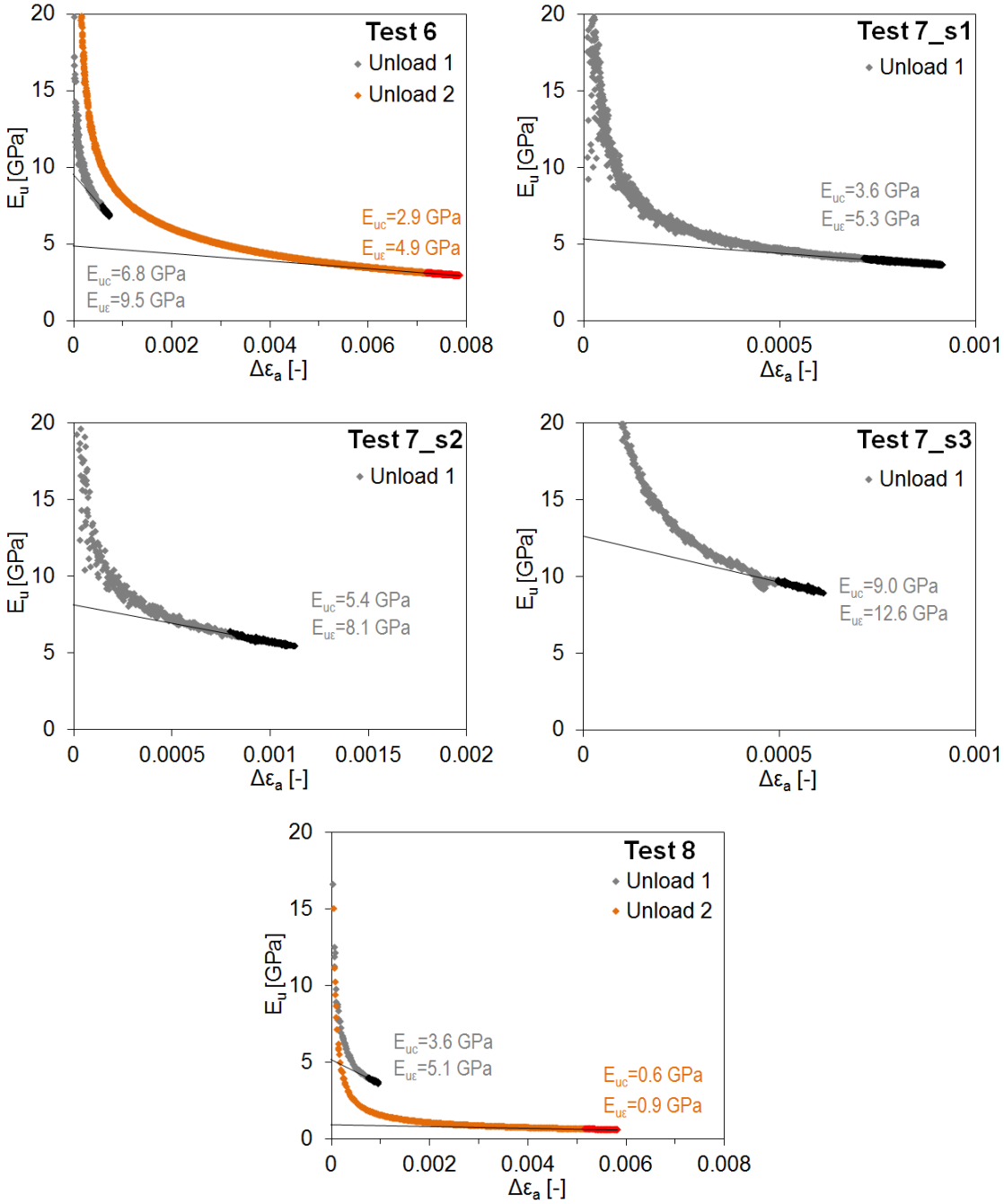

Fig. 59: Analysis of the elastic response during the cycles in the tests performed by Lab E

A summary of the measured undrained elastic moduli as function of the mean effective stress is reported in Fig. 60 the for the S-tests on the shaly OPA, in Fig. 61 for the S-tests on the sandy OPA, and in Fig. 62 for the P-test on the shaly OPA. It has to be considered that the unloading-reloading cycles were not performed in all of the tests (please refer to the graphs in the Chapter 6 for the details of each test).

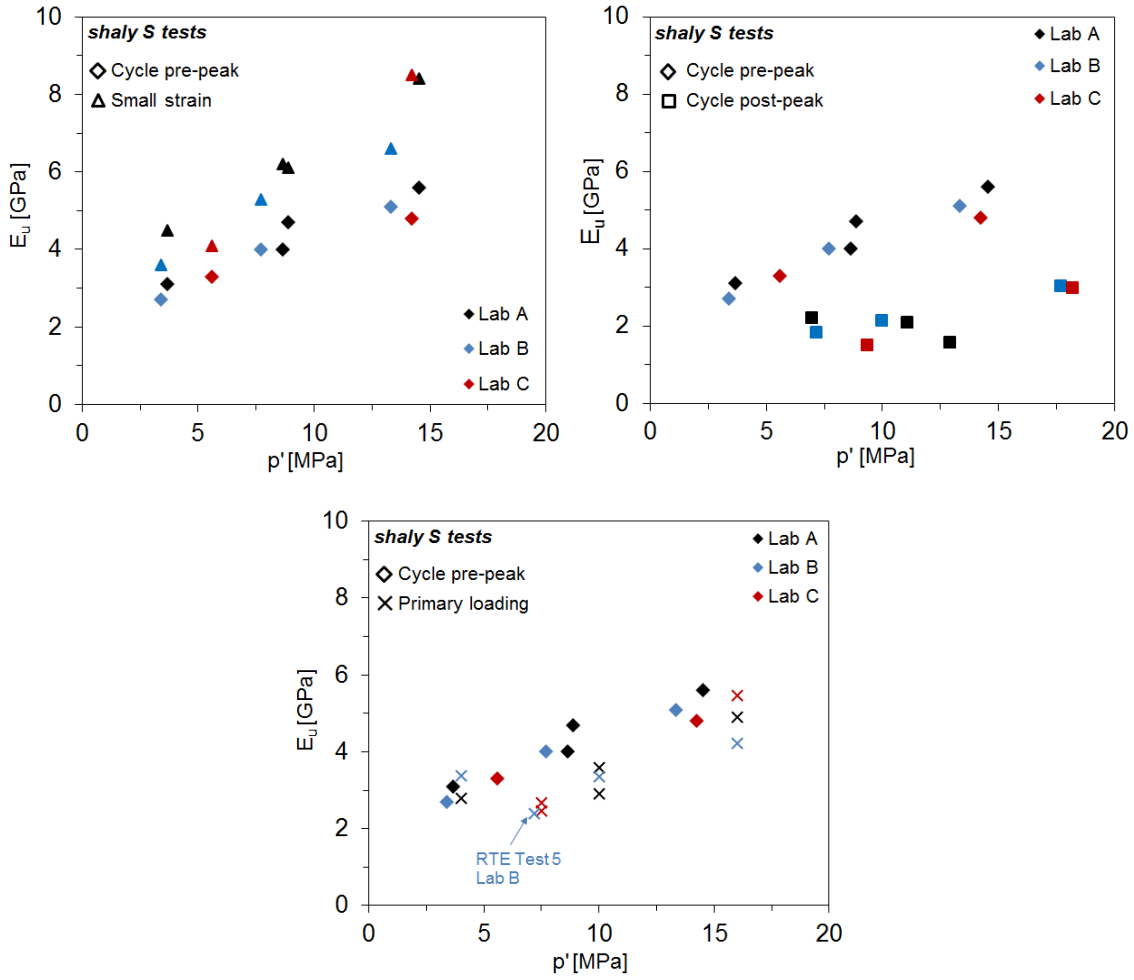

Fig. 60: Comparison of the undrained elastic moduli for the S-tests performed on the shaly OPA

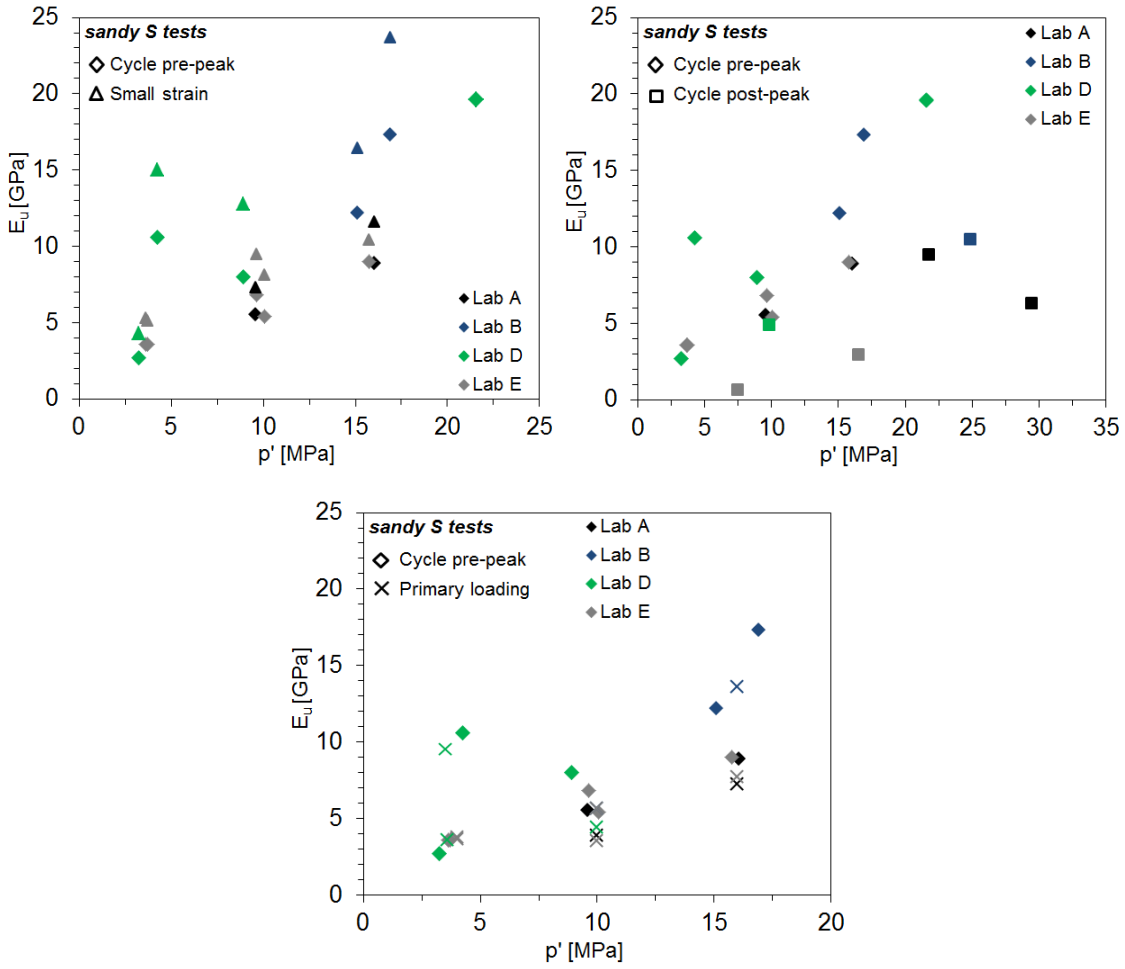

Fig. 61: Comparison of the undrained elastic moduli for the S-tests performed on the sandy OPA

For the S-tests on the shaly OPA, the following three main features can be highlighted: (i) the dependence of the moduli on the mean effective stress (p'), (ii) the influence of the strain range cosidered to obtain the moduli (*Small strain* moduli are greater than *Cycle pre-peak* moduli), (iii) the decrease of the the secant elastic moduli after the failure of the specimen (*Cycle post-peak* are lower than *Cycle pre-peak*). Regarding the *Primary loading* moduli, they are slightly lower than the *Cycle pre-peak* moduli; their value is however strongly dependent on the selected axial stress-strain range (a stress range of 20 – 25 % of the peak stress was considered here).

Similar considerations can be made for the S-tests on the sandy OPA (Fig. 61). However, in this case the scatter among the points is higher due to the more significant heterogenety of the tested specimens. Overall, the sandy OPA specimens exhibited higher values compared to the shaly OPA specimens (Fig. 60).

The results obtained from the P-tests on the shaly OPA highlighted the elastic anisotropy of the material. Indeed, the graph in Fig. 62 shows higher values of the undrained elastic moduli compared to the moduli obtained in the S-tests (Fig. 60).

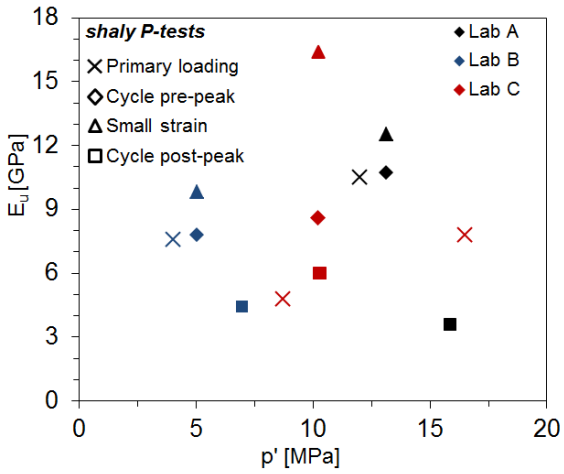

Fig. 62: Comparison of the undrained elastic moduli for the P-tests performed on the shaly OPA

In terms of radial response, the relationship between axial and radial deformations during the unloading phase of the cycles performed before the achievement of the peak stress was used for the assessment of the undrained Poisson's ratio (ν_u). Deviations from the theoretical value of 0.5 typically obtained from the linear isotropic elasticity are due to the anisotropic features of the material and possible poroelastic effects. Fig. 63 shows an example of the relationship between the two strains during the unloading phase of the cycles of an S-test (Test 3 Lab B) conducted on the shaly OPA. The obtained linear relationships allowed the estimation of the undrained Poisson's ratio. Similar trends were observed also for the other tests. A summary of the values obtained from the S-tests carried out on shaly and sandy specimens is presented in the Fig. 64. The values of ν_u are in the range between 0.3 and 0.5.

Regarding the cycles carried out after the failure of the specimens, the presence of the failure plane and the measurement of the radial displacement with punctual transducers might lead to a misleading evaluation of the radial response. For these reasons, the cycles after the peak stress were not used for the evaluation of the radial elastic response.

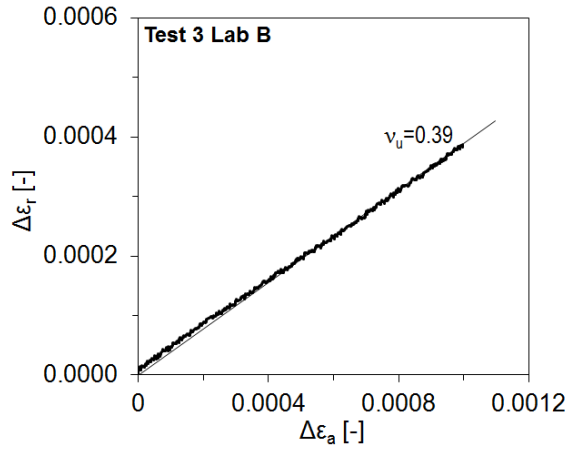

Fig. 63: Relationship between axial and radial strains during the unloading phase of the pre-peak cycle performed in the Test 3 Lab B

A significant anisotropic response is observed in the case of P-tests. Indeed, the presence of the bedding planes influences significantly the response of the specimens in the radial directions, with a higher deformation in the direction perpendicular to bedding than in the direction parallel to bedding. Fig. 65 illustrates an example (Test 4 Lab B) of the relationship between the axial strain and the two radial strains. A linear relation is always observed for both radial deformations. A value of undrained Poisson's ratio can be estimated for each direction. The reported values clearly highlight the anisotropic response of the material. A summary of the values obtained for the P-tests performed on the shaly OPA is presented in Fig. 66.

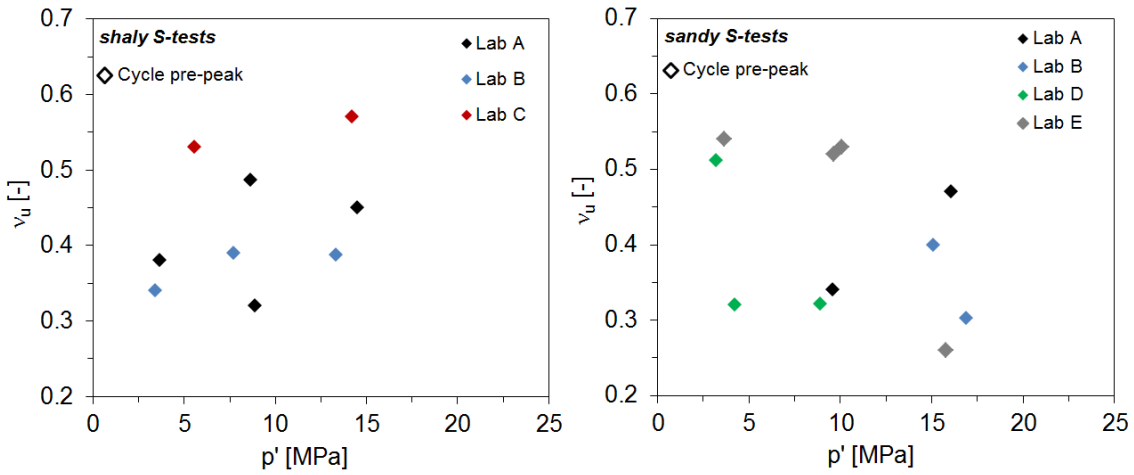

Fig. 64: Relationship between the mean effective stress and the undrained Poisson's ratio for the S-tests performed on the shaly OPA (left) and sandy OPA (right)

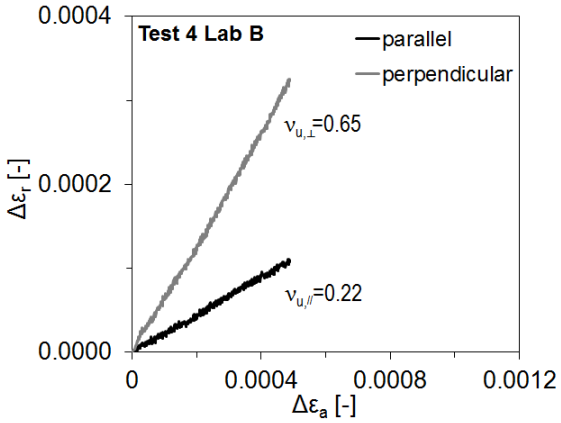

Fig. 65: Relationship between radial strains (perpendicular ⊥ and parallel // to bedding) and axial strain for a P-test performed on shaly specimen (Test 4 Lab B)

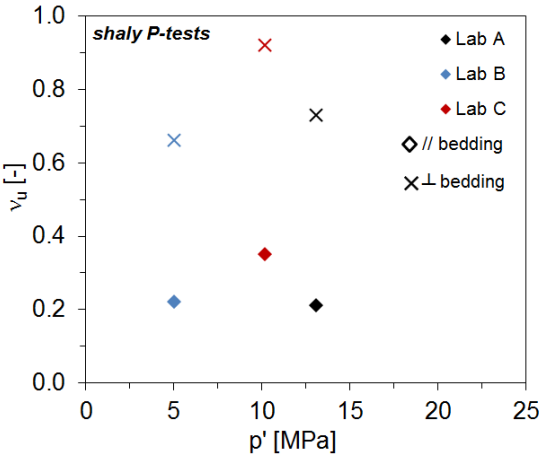

Fig. 66: Relationship between the mean effective stress and the undrained Poisson's ratio for the P-tests performed on the shaly specimens

Ultrasonic velocities of P (V_p) and S (V_s) waves were also measured by three laboratories: Lab A, Lab B, and Lab C. In particular the Lab A and Lab C measured the velocity of both P and S waves in the axial direction (Vp_z and Vs_z). The Lab B measured only the velocity of P waves but in the axial (Vp_z) and radial (Vp_h) directions. These configurations allowed the estimation of the wave velocities considering the anisotropic structure of the tested specimens (bedding orientation).

The following analysis focuses on the velocities measured at the end of the consolidation phase, before the starting of the shearing phase. Fig. 67 and Fig. 68 summarize in particular the relationship between the wave velocities and effective mean stress acting on the specimen at time of the measurement. The presented values are listed in the Tab. 5. The measurement were not performed on all the tested specimens (compare with the tests list in Tab. 1)

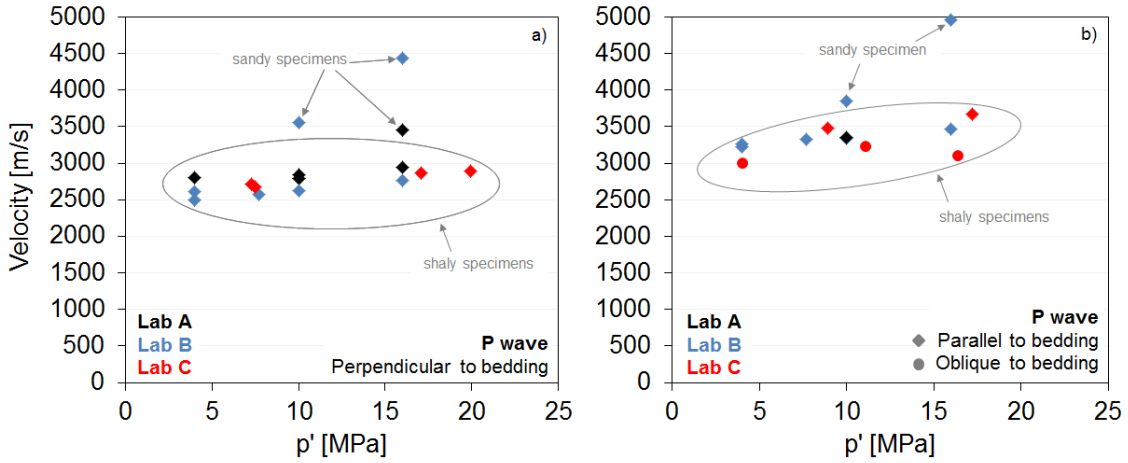

Fig. 67: P-wave velocity measured in the directions a) perpendicular to bedding, and b) parallel and oblique to bedding

The graph a) in Fig. 67 shows the P-wave velocity measured perpendicular to bedding. The graph highlights clearly the impact of the heterogeneity. Shaly specimens exhibited values between 2'500 m/s and 3'000 m/s, while the sandy specimens exhibited higher values with larger scatter. The velocity of P-wave in the direction parallel and oblique to bedding was higher than perpendicular to bedding. This aspect is highlighted in the graph b) of Fig. 67 that shows values in the range between 3'000 m/s and 4'000 m/s. Also in this case, the sandy specimens exhibited higher values than shaly specimens.

The graphs in the Fig. 68 illustrate the relationship between the S wave velocity and the effective mean stress. Lower values compared to P wave velocity were observed. As previously mentioned only the Lab A and the Lab B performed this measurement. The comparison between the graph a) and the graph b) in Fig. 68 highlights again the impact of anisotropy, which in this case is less pronounced compared to the P wave. The velocity of the S wave parallel to bedding were slightly higher than the in the direction perpendicular to bedding.

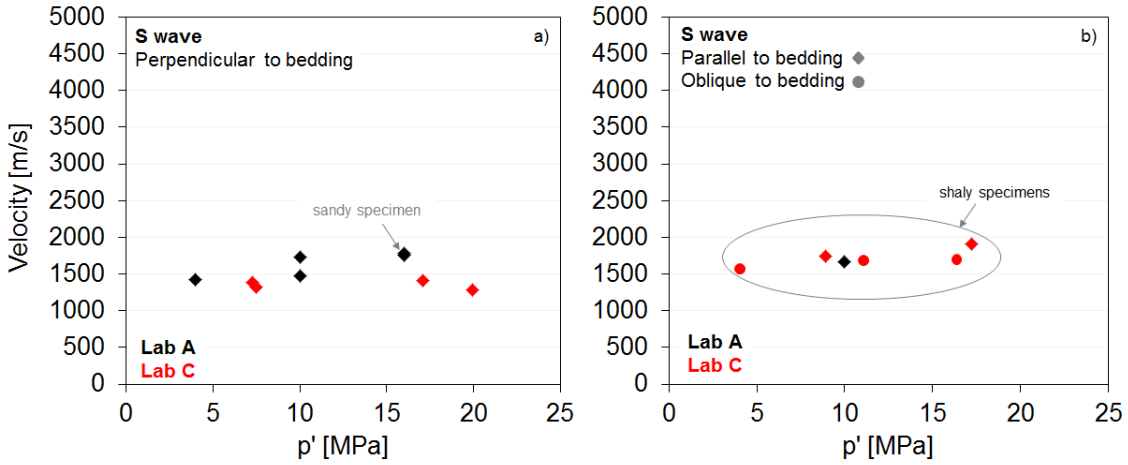

Fig. 68: S wave velocity measured in the directions a) perpendicular to bedding, and b) parallel and oblique to bedding

Tab. 5: P and S wave velocities measured on the tested specimens at the end of the consolidation phase

Lab	**Test ID**	**Test #**	**sig'** [MPa]	**Bedding**	**vp_z** [m/s]	**vp_h** [m/s]	**vs_z** [m/s]
A	T2303	1	4	S	2'806	-	1'419
A	T2289	2	10	S	2'845	-	1'736
A	T2280	3	16	S	2'941	-	1'758
A	T2300	5	10	S	2'786	-	1'473
A	T2304	4	10	P	3'357	-	1'668
A	T2311	7	16	S	3'458	-	1'770
B	CIU432_2_0	1	4	S	2'608	3'229	-
B	CIU432_2_1	2	10	S	2'630	3'339	-
B	CIU432_2_3	3	16	S	2'769	3'467	-
B	CIU432_2_4	4	4	P	3'259	2'502	-
B	CIU432_2_5	5	7.7	S	2'576	3'324	-
B	CIU432_2_6	6	10	S	3'558	2'846	-
B	CIU432_2_7	7	16	S	4'439	4'958	-
C	BGC2-1-2	2	7.50	S	2'681	-	1'320
C	BGC2-1-4	2	7.25	S	2'711	-	1'387
C	BGC2-1-1	3	17.08	S	2'871	-	1'416
C	BGC2-1-3	5	19.94	S	2'896	-	1'282
C	BGC2-1-11	4	8.92	P	3'475	-	1'741
C	BGC2-1-13	4	17.23	P	3'671	-	1'913
C	BGC2-1-22	10	4.05	Z	3'001	-	1'573
C	BGC2-1-23	11	11.07	Z	3'228	-	1'688
C	BGC2-1-24	12	16.38	Z	3'100	-	1'703

8 Shear strength

This chapter is dedicated to the comparison among the different contractors of the material's response during the shearing phase of the tests. The comparison is mainly focused on the stress paths and the stress-strain relationship, and it aims at assessing the robustness of the experimental methodologies in investigating the hydro-mechanical behaviour with different tests performed by different contractors. The strength parameters are derived in the final part of the section.

8.1 Stress paths and stress-strain response

The stress paths of the S-tests carried out on the shaly OPA are presented in Fig. 69 to Fig. 70. The maximum AB parameter (*max AB*), the maximum pore fluid pressure (*max u*), and the maximum deviatoric stress (*max q*) observed during the shearing of the specimens are reported in the graphs. The figures clearly show that the stress paths are dominated by the interval between the *max AB* and the peak stress (*max q*), with the maximum pore water pressure (*max u*) located in between the two. In particular, a significant part of the stress paths is dominated by a decrease of the pore fluid pressure. This aspect is highlighted by the right curvature of the stress paths and indicates that the failure of the specimens is associated to a dilatant response. A good matching among the tests performed by the different contractors can be observed. This aspect confirms that robust testing of shaly OPA is possible, and experimental results are consistent. In the case of Lab A, the evolution of the stress paths suggests a lower decrease of the mean effective stress during shearing compared to the other contractors. This feature is usually addressed to a lower development of the pore fluid pressure.

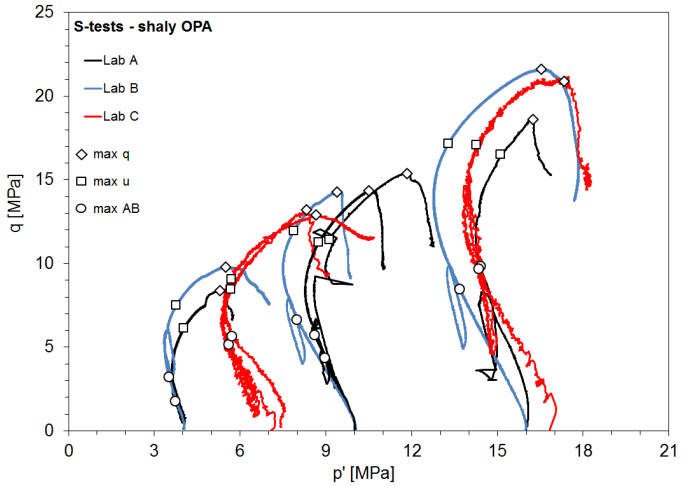

Fig. 69: Comparison of the stress paths for the CTC S-tests performed on the shaly OPA

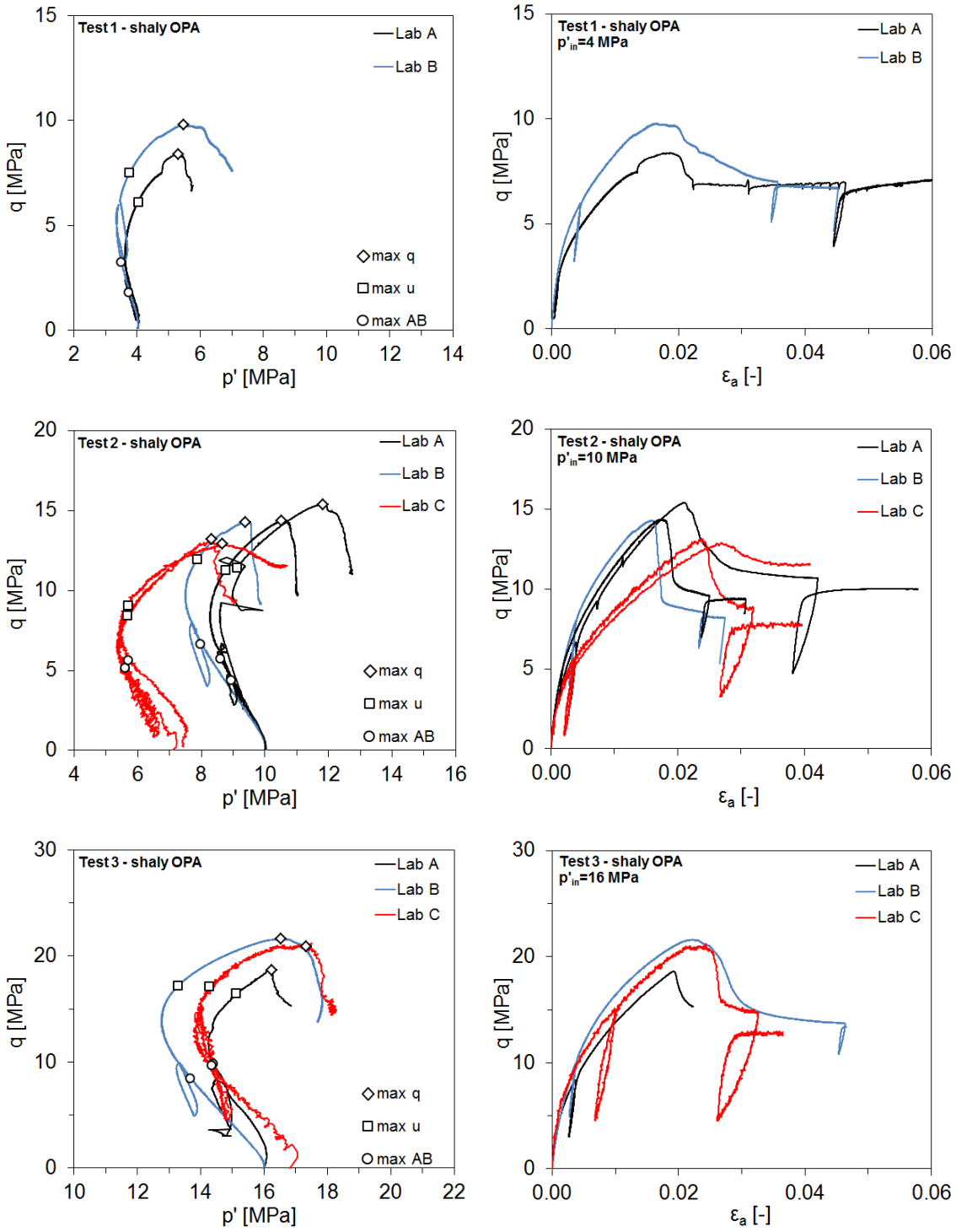

Fig. 70: Comparison of the stress-paths and stress-strain relationships for the Tests 1, 2, and 3 on the shaly OPA (S-tests)

A different stress path is observed for the P-tests performed on the shaly OPA (Fig. 71). The graphs highlight a linear stress path with increase of the mean effective stress until failure; in this case, although the stress paths are still dominated by the interval between *max AB* and peak stress (*max q*), the maximum pore water pressure (*max u*) almost coincides with the peak stress, indicating no volume expansion during the shearing phase. Moreover, P-tests exhibited higher peak stress, lower axial strain at failure (1 %), and more pronounced softening behaviour with respect to S-tests.

The stress paths of the Z-tests carried out on the shaly OPA by Lab C (Fig. 72) are almost vertical and their shape can be considered in between the S and P-tests. The Test 11 shows a slight curvature to the right after the *max AB* suggesting that failure is associated to dilation. No curvature is observed in the Test 10 and Test 12, and the maximum pore water pressure and peak stress are very close. Regarding the Test 12, a possible damage of the specimen before testing might be considered as the possible cause of the low observed peak stress.

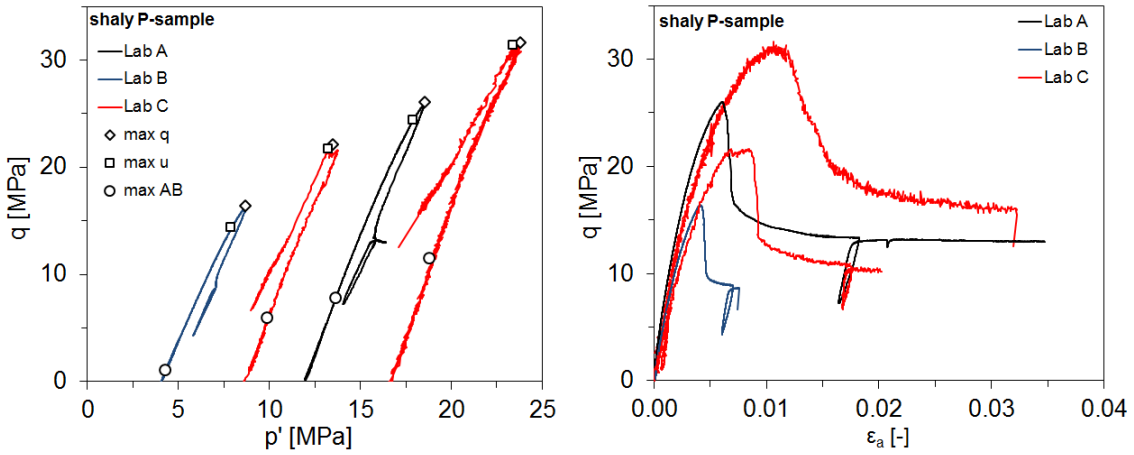

Fig. 71: Comparison of the stress-paths and stress-strain relationships of the P-tests on shaly OPA

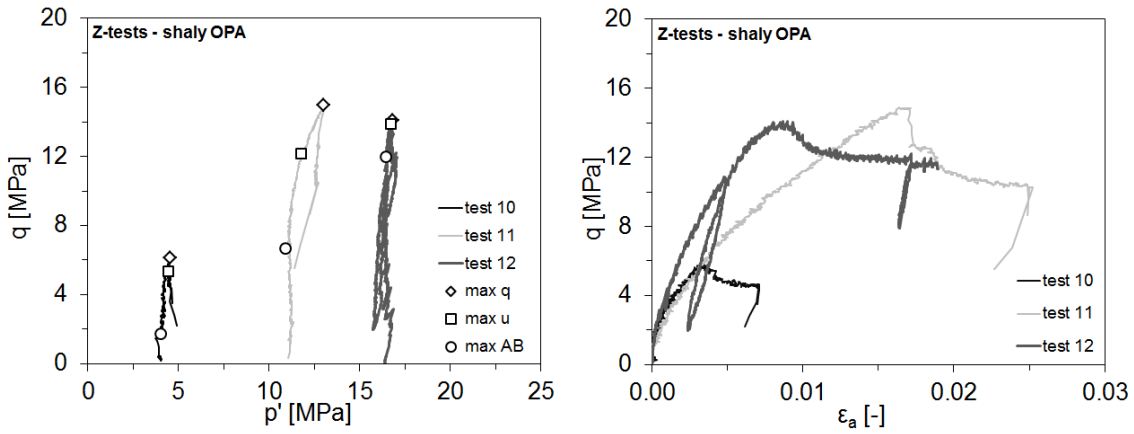

Fig. 72: Comparison of the stress-paths and stress-strain relationships of the Tests 10, 11, and 12 on the shaly OPA (Z-tests Lab C)

Fig. 73 and Fig. 74 illustrate the results of the S-tests performed on the sandy OPA specimens. Note that in Fig. 73 the stress path of the Test 6 (Lab B) and Test 8 (Lab D) are not reported to allow a better comparison among the other tests. As for the S-tests on the shaly OPA, the stress paths are dominated by the interval between *max AB* and *max q*, with *max u* in between. Compared to the shaly OPA, testing the sandy OPA is more challenging due to the heterogeneity of the tested specimens; this aspect is responsible for a more difficult assessment of the testing reproducibility.

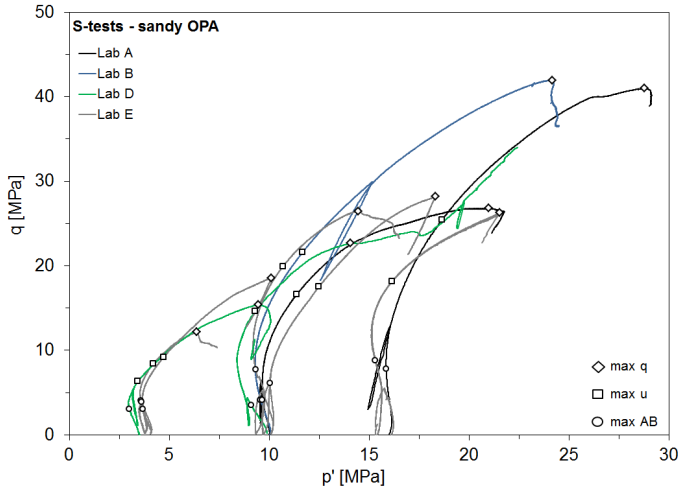

Fig. 73: Comparison of the stress paths for the S-tests performed on the sandy OPA specimens

The S-tests on the sandy OPA highlighted a significant decrease of pore pressure during shearing before the achievement of the peak stress. This feature is highlighted in Fig. 75 where a comparison of the maximum pore pressure ($\Delta u_{w,max}$) and the pore pressure at failure ($\Delta u_{w,f}$) between the S-tests on the shaly and sandy OPA is presented. The graphs clearly illustrate that the shaly and sandy OPA specimens exhibited similar values of the maximum pore water pressure ($\Delta u_{w,max}$). However, once the failure was achieved, the pore pressure in the sandy specimens was significantly lower than in the shaly specimens. This difference between the two facies might be related to the different volumetric response of the materials during the shearing phase. In particular, the maximum values of the pore water pressure presented in Fig. 75 highlight the lower values for the Lab A tests compared to the other contractors; this aspect supports the hypothesis of a leakage in the system that would affects the increase of pore pressure (and the mean effective stress) during shearing.

Regarding the stress-strain response, as already anticipated in the Chapter 6, a different behaviour compared to the S-tests on the shaly OPA is observed, which is characterized by the absence of clear peak stress and brittle failure Moreover, the matching among the contractors is not well defined as in the case of the S-tests on the shaly OPA. The reason of this aspect is mainly related to the more heterogeneous mineralogical composition of the sandy OPA specimens with respect to the shaly OPA specimens. To highlight this feature and partially take it into account, the water content (w) of each tested sandy OPA specimen is reported in the graphs in Fig. 74, and a rough relationship with the exhibited peak stress can be observed.

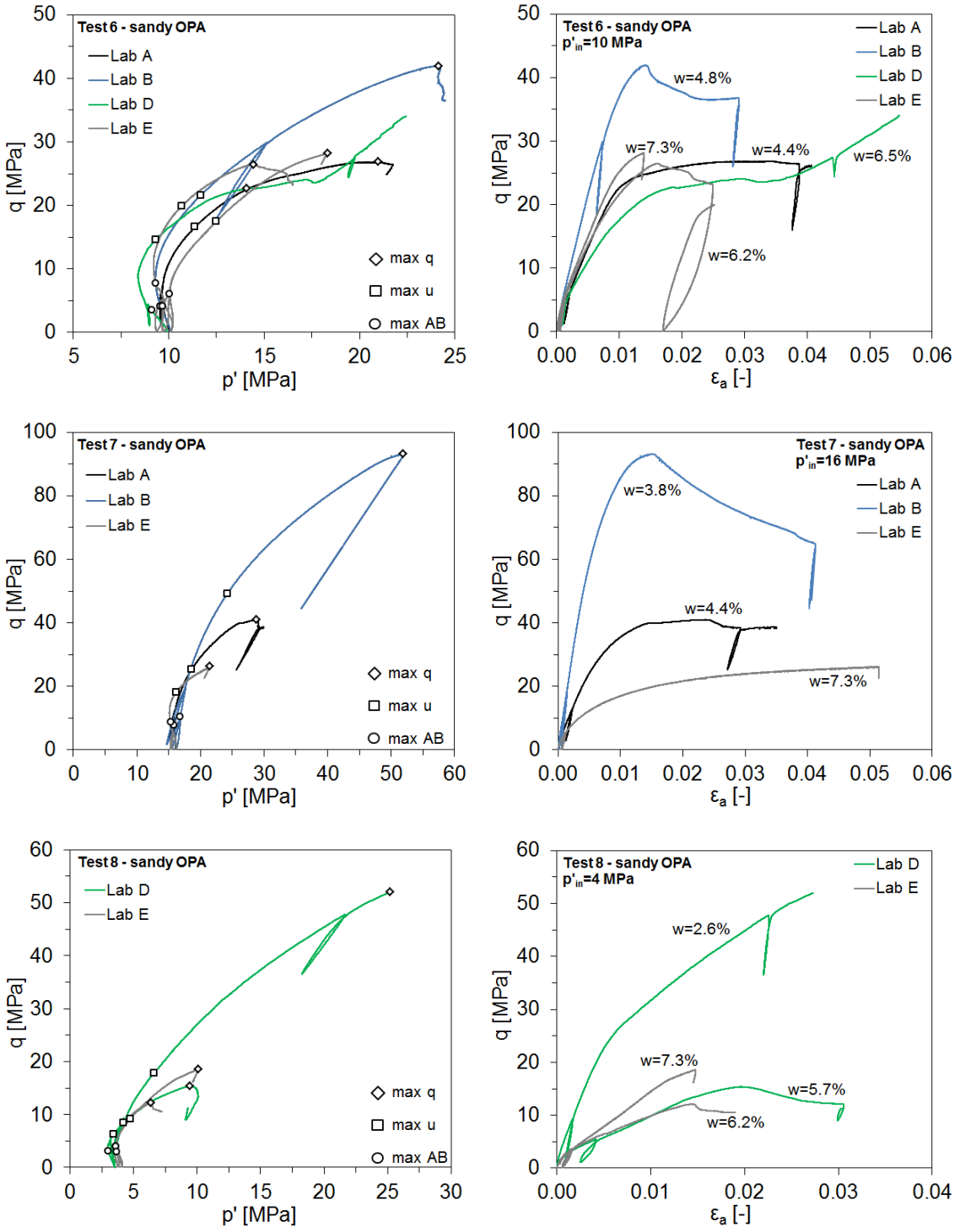

Fig. 74: Comparison of the stress-paths and stress-strain relationships for the Tests 6, Test 7, and Test 8 on the sandy OPA specimens (S-tests)

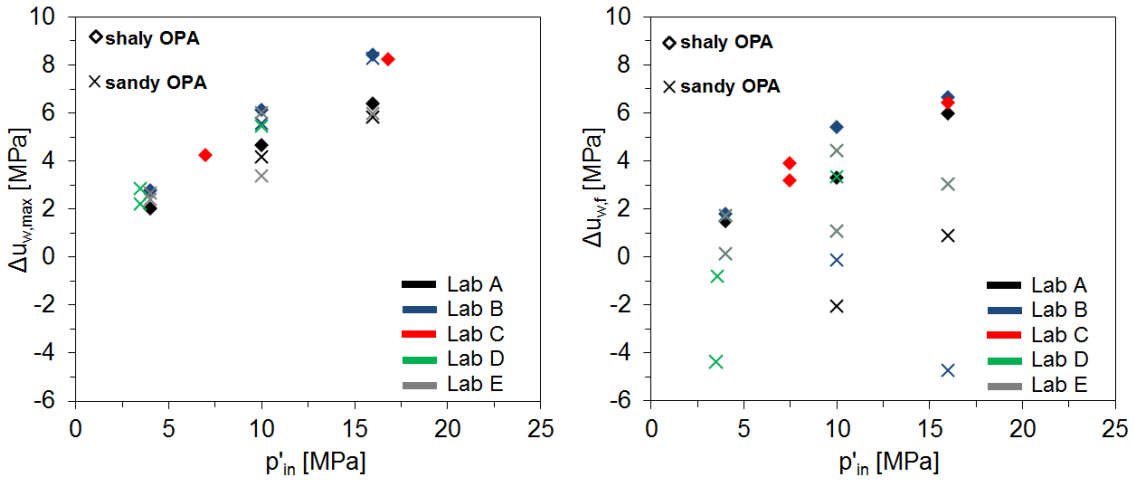

Fig. 75: Maximum pore water pressure ($\Delta u_{w,max}$) and pore water pressure at failure ($\Delta u_{w,f}$) for the S- tests on the shaly and sandy OPA specimens

8.2 Shear strength envelopes

The obtained strength values from the tests are summarized in this section for both the shaly and sandy OPA. It is important to consider that the shaly OPA specimens were more homogeneous in terms of mineralogical composition than the sandy OPA specimens (see Tab. 4, Chapter 4).

Fig. 76 presents the results for the S-tests on the shaly OPA. Four different strength envelopes are illustrated in the graph: peak strength (that refers to the *max q*), post-peak strength, maximum pore fluid pressure (that refers to the *max u*), and maximum AB (that refers to the *max AB*). The corresponding values of effective intercept cohesion (c') and effective shear strength angle (φ') are reported in the figure. A reduction of both c' and φ' is observed in the post-peak envelope, which indicates the brittle failure of the specimens. The *max AB* envelope highlights the stress state when the material starts to experience a reduction of the rate of increase of the pore fluid pressure, and it can be associated to the onset of the volumetric expansion of the specimens during shearing.

Fig. 77 shows a comparison between the S-tests and P-tests on the shaly OPA. The specimens tested parallel to bedding (P-tests) exhibited higher peak strength than the specimens tested perpendicular to bedding (S-tests). On the other hand, similar post-peak strength values were observed in both P and S-tests. This aspect is supported by the observed failure plane in the specimens after testing, which is crossing the bedding in both types of tests. Regarding the P-tests, the *max u* and *max AB* envelopes are not represented in Fig. 77. As the maximum pore fluid pressure is very close to the peak deviatoric stress; this feature indicate that the fluid pressure is increasing almost until the failure of the specimen, suggesting a negligible impact of the volumetric expansion of the specimens during the shearing. A confirmation of this aspect is given by the evolution of the AB parameter with deviatoric stress (see Fig. 25, Fig. 32, Fig. 39, Fig. 40), which is almost constant. Therefore, the use of the *max AB* envelope to evaluate the onset of the plastic behaviour might lead to a misleading interpretation of the hydro-mechanical behaviour of the material.

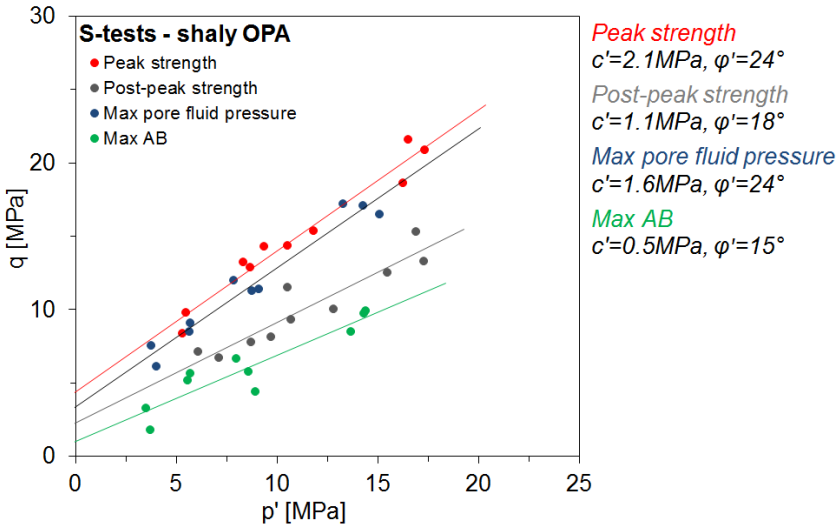

Fig. 76: Strength values for the S-tests performed on the shaly OPA

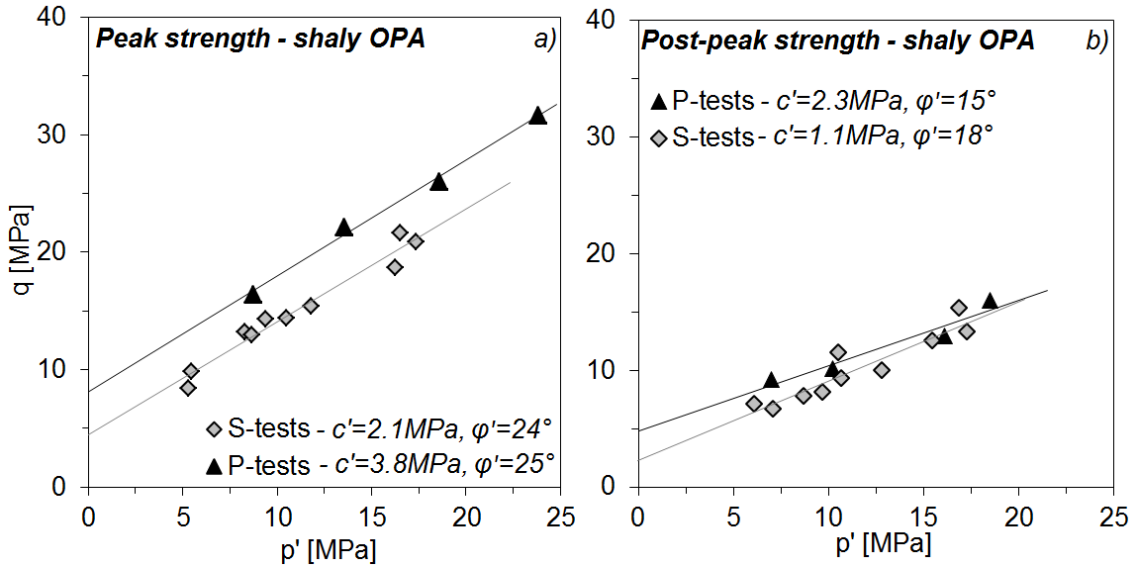

Fig. 77: Comparison between S-tests and P-tests of the peak and post-peak strength values

Fig. 78 illustrates the alternative stress paths considered in the benchmark programme (Tests #5 in the Tab. 1). The three stress paths (RTE, CTE, and TC) are compared with the peak stress obtained from CTC tests performed on the specimens loaded perpendicular (S-tests) and parallel (P-tests) to bedding to evaluate possible differences of strength related to alternative loading configurations. In particular, to have a more direct comparison, the absolute value of the deviatoric stress is considered for the two extension tests.

The CTE test carried out by the Lab A exhibited a similar stress path to P-tests in Fig. 71. This feature is reasonable considering that the specimen was loaded parallel to the bedding, as in the case of CTC P-tests. The observed peak stress is slightly lower than the values measured with CTC tests. Regarding the RTE test performed by Lab B, as already anticipated in the Section 6.2, the back pressure decreased to 0 MPa during the reduction of the axial stress and before the failure of the specimen. This result suggested that a higher initial pore fluid pressure should be considered when the RTE stress path is going to be adopted to study the mechanical response of the material in extension with undrained conditions. The TC test carried out by Lab C exhibited a similar stress path to CTC S-tests; the observed peak stress is in this case slightly higher than the values observed in CTC S-tests. In summary, the considered alternative stress paths highlighted some differences with respect to the stress path evolution, without however significant discrepancies in terms of peak stress.

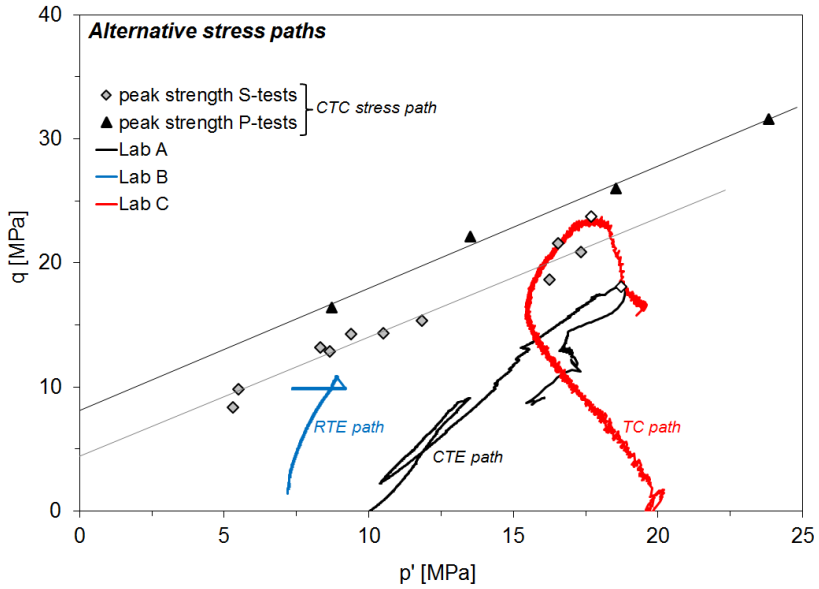

Fig. 78: Results of the tests performed with alternative stress paths with comparison to peak strength from CTC tests

The evaluation of strength envelopes is more difficult for the sandy OPA specimens due their heterogeneity. Fig. 79 shows all the obtained peak strength values. From the data of the mineralogical composition, most of the specimens exhibited a clay mineral content between 28 % and 35 %, while the calcite content was between 10 % and 20 %. However, as highlighted in the Fig. 79, there were some specimens outside these ranges, as in the case of Lab B Test 7 and Lab D Test 8 (BGC2-17-1) where the significant amount of calcite (> 40 %) was probably responsible for the high observed strength values. The clear impact of heterogeneities can be also observed in the pictures of the specimens after testing. Moreover, it has to be taken into account that some of the tests experienced some issues, and the observed peak strength values might not be considered completely reliable. This was the case for the Test 6 and Test 7 by Lab A (Fig. 27 and Fig. 28) where no clear brittle failure was exhibited, the Test 7 by Lab B (Fig. 35) where the pore fluid pressure dropped to 0 MPa before the achievement of the peak stress, the Test 6 by Lab D (Fig. 45) where an unrealistic stress-strain relationship was observed.

Due to these reasons, the strength envelopes are not presented for the sandy OPA specimens. Indeed, although the points in the Fig. 79 show a rough linear trend, as a misleading evaluation of the strength parameters would be obtained due to the heterogeneity of the tested specimens.

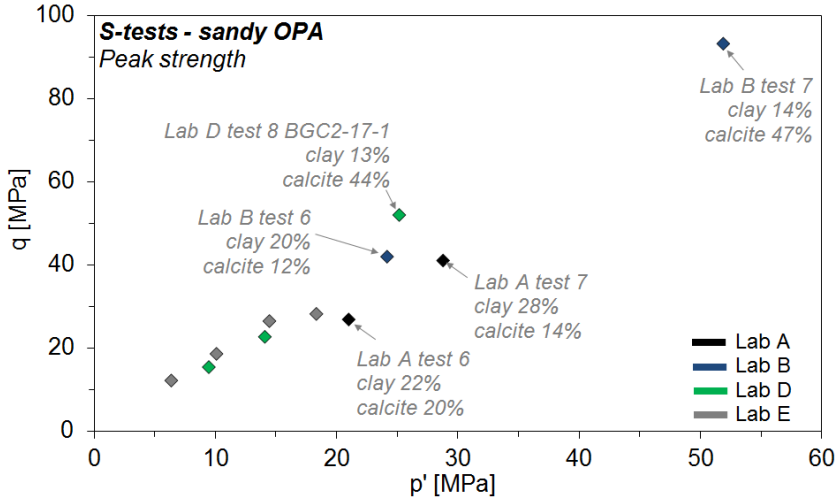

Fig. 79: Peak strength values for the S-tests performed on the sandy OPA

9 Conclusions

The results of a benchmark study on undrained triaxial testing of Opalinus Clay is documented. The main goal of the study was the evaluation of two different testing procedures (named conventional and alternative procedure, respectively) to perform the laboratory tests. Core samples extracted from the shaly and sandy facies in the Mont Terri URL were tested at different confining effective stresses. Shaly OPA specimens were tested with different bedding orientations with respect to the axial loading (S, P, Z).

Considering the major outcomes of the benchmark study, it is possible to conclude that consistent experimental results were obtained when the planned testing procedures were respected by the contractors. This aspect was particularly relevant in the case of the shaly OPA where the potential of both testing procedures (conventional and alternative) for the saturation phase of the tests was demonstrated. Moreover, the measurements of the Skempton's B coefficient proved to be an efficient way to assess the saturation of the specimens before the shearing phase; complete consolidation to the target effecting confining stress was properly carried out in all the tests with conventional procedure, and the adopted strain rates can be considered appropriate for the performance of the shearing phase and the proper assessment of the pore water pressure evolution.

These results prove that robust testing of Opalinus Clay is possible. Different laboratories performed the same tests on nearly identical core material and with different testing procedures. In the case of the shaly OPA, the reproducibility of the experimental results in terms of hydro-mechanical response was clearly demonstrated. On the other hand, comparing test results in the sandy OPA is more challenging due to the more pronounced heterogeneity of the material with respect to the shaly OPA. Therefore, in the latter case, the selection of the specimens for the performance of triaxial tests plays a major role for the comparison of the hydro-mechanical response of the material and the estimation of the geomechanical parameters.

The established testing procedures to perform undrained triaxial testing of OPA can be validated, and the following further testing recommendations might be considered for future testing campaigns.

9.1 Pre-testing and saturation phases

- The initial conditions of the specimens before starting the tests have to be accurately assessed in terms of both water content and bulk density. Regarding the water content, beside the measurement on the tested specimens, it is suggested to have a second measurement on a piece of material obtained from the core as close as possible to the specimen (similar to the Lab B procedure). The bulk density can be retrieved from specimen's volume measured with calliper. When the specimens are initially equalized in desiccators at given relative humidity (Lab C and Lab E procedures), the water content and bulk density should be measured both before and after the equalization. In any case, it is mandatory to measure the specimen weight before and after testing. These aspects are of great importance to evaluate the response of the material during the initial saturation phase, in particular in terms of swelling pressure. Due to the high variability in mineralogical composition, the water content of the cores from which the specimens are then extracted does not represent fundamental information for the interpretation of the tests, but it can give a useful overview on the conditions of the material.

- The specimens' conditions after testing have to be also carefully assessed in terms of water content. To this aim, the entire tested specimens have to be removed from the rig and dried in the oven at 105 °C to obtain the dry weight. The dry weight is then used to back-calculate the water content of the specimens after preparation, before testing, and also during the eventual equalization in a desiccator.

- An isotropic stress must be applied before starting the saturation phase of the tests by putting the tested specimen in contact with the fluid. This initial isotropic stress should allow just the application of a small back pressure (~ 100 kPa) to start the saturation process of the tested specimen. 0.5 MPa of isotropic stress should be considered as maximum value for this initial step of the tests; higher values of stress may influence significantly the development of the swelling pressure during saturation.

- The initial specimens' saturation represents a key phase of the test. It is suggested to keep the specimens in contact with fluid at a low pressure until the complete stabilization of the stresses is observed. Just then the stresses and the pore water pressure can be increased to further enhance the saturation and perform the B-check test.

  Due to the anisotropy of the OPA, the swelling pressure must be evaluated in both directions perpendicular and parallel to bedding. Although this aspect does not represent an issue in S-tests, it is a disadvantage in the case of P-tests. Indeed, the testing layout of all the adopted equipment allows the isotropic control of the confining pressure. Therefore, the different swelling pressures that might be exhibited in the two orthogonal radial directions in P-tests cannot be detected. In this case, an average radial swelling pressure can only be evaluated. True triaxial test configuration should be considered for this purpose.

- Regarding the consolidation, the obtained results highlighted that testing specimens at low effective confining stress usually required an unloading process to bring the material to the target consolidation stress to start the shearing phase. This aspect was well observed in tests carried out at 4 MPa of effective confining stress adopting the conventional testing procedure.

- The assessment of the Skempton's B coefficient is important to assess the specimen's saturation. When B values are not satisfactory, it is possible to perform an undrained compaction until an increase of the back pressure is observed. This methodology is different than the more traditional procedure of re-establishing drained conditions to increase the back pressure in order to enhance the saturation before performing a new B-check measurement. The results of the alternative procedure support this alternative methodology, which might reduce significantly the time required to assess the specimen saturation.

  As leakages might be a problem during the tests, a check should be foreseen before the measurement of the Skempton's B coefficient and the shearing phase. A leakage check can be performed in undrained conditions by closing all the valves connecting the specimen to the water pumps. Pore pressure variation is then monitored with an internal pressure transducer for a period of at least 24 hours. Pressure decreased might be observed in the case of not fully saturated conditions, with a final stabilization. In the case of a pure leakage, the pressure decrease should not stabilize.

9.2 Shearing phase

- Considering the testing set-up, specimens' size, and drainage configurations (use of side drains), strain rates in the range between 2×10^{-7} s^{-1} and 5×10^{-8} s^{-1} were demonstrated to be appropriate for testing Opalinus Clay specimens for undrained boundary conditions (both shaly and sandy OPA).

- The strain dependency of the undrained elastic moduli highlighted the importance of using a consistent testing protocol for the performance of the unloading-reloading cycles. This aspect is of great importance to compare elastic moduli measured before and after the failure of the specimens. From the obtained results, it was observed that the elastic modulus decreases as the axial strain interval of the stress cycle increases. To have a proper evaluation of the elastic parameters, the specimens should experience an axial strain interval of at least 0.001 for both S and P-tests. Regarding the different elastic parameters analysed in the tests, the performance of the unloading-reloading cycles must be considered a fundamental method to evaluate the damage of the material. Indeed, most of the specimens experienced a clear failure during the tests, with the presence of an oblique failure plane. On the other hand, this aspect does not allow a correct evaluation of the radial deformations after failure when punctual measurement systems (such as LVDTs) are used, with consequences also on the assessment of the volumetric strain.

- A low initial value of the pore fluid pressure may cause problem during the shearing phase. Back fluid pressure decrease was observed when the specimens were approaching failure. This aspect was particularly evident for the tests performed on the sandy OPA, where the back pressure decreased even to 0 MPa posing issues in the interpretation of the tests in terms of effective stress. To avoid this problem, a higher initial pore fluid pressure (> 5 MPa) might be considered.

- The volumetric response of the specimens during shearing was found to play a key in controlling the mechanical response of the material. The difference evolution of the back pressure during shearing between the shaly and sandy OPA highlighted a more pronounced dilatant response for the sandy OPA. The bedding orientation played also a key role, where P-test exhibited an increase of the back pressure until the specimens' failure. The testing equipment used for the measurement of the specimens' deformations (both axial and radial) must therefore be capable to provide reliable measurement for a proper evaluation of the volumetric strain during shearing.

- Regarding the tests performed in extension, the CTE stress path must be preferred over the RTE stress path. The evolution of the pore fluid pressure is responsible for this choice, as in the case of RTE test (Lab B Test 5), the unloading of the specimen induced a decrease of the back-fluid pressure to 0 MPa. A second possibility to perform extension tests with an unloading process might be the triaxial extension (TE) stress path, where the axial stress is reduced while the radial stress is increased to keep the mean total stress constant. This stress path might induce a lower reduction of the pore water pressure during shearing.

10 References

Favero, V., Ferrari, A. & Laloui, L. (2018): Anisotropic behaviour of Opalinus Clay through consolidated and drained triaxial testing in saturated conditions. Rock Mechanics and Rock Engineering, 51(5): 1305–1319.

Giger, S.B., Ewy, R.T., Favero, V., Stankovic, R. & Keller, L.M. (2018): Consolidated-undrained triaxial testing of Opalinus Clay: results and method validation. Geomechanics for Energy and the Environment, 14, 16–28.

Head, K.H. & Epps, R.J. (2011): Manual of Soil Laboratory Testing - Volume 2: Permeability, Shear Strength and Compressibility Tests, 3rd Edition.

Renner, J., Evans, B. & Hirth, G. (2000): On the rheologically critical melt fraction. Earth Planet Sci Lett 181(4): 585–594.